University of Twente

Royal Netherlands Aerospace Centre (NLR)

Characterization of the Onset of Boiling for Ammonia in Minichannels

Master Thesis

Document number: 421

Author:
T. Luten
s1820540
Mechanical Engineering
Thermal and Fluid Engineering
University of Twente

Graduation committee:
Dr. ir. R. Hagmeijer
Dr. ir. J.B.W Kok
Dr. ir. S.G. Huisman
Ir. A.K. te Nijenhuis

December, 2022

Abstract

The temperature of an aircraft or spacecraft heat load can be controlled by a two-phase mechanically pumped loop (MPL) thermal management system, using the evaporation of a fluid. The refrigerant fluid of the thermal management system absorbs the heat of the heat load in an evaporator. After the evaporator, the vapour-liquid mixture will proceed to the condenser, where the absorbed heat is emitted into the surroundings. A two-phase MPL thermal management system is an emerging cooling technique for the aerospace industry, for instance for hydrogen fuel cells or power electronics.

The boiling process plays a critical role in the heat transfer from the heat load to fluid in a two-phase MPL. However, the onset of the boiling process in the evaporator is not yet fully understood and superheated liquid may show up at the beginning of the evaporator. In this research, it is investigated whether it is possible to reduce the superheated liquid temperature and to improve the onset of boiling by adding non-condensable gases (NCGs) to a two-phase system. It is hypothesized that the addition of dissolved gases will increase the number of nucleation sites and thus, a smaller energy threshold is present for the fluid to start boiling.

To predict the superheated liquid temperature, a theoretical model with the convection-diffusion equation is used that can deal with various setup conditions. The location of superheated liquid on the wall in the evaporator section can be determined with this. Experiments verified that superheated liquid is exhibited at relatively low heat fluxes on the evaporator in combination with a low saturation temperature. On the other hand, subcooled liquid occurs at higher heat fluxes in combination with a higher saturation temperature. The tests presented here were carried out with ammonia as a refrigerant at saturation temperatures of 40, 60 and 80 °C. The heat flux range was from 1 to 20 W/cm^2 and a laminar mass flow of 0.1 g/s is used resembling typical conditions for two-phase MPL thermal management systems for aerospace cooling purposes.

The hypothesis that dissolved gasses affect the boiling process has neither been confirmed nor disproved by the carried-out experiments. With the used setup, the distribution of the added NCGs was controlled insufficiently which resulted in non-accurate results in the test section of the setup. It is expected that the dissolved nitrogen gas enters the accumulator and stays there. Moreover, a lack of data on the solubility of nitrogen in ammonia was observed in the literature. Therefore, predictions on the amount of nitrogen to be added to the system were inaccurate.

The results of this report will advance the understanding of the onset of boiling in two-phase MPL thermal management systems. Modelling the superheated liquid temperature can be used in the design process of a two-phase MPL thermal management system. Depending on the conditions such as the heat flux, saturation temperature and the surface roughness of the channels used in the evaporator, it can be predicted whether and what the superheated liquid temperature will be. The report concludes with recommendations to conduct experimental research into the solubility of refrigerant fluids and especially near the saturation temperature. In addition, attention was given to a more ideal experimental setup for a follow-up study which is already planned for the near future.

Acknowledgement

This research was supervised by dr. ir. R. Hagmeijer. I am grateful to him for the support and the critical comments and discussions during the monthly meetings. In addition, I appreciated that you took the time to come and have a look at the experimental setup at NLR in Marknesse.

I would also like to show my gratitude to Arne te Nijenhuis and Henk Jan van Gerner as external supervisors from NLR. I enjoyed the weekly meetings, physical or via Skype. Arne, thanks for all the feedback and for reading my draft report which greatly improved the research and the final report. Henk Jan, thank you for sharing your knowledge during the many conversations we had. Furthermore, thanks to both of you for always being available for questions. Also for questions or conversations off-topic about, for example, cycling. In addition, I would like to thank Ramon van den Berg for his contribution to the last phase of the research on NCGs.

I am also very grateful to the people of the thermal control lab. In particular to Gerrit van Donk, Aswin Pauw and Bram Lamers. Unfortunately, Gerrit is no longer with us. He was the brain behind the used experimental setup and got the setup working again in the summer of 2021. In addition, he was the inventor of the purchased nitrogen injection valve. In addition, I would like to thank Bram for converting the setup and the software adjustments. You were still working on the setup one day before your wife gave birth. Of course, I can not forget Aswin. Thanks for the enjoyable moments in the lab, for making the setup leakproof with the 'cup method', and for filling the setup several times together with Bram. Without you, I would not have been able to carry out my experiments.

In addition, I would like to thank everyone for their help and understanding for the period that has arisen during the final phase (2022) of the graduation project. There are many people to name but I am very grateful to everyone! Finally, I would like to thank the whole ASEQ department for the enjoyable and educational period at the office. Furthermore, I would like to thank the entire NLR for allowing me to work on location in Marknesse during the strange times of Covid-19. Last but not least, thanks to the football players and walkers for the distraction and fun during the lunch breaks.

Contents

List of Figures

List of Tables

Nomenclature

Symbol	Description	Unit
P	Power	W
h_{lv}	Latent heat of evaporation	J/kg
c_p	Specific heat	J/kgK
T	Temperature	K
x	Vapor mass fraction	-
ρ	Density	kg/m^3
k	Thermal conductivity	W/mK
σ	Surface tension	N/m
A	Area	m^2
q	Heat flux	W/cm^2
G	Mass flux	kg/sm^2
$\dot{m}$	Mass flow	g/s
Fr	Froude number	-
u	Flow velocity	m/s
g	Gravitation acceleration	m/s^2
d	Diameter	m
Eo	Eötvös number or Bond number	-
ξ	Confinement number	-
Re	Reynolds number	-
μ	Dynamic viscosity	Pas=kg/ms
h	Heat transfer coefficient	W/cm^{2}K
Nu	Nusselt number	-
f	Friction factor	-
Pr	Prandtl number	-
ε	Surface roughness	m
ζ	Smoothing function	-
Co	Convection number	-
Bo	Boiling number	-
P	Perimeter	m
p	Pressure	Pa
X_{tt}	Lockhart-Martinelli parameter	-
x_{di}	Dry-out incipience quality	-
We	Weber number	-
Ca	Capillary number	-
r	Radius	m
H	Henry's law constant	-
X	Mole fraction	-
S	Solubility	g/kg
U	Voltage	V

Symbol	Description	Unit
I	Current	A
L	Length	m
$\dot{q}$	Uniform heat production	W/m^3
C	Constant	-
V	Volume	m^3

Abbreviations

Abbreviation	Explanation
AMS	Alpha Magnetic Spectrometer
cbd	convective boiling dominant
CFCs	Chlorofluorocarbons
CHF	Critical heat flux
CNT	Classical Nucleation Theory
GWP	Global Warming Potential
HCA	Heat controlled accumulator
HCFCs	Hydrochlorofluorocarbons
HFCs	Hydrofluorocarbons
ISS	International Space Station
MPL	Mechanically pumped loop
nbd	nucleate boiling dominant
NCG	Non-condensable gas
NFPA	National Fire Protection Association
NIST	National Institute of Standards and Technology
NLR	Royal Netherlands Aerospace Centre
ONB	Onset of nucleate boiling
PCA	Pressure controlled accumulator
PDE	Partial differential equation
REFPROP	Reference Fluid Thermodynamic and Transport Properties Database
STP	Standard temperature and pressure
SPIV	Six port injection valve
tp	two-phase

Pleasure in the job puts perfection in the work.

Aristotle

UNIVERSITY
OF TWENTE.

1

Introduction

It was in the worldwide news [1] [2], last November 2020. Glasgow, Scotland was world stage of the two-week global climate-change conference, COP26 [3]. It states and agrees to support the industry's commitments towards net-zero CO_2 emissions by 2050 [4], which is also supported by Boeing [5]. The transition from fossil fuels to renewable sources is an important part of achieving the set goals. A possible solution for long distances could be hydrogen-powered aircraft [6]. Major companies such as Airbus and Embraer have made announcements for a hydrogen-powered aircraft fleet [7] [8]. The Airbus ZEROe concepts are shown in Figure 1.1.

Figure 1.1: Airbus ZEROe concept aircraft, a turboprop, turbofan, and a blended-wing body concept [7].

Converting hydrogen into electricity can be done through a fuel cell where part of its energy is converted into heat. Typically, fuel cells have an even 1:1 power to dissipated heat ratio [9], which can generate a huge amount of excess heat for large fuel cell stacks. Furthermore, hydrogen-powered aircraft have opened up interest in the development of highly efficient power electronics [10]. These emerging applications need adequate thermal management systems.

Conventional cooling methods are ambient air cooling or liquid cooling. However, with the significant increase in electric power density of aircraft and to keep the mass and

power low of a cooling system, advanced cooling techniques are needed for the next generation of aircraft [10]. Two-phase mechanically pumped loop (MPL) cooling can be an adequate solution for the emerging need for cooling power electronics [11] [12] and fuel cells [13] [14] [15].

A two-phase MPL thermal management system is a cooling method especially suited for high heat flux applications and to ensure temperature uniformity [16] [17]. Using the evaporation of a refrigerant fluid, it absorbs the heat of the heat load in a cooling plate. The fluid emits heat into the air with an air heat exchanger. A schematic overview is shown in Figure 1.2, where P is the power in watts. The concept of a two-phase MPL thermal management system will serve as a framework for this study.

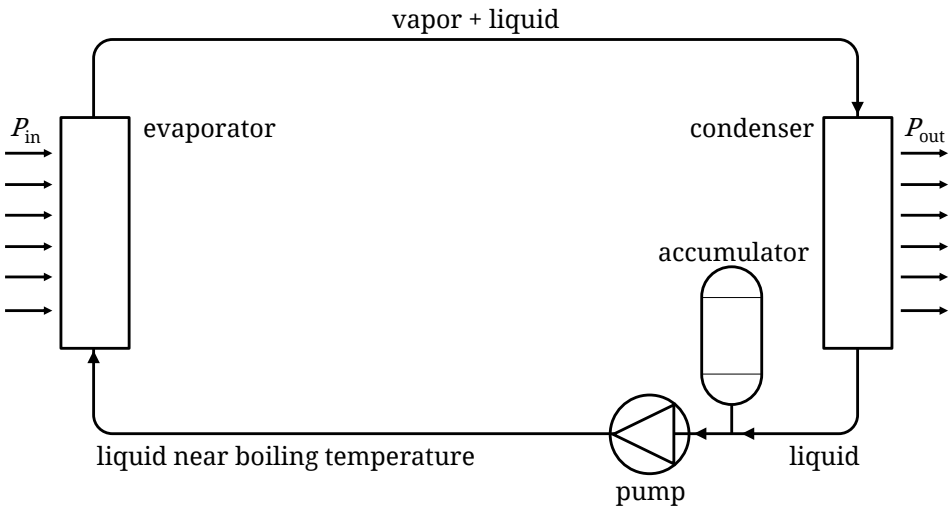

Figure 1.2: Schematic of a two-phase MPL thermal management system.

Nevertheless, several critical elements of a two-phase MPL thermal management system have not been addressed in recent years, which has resulted in sub-optimal system performance. One topic that is not yet fully understood is the onset of boiling in the evaporator section. Previous experiments with two-phase MPL demonstrator systems in the thermal control test lab at the Royal Netherlands Aerospace Centre (NLR) have shown that both subcooled liquid and superheated liquid can enter the evaporator, depending on the specified operating conditions.

Theoretically, fluid will start to boil at saturation temperature and saturation pressure. In practice, when superheated liquid enters the evaporator, the liquid temperature of the refrigerant is above the theoretical saturation temperature, which can cause too high heat load temperatures. For instance, in a fuel cell, too high temperatures are undesirable [18]. Subcooled liquid occurs when fluid enters the evaporator below the saturation temperature while there is already two-phase behavior on the wall [19], which is a desirable effect in two-phase MPL thermal management systems.

The main goal of this research is to investigate if it is possible to reduce superheated liquid temperature or ultimately, prevent superheated liquid completely in an experimental setup. Several mechanisms such as rough walls [20], the addition of nanofluids [21], and the addition of dissolved gases [22] [23] [24] can be introduced to a two-phase MPL system to increase the number of bubble nucleation sites, and thus improve the onset of boiling.

In this research, it is investigated whether it is possible to reduce the superheated liquid temperature and to improve the onset of boiling by adding non-condensable gases to a two-phase system. It is hypothesized that the addition of dissolved gases will increase the number of nucleation sites and thus, a lower liquid temperature is required to start boiling. No or reduced superheated liquid will result in better temperature uniformity of the heat load and higher reliability and predictability of the two-phase MPL thermal management system.

1.1 Problem definition

The main research question becomes:

- *Do dissolved gases in refrigerants have a reducing effect on the superheated liquid temperature?*

Defined subquestions during this research are:

- *What is the solubility of non-condensable gases in refrigerants?*
- *Can the subcooled and superheated liquid temperature be quantified for a pure refrigerant flow through a circular channel at a heated wall?*
- *What is the influence of the heat flux and saturation temperature on the superheated liquid temperature?*

In parallel with the research question, the following subquestion is also being investigated:

- *Can dissolved gases in refrigerants improve the boiling heat transfer?*

1.2 Report outline

To answer these research questions, the theory behind it is described in Chapter 2. Within this chapter, the two-phase MPL thermal management system is explained in detail. In addition, typical two-phase refrigerants are treated and the focus is placed on the evaporator section. Next, the boiling process will be described including flow boiling heat transfer and flow characterization. In addition, subcooled and superheated liquid is discussed. Finally, this section describes the solubility of dissolved gases in refrigerants.

Chapter 3 describes the experimental setup used. Besides, it describes how the heat transfer coefficient is approached and the verification of the experimental setup. Chapter 4 deals with modelling. The boiling heat transfer coefficient is discussed and the model using the convection-diffusion equation is described for the prediction of subcooled and superheated liquid.

Next, Chapter 5 presents the experimental results about subcooled liquid, superheated liquid, and the addition of dissolved gases. In addition, the results are compared with empirical correlations and with the created model. The report ends with a discussion, conclusion and recommendations.

2

Theory

This chapter discusses the theory behind a two-phase MPL thermal management system, the boiling process, the heat transfer coefficient, and subcooled and superheated liquid. Finally, the solubility of non-condensable gases in refrigerants is discussed.

2.1 Two-phase MPL thermal management systems

A two-phase MPL thermal management system was already shortly described in the introduction and a schematic was shown in Figure 1.2. This section describes the system in more detail.

Two-phase MPL is one of the specialities of the Thermal Management department of NLR. One example of an applied two-phase MPL thermal management system is in the Alpha Magnetic Spectrometer, also known as AMS-02, which was launched with a space shuttle in May 2011 and subsequently mounted on the International Space Station (ISS) [25].

2.1.1 Working principle

First, a pump is used to circulate a working fluid, the coolant. The pump is usually seen as the 'start' of the loop as the pressure here is highest and is always placed on the liquid side of the loop. The coolant flows to an evaporator where the liquid is evaporated. The heat is absorbed and the liquid-vapor mixture flows to a condenser where it is condensed back into the liquid.

The saturation pressure (and thereby the saturation temperature) in the system is controlled by the accumulator and it functions as a coolant tank. Two types of accumulators are possible, a heat controlled accumulator (HCA) or a pressure controlled accumulator (PCA). It is also possible to have a two-phase MPL thermal management system without an accumulator. In that case, the pressure in the system can be controlled by the pump speed.

A recuperator can be used to heat the liquid near the saturation temperature. Moreover, the vapor then cools down, which is beneficial for the condensation process. If the liquid is not near saturation temperature after the recuperator, a preheater can be placed before the evaporator. A schematic with recuperator and preheater is shown in Figure 2.1.

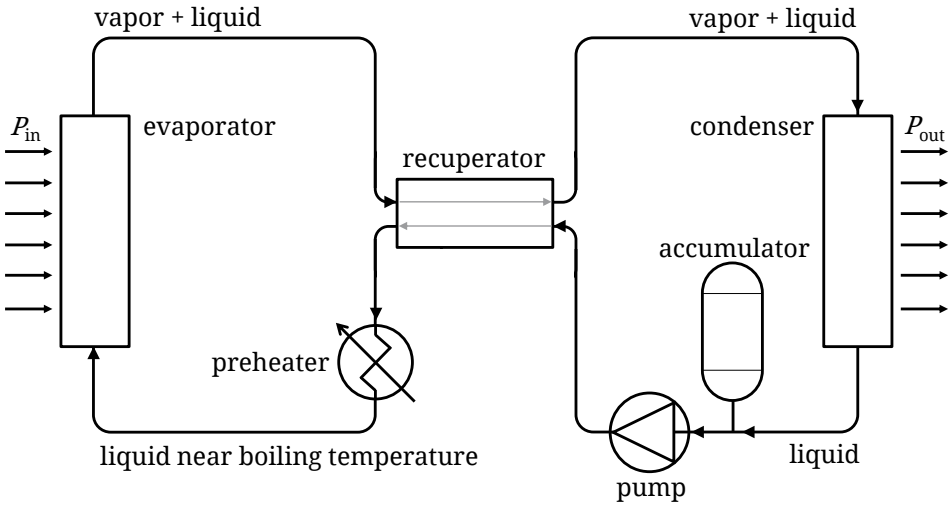

Figure 2.1: Schematic of a two-phase MPL thermal management system with recuperator and preheater.

An advantage of a two-phase MPL thermal management system is the uniform temperature due to the boiling process in the evaporator. Because of the latent heat of vaporization (h_{lv}) of the fluid, the fluid's temperature does not increase when heat is added. Instead, the vapor mass fraction of the fluid increases. The vapor mass fraction is also known as the quality of the mixture and is denoted by x. It is zero for liquid and one for vapor. Typically, NLR works with a maximum vapor mass fraction of 0.7 at the outlet of the evaporator. The latent heat of vaporization and the increasing vapor mass fraction allows the cooling plate to operate at a very stable uniform temperature. This is in contrast to a single-phase cooling system, where the temperature of the coolant increases over the length of the cooling plate.

Moreover, the required mass flow for a two-phase MPL thermal management system is much smaller than for a single-phase MPL cooling system. This is because the latent heat of vaporization of a fluid is typically much larger than the specific heat capacity of a fluid times the allowed temperature gradient, i.e. $c_p \Delta T$. To compare the heat transport equations, $h_{lv}x$ is proportional to $c_p \Delta T$. The smaller mass flow results in a smaller tubing diameter, lower pump power and finally an overall lower mass for the cooling system in comparison with single-phase cooling.

Another advantage is that the heat transfer coefficient in the evaporator from wall to fluid is much higher for two-phase flow than for liquid flow. Therefore, a smaller temperature difference is present at the interface of fluid and heat load. Ultimately this means that the fluid can operate at higher temperatures, near the heat load temperature. This results in a smaller surface area for the condenser.

The disadvantage in comparison with single-phase cooling is the required larger accumulator, to account for the volume expansion that comes with the phase transition of the fluid from liquid to vapor. A single-phase MPL system only has to deal with the liquid volume expansion. Furthermore, leak tightness is critical, to ensure operation around the saturation characteristic of the fluid. Also, the design is more complex for a two-phase MPL system.

2.1.2 Typical two-phase refrigerants

The working fluid is responsible for absorbing the heat generated by the heat load and transporting it to the condenser. The fluid selection is one of the most important steps for the design of a two-phase MPL thermal management system. Fluids can be selected from the NLR's System Analysis Tool [26] based on the specified requirements. This tool is made in MATLAB and uses the Reference Fluid Thermodynamic and Transport Properties Database (REFPROP) from the National Institute of Standards and Technology (NIST), which contains more than 150 different fluids. For this research, only typical two-phase refrigerants are treated, these are shown in Table 2.1. Depending on the application there is an operating temperature, in this example, the fluid properties are considered at 60 °C. Experience within NLR is that many projects have a typical operating temperature between 30 and 100 °C. In the remainder of the report, fluid properties will often be considered at 40, 60, and 80 °C.

Table 2.1: Typical two-phase refrigerants with their fluid properties considered at a temperature of 60 °C.

	R134a	R1234yf	R245fa	R1233zd(E)	Ammonia	Methanol
Pressure at 20 °C [bar]	5.7	5.9	1.2	1.1	8.6	0.1
Pressure at 60 °C [bar]	16.8	16.4	4.6	3.9	26.1	0.8
Liquid density [kg/m^3]	1053	941	1237	1173	545	753
Density ratio [-]	12	9	49	57	27	731
Specific heat [kJ/kgK]	1.7	1.7	1.4	1.3	5.2	2.8
Thermal conductivity [W/mK]	0.07	0.05	0.08	0.07	0.39	0.19
Latent heat of vaporization [kJ/kg]	139	110	169	171	998	1110
Surface tension [N/m]	0.004	0.002	0.009	0.010	0.013	0.019
$\partial p_{\text{sat}}/\partial T_{\text{sat}}$ [bar/°C]	0.40	0.37	0.13	0.11	0.64	0.03
Maximum NFPA	1	2	2	2	3	3
GWP	1530	0.5	962	3.9	0	1.0
Future availability	Phased out	Probably good	Phased out	Good	Good	Good

In this table, the safety of fluids is rated with the National Fire Protection Association (NFPA) 704 standard [27] in the form of a "safety diamond". The diamond differs per fluid and a description of the different values ranging from 0 to 4 for health, flammability, and instability is shown in Figure 2.2. Here 0 means minimal hazard and 4 means severe hazard. For instance, ammonia and methanol have a value of 3 for toxicity and flammability, respectively. With the NLR's System Analysis Tool, fluids with a high NFPA value can be excluded.

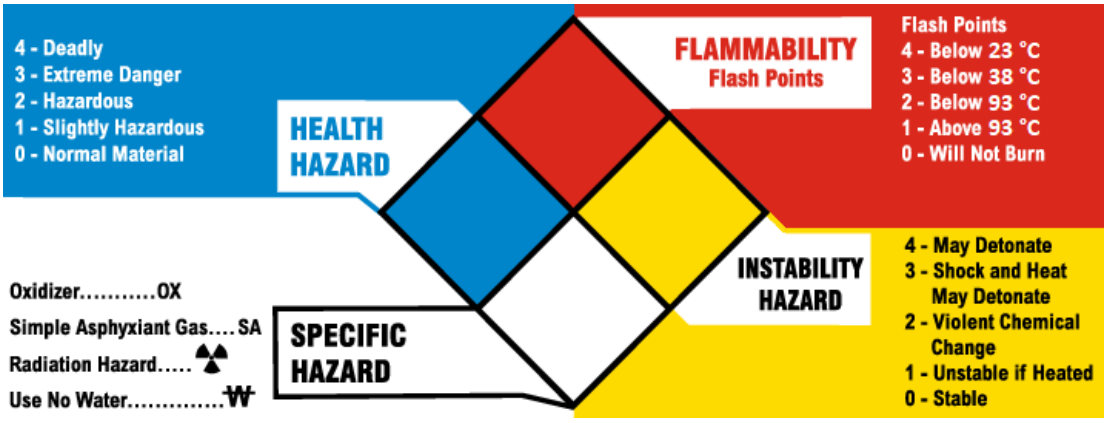

Figure 2.2: NFPA diamond with the hazards and risks for health, flammability, and instability [28].

Furthermore, some fluids deplete the ozone layer. This is laid down in the Montreal Protocol [29], which banned chlorofluorocarbons (CFCs) and hydrochlorofluorocarbons (HCFCs). R134a and R245fa are hydrofluorocarbons (HFCs) that were developed to replace CFCs and HCFCs. However, these fluids have a high Global Warming Potential (GWP) and will eventually be banned [30]. Currently, R134a will no longer be approved for use in new light-duty vehicles manufactured or sold in the United States as of the model year 2021 [31]. For example, R1234yf and R1233zd(E) are the successors of R134a and R245fa, respectively. As seen in Table 2.1 these fluids have a lower GWP.

Important for a two-phase MPL thermal management system is to have a suitable fluid that can absorb as much energy as possible. According to the table, ammonia would then be an extremely suitable refrigerant. Ammonia often results from NLR's System Analysis Tool in various projects. However, ammonia is for high-pressure applications and is toxic, so it may not be within the requirements of the thermal management system. Therefore, other typical two-phase refrigerants can be selected from the table depending on the requirements.

2.1.3 Evaporator section

With a chosen refrigerant and typical diameter from the NLR's System Analysis Tool, the focus can be shifted to the evaporator section. A typical evaporator for a two-phase MPL thermal management system is shown in Figure 2.3. This example was made by NLR itself using 3D metal printing. The functioning of a two-phase MPL system is demonstrated, therefore the evaporator has not been further optimized. It makes use of relatively simple parallel circular channels as shown in Figure 2.4. In most projects, only the diameter is a design parameter where the cross-section shape and the orientation of the channels in the evaporator plate are usually fixed.

Typically the diameters of channels in the evaporator plate are in the range of minichannels. Minichannels are channels with a diameter between 0.2 and 3 mm [20], which is within the range of 3D metal printing manufacturability at NLR. In these minichannels, the flow behaves as in conventional channels that have larger diameters. The flow characterization of these parameters will be discussed in Section 2.2.4.

The focus of this research is on the evaporator of a two-phase MPL cooling system, and in particular the first section of the evaporator where the fluid has to start boiling. Important here is the conditioning of how the fluid enters the evaporator, such as the

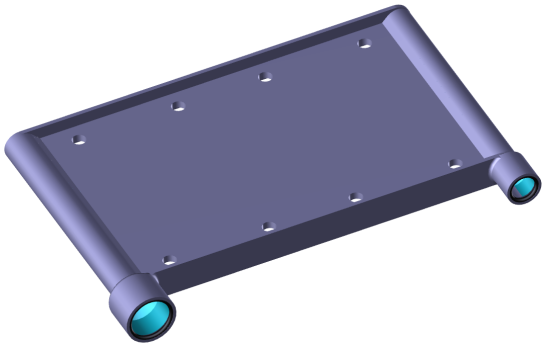

Figure 2.3: Typical evaporator design.

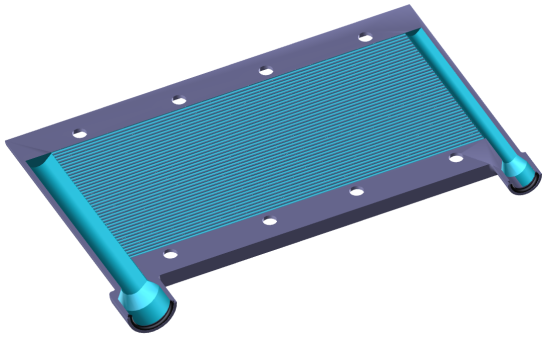

Figure 2.4: Cross-section evaporator.

inlet temperature. To further elaborate on this, the next section will continue on the theory behind boiling.

2.2 Boiling process

The boiling of a fluid is a two-phase heat and mass transfer process. It is a phase transition from a liquid to a vapor that occurs at the corresponding boiling point. From an engineering point of view, boiling can be categorized into pool boiling and flow boiling (also known as forced convection boiling) [32].

In pool boiling, a pool of liquid is converted into vapor by continuously heating a wall through an external source. The bulk liquid is stagnant and nucleation sites are required for the liquid to start boiling. It is generally considered that these nucleation sites are cavities or scratches in the solid surface of the wall [33]. A well-known example is when water is boiled in a pan. Vapor bubbles nucleate at the heated surface and rise through buoyancy forces. A schematic representation of pool boiling is shown in Figure 2.5.

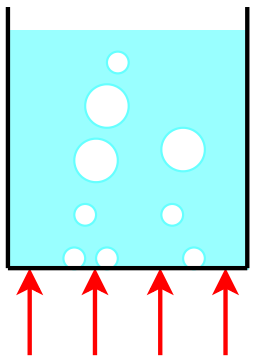

Figure 2.5: Pool boiling.

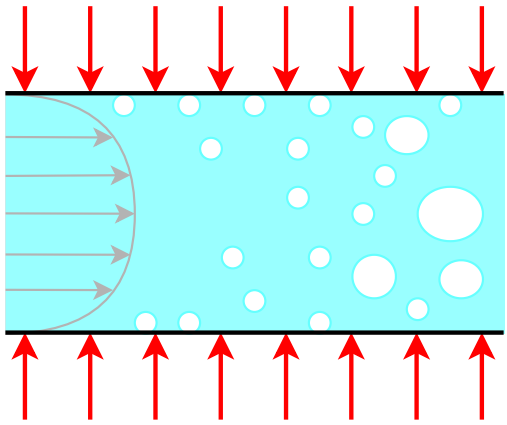

Figure 2.6: Flow boiling.

2.2.1 Flow boiling heat transfer

The different aspect of flow boiling is that a liquid flow along a heater surface is driven by external means. Flow boiling can be divided into external and internal flow boiling. Respectively, a forced flow over a heated surface or inside a heated tube. In this study, only flow boiling through tubes is treated. Internal flow boiling is also known

as two-phase flow. To distinguish both boiling phenomena, a schematic representation of flow boiling is shown in Figure 2.6. The red arrows indicate an arbitrary heat input and the gray arrows an arbitrary velocity field. The amount of heat that is dissipated from the heating surface per unit area is defined as the heat flux and is measured in W/cm^2. For cooling applications, it is a widely used unit since small surface areas are involved.

Internal flow boiling is much more complicated to understand because there is no free surface for the vapor to escape, and thus both the liquid and the vapor are forced to flow together. Depending on the relative amounts of liquid and vapor, the two-phase flow can have different flow regimes. A schematic representation of the different flow regimes with an indication of the corresponding heat transfer coefficient is shown in Figure 2.7.

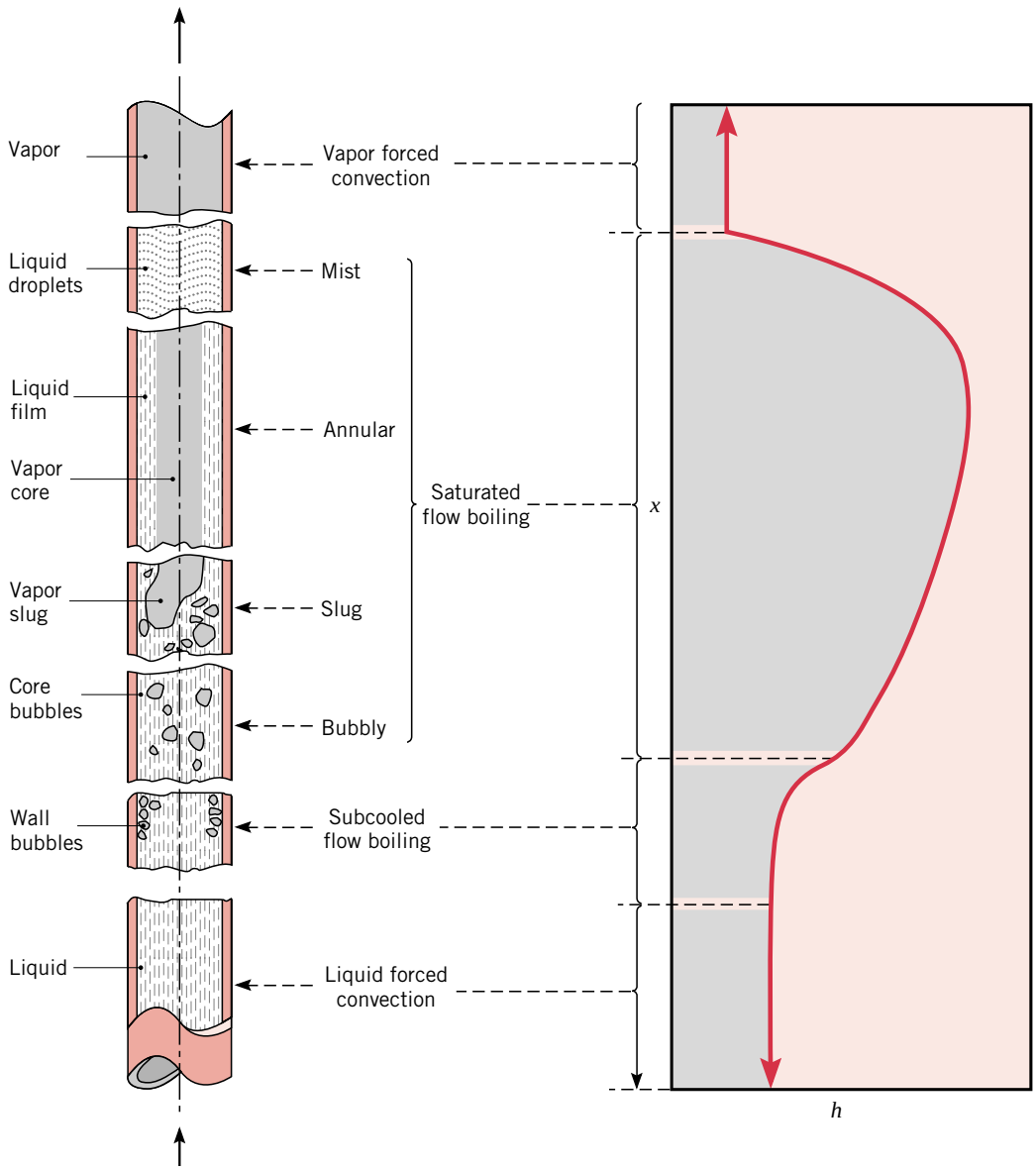

Figure 2.7: Flow regimes for flow boiling in a tube and heat transfer coefficient indication [32].

2.2.2 Flow regimes

Between liquid forced convection and vapor forced convection there occurs flow boiling. At the bottom of the figure, the flow is completely liquid and at the top completely vapor. In between, the vapor mass fraction is denoted by x, as mentioned earlier. The plot on the right indicates the corresponding heat transfer coefficient. This will be discussed in detail in the next section. For now, the focus is on the left part of the figure.

Saturated flow boiling can be divided into different flow regimes, namely bubbly, slug, annular, and mist flow. Before the liquid shows two-phase behavior, there is subcooled flow boiling. Here, the temperature of the bulk liquid is below the saturation temperature and bubbles that form at the tube surface can grow or collapse. When the bulk temperature reaches the saturation temperature and the flow regime dictates that bubbles can exist at any radial location, saturated flow boiling occurs. The bubbly flow regime occurs first. These corresponding temperatures are shown in Figure 2.8.

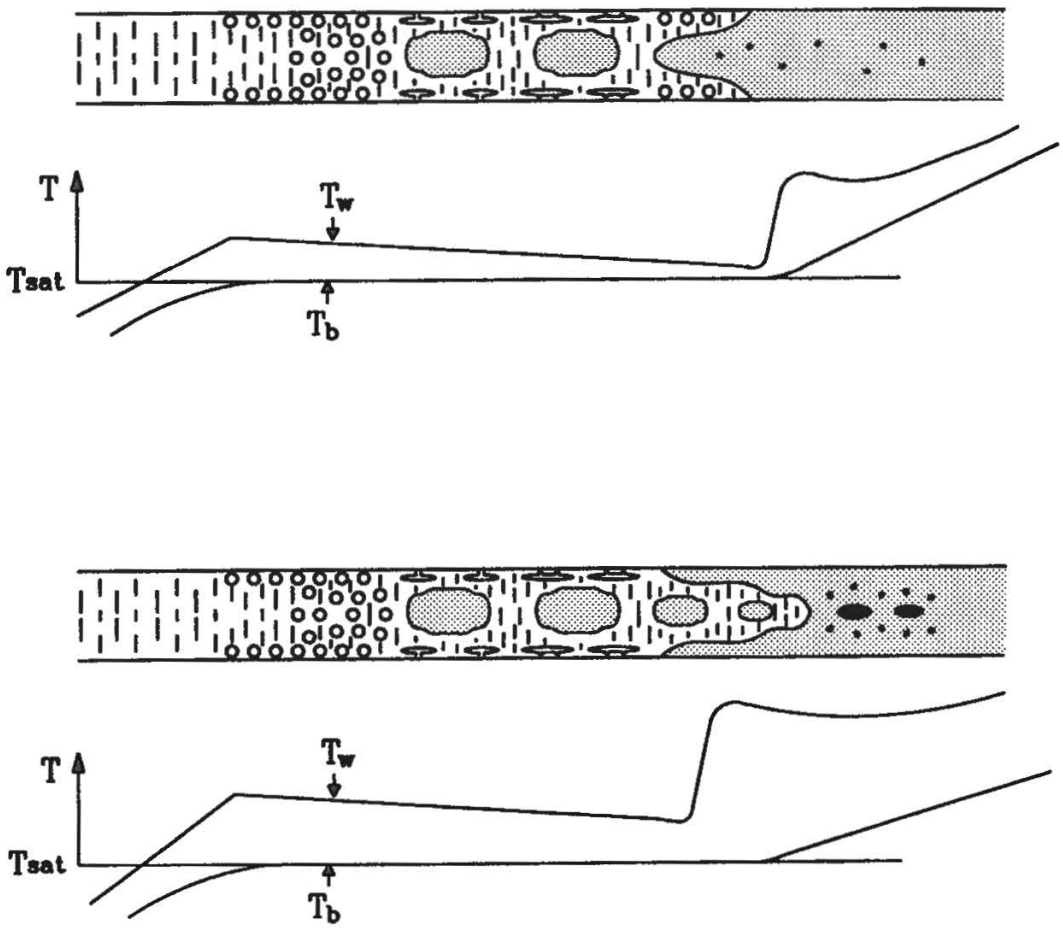

Figure 2.8: Schematic representation of different flow regimes for flow boiling in a tube and indication for the wall temperature (T_{w}) and the bulk temperature (T_{b}). T_{sat} corresponds to the saturation temperature. The top picture applies to low heat fluxes or low flow rates and the bottom picture applies to high heat fluxes or high flow rates [33].

The wall temperature is higher than the saturation temperature due to the applied heat flux. The bottom picture has a relatively higher wall temperature because of the

higher applied heat flux. As the vapor mass fraction increases, bubbles coalesce to form vapor slugs. The next flow regime is annular flow, which has a vapor core and a liquid film. Annular flow is the preferred flow regime for two-phase MPL thermal management systems because of the relatively high heat transfer coefficient as shown in Figure 2.7 and the 'smooth' flow pattern. However, to get into the annular flow regime, the previous flow regimes must be passed. This complex process can lead to problems in practice, which will be discussed later.

Increasing the vapor mass fraction further, the wall can no longer be completely filled with liquid and dry spots eventually appear on the inner wall of the tube. This phenomenon is also called dry-out or the critical heat flux (CHF) and after this, the mist regime will occur. Dry-out can be seen in Figure 2.7 and 2.8 when the heat transfer coefficient decreases and the wall temperature increases, respectively. Moreover, it is visible that at relatively high heat fluxes the wall temperature rises earlier. This is in agreement with previous experiments of two-phase MPL thermal management systems within NLR's test facility. According to Figure 2.8, it is preferred to use a maximal vapor mass fraction of 0.7 to maintain a liquid-vapor mixture at the outlet of the evaporator. In practice, this is a wide margin so that dry-out does not occur and the heat load can operate at a relatively uniform temperature.

A remark about these flow regimes is that in the literature there are also variants in between. Like plug, bubbly slug, churn, and wispy annular. Moreover, the flow regimes depend on the diameter of the tube, the fluid, the mass flux, the heat flux, the vapor mass fraction, and the temperature. This will be discussed in the following sections.

2.2.3 Nucleation

Back to the beginning of the boiling process, nucleation is the first step. Because different terms of nucleation will come back in this report, it is briefly discussed here. Furthermore, this study did not delve deeply into the microscopic properties of fluids within the boiling process. In a lot of studies about nucleation which include microscopic properties, the Classical Nucleation Theory (CNT) and extensions thereof are used [34].

More interesting for this research is the distinction between homogeneous and heterogeneous nucleation. Homogeneous nucleation takes place away from the surface. Heterogeneous nucleation takes place at nucleation sites on the wall. Mostly at cavities or scratches in the solid surface of the wall [33]. In minichannels, heterogeneous nucleation is much more common than homogeneous nucleation [35]. This is illustrated in Figure 2.6, 2.7 and 2.8. The moment that bubbles can exist on the heated wall is also defined as the onset of nucleate boiling (ONB) [19]. In Figure 2.9, this is already before the theoretically liquid point $x = 0$.

When bubbles arise, the heat transfer mode goes from liquid forced convection to a combination of nucleate boiling and convective boiling [35]. In many cases, nucleate boiling heat transfer occurs first and the convective boiling heat transfer takes over as the vapor mass fraction increases. A relative indication for the different heat transfer modes with corresponding heat transfer coefficients is shown in Figure 2.9. For nucleate boiling, the heat directly evaporates at the wall of the tube. This results in a relatively high heat transfer coefficient for a low vapor mass fraction. For increasing vapor mass fraction, a smaller fraction of the tube wall is covered with liquid, decreasing the heat transfer coefficient.

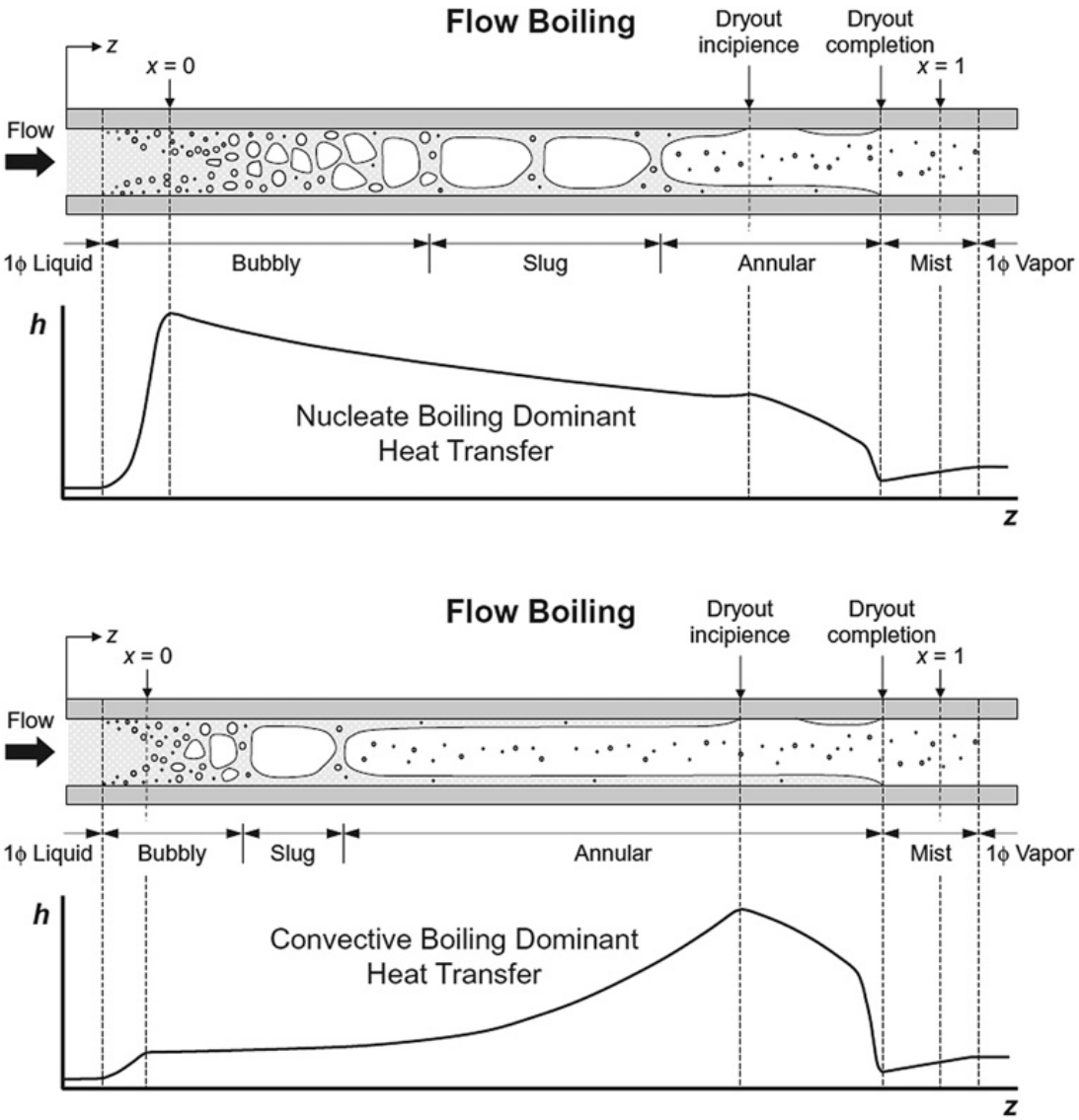

Figure 2.9: Flow regimes for flow boiling in a tube and heat transfer mode indication [35].

Convective boiling is the preferred boiling mode in a two-phase thermal management system. This heat transfer mode requires a temperature drop over the thin liquid film. Due to the heat flux on the wall, the liquid temperature is higher than the local boiling temperature. Therefore, evaporation takes place at the bulk liquid-vapor interface. As the vapor mass fraction increases, the liquid film thickness decreases and the heat transfer coefficient increases.

In practice, flow boiling consists of a combination of nucleate and convective boiling. In literature, there is no consensus about when which heat transfer mode is dominant [33] [35] [36]. Nucleate boiling can be linked to the first occurring flow regimes, like bubbly and slug flow. Annular flow is associated with convective boiling and annular flow suppresses nucleate boiling [36]. Furthermore, the flow boiling heat transfer is strongly dependent on the heat flux when nucleate boiling dominates, while the heat transfer is less dependent on the heat flux and strongly dependent on the mass flux and vapor mass fraction whereas convective boiling dominates [35]. Mass flux is the rate of mass flow, expressed in G with the unit kg/sm^2. The mass flow rate is the mass of a liquid that passes per unit of time, $\dot{m}$ in kg/s. In two-phase MPL thermal management

systems, the mass flow rate is usually expressed in g/s because of the relatively small flows.

2.2.4 Flow characterization

It is assumed that minichannels are defined with a diameter between 0.2 and 3 mm according to Kandlikar [20]. This threshold diameter is assumed during this study. Besides the influence of the heat flux and mass flux, the boiling process also depends on the diameter of the tube, the fluid, and the temperature. Much research has been done in literature on two-phase fluid that is going vertical, for example, the flow regimes in previous sections are also based on vertical flows. However, in two-phase MPL thermal management systems, the evaporator is usually oriented horizontally. In addition, when an application has to operate in space, gravity does not play a role. This combines the different parameters to flow characterization, which can be rewritten to different dimensionless numbers for a flow pattern prediction. First, the Froude number, which is the ratio between inertia forces and gravity forces.

$$\mathrm{Fr} = \frac{u}{\sqrt{gd}} \tag{2.1}$$

Where u is the two-phase velocity, g is the gravitational acceleration and d is the inner diameter of the tube. When either the mass flow is high, or the diameter is low, the Froude number will be high. Inertia forces become dominant over gravity and annular flow will form. Next, the Eötvös number or Bond number, which is the ratio between the buoyancy force to surface tension forces.

$$\mathrm{Eo} = \frac{(\rho_l - \rho_v)gd^2}{\sigma} \tag{2.2}$$

Where ρ_l and ρ_v are the liquid and vapor density respectively. When the Froude number is very large, inertia dominates over acceleration. When the Eötvös number is very small, gravity forces are negligible small with respect to capillary forces and it can be expected that the flow regime will be independent of gravitational acceleration [37]. These simple dimensionless numbers give a rough idea of the flow regimes in a tube. If gravity forces are insignificant compared to surface tension forces, the flow regimes for flows in vertical tubes will also be valid for flows in horizontal tubes. As a result, the liquid will not only be at the bottom due to gravitation but the entire tube wall could be covered with liquid.

Another dimensionless number is the Confinement number, which uses the bubble growth confinement within a channel as the parameter to distinguish the macro-to-microscale transition. The Confinement number ξ is given in Equation 2.3, not to be confused with the Convection number which will be discussed later.

$$\xi = \frac{1}{d}\sqrt{\frac{\sigma}{g(\rho_l - \rho_v)}} \tag{2.3}$$

According to Kandlikar [20], the threshold for the Confinement number is 0.5, where $\xi > 0.5$ is for minichannels. The relation between the Confinement number and the Eötvös number is $\xi = \mathrm{Eo}^{-1/2}$. This results in a corresponding threshold for $\mathrm{Eo} < 4$. According to Thome [38], there is still a significant difference of opinion with respect to the threshold of minichannel flow behavior and the different thresholds. The Reynolds

number indicates if the flow behavior is laminar, in transition or turbulent. It represents the ratio of the inertia forces to viscous forces, shown in Equation 2.4. Here, μ is the dynamic viscosity in kg/ms. For internal flow in circular tubes, it is laminar when Re $<$ 2300, fully turbulent for Re $>$ 4000 and transitional in between [39].

$$\mathrm{Re} = \frac{\rho u d}{\mu} = \frac{4\dot{m}}{\pi d \mu} \tag{2.4}$$

For steady, incompressible flow with a uniform cross-sectional area in a tube, the mass flow and velocity are constants independent of the length of the tube. The Reynolds number reduces to the right side of the equation. These simple dimensionless numbers give a rough indication about the flow regimes in a channel. In a next chapter, the experimental setup will be discussed and the above dimensionless number will be applied.

2.2.5 Flow pattern map

More detailed estimations about the transition of flow regimes can be obtained from flow pattern maps which have been developed based on empirical data. In the literature there are many different flow pattern maps with a limited range of applicability [38]. This study focuses on the most commonly used flow pattern maps. The most-widely used flow pattern map was created in 1969 by Hewitt and Roberts and is illustrated in Figure 2.10. It is a general flow pattern map for vertical flow in circular tubes for a wide range of fluids, tube diameters, mass flux, heat flux, vapor mass fraction, and temperature. Although this flow pattern map has been derived for vertical flow, it is usable for horizontal flow as well when the flow is independent of gravitational accelerations.

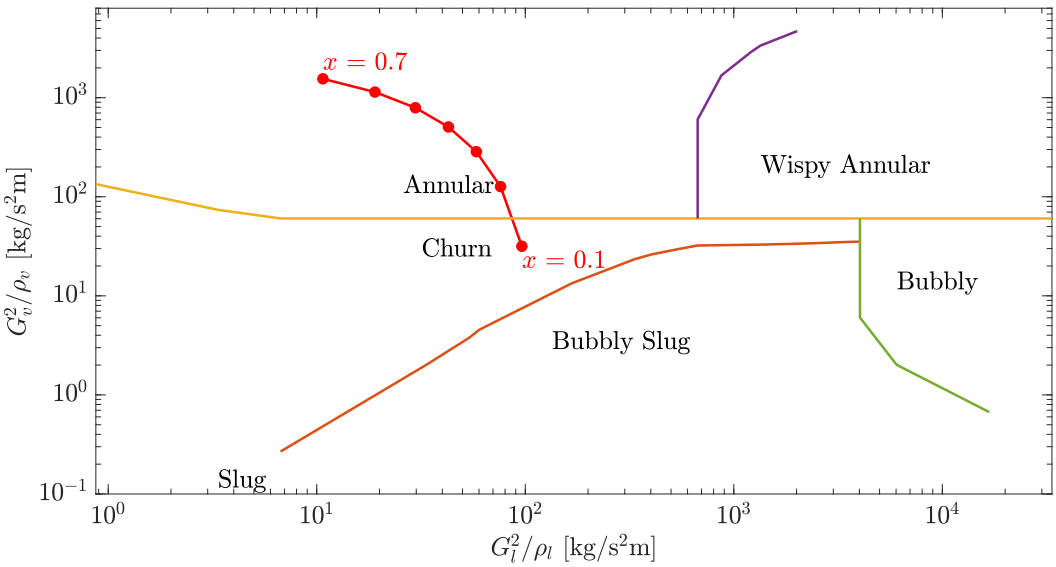

Figure 2.10: Flow pattern map for vertical flow boiling in a circular tube by Hewitt and Roberts [40]. This specific example is for ammonia as refrigerant in a 1 mm tube with a mass flow of 0.2 g/s and a saturation temperature of 60 °C.

The axes represent the superficial momentum fluxes of the respective phases, which is the mass flux divided by the density [35]. In this figure, churn flow is between the slug and annular flow regime. Wispy annular flow is between annular and mist flow. The red line in this figure indicates a continuous trend for vapor mass fractions ranging from x

= 0.1 to 0.7. For the same case, this results in a Froude number of 16.8 for $x = 0.1$ and 89.3 for $x = 0.7$. The Eötvös number is 0.4, which is far below the threshold mentioned earlier. As can be seen in the figure, the flow regime is in the less favorable churn flow for low vapor mass fraction. However, for high vapor mass fraction annular flow is expected.

In two-phase MPL thermal management systems, the evaporator is usually oriented horizontally. In conventional channels, the liquid flows over the bottom and the flow regimes are named differently. For clarity, these flow regimes are shown in Figure 2.11.

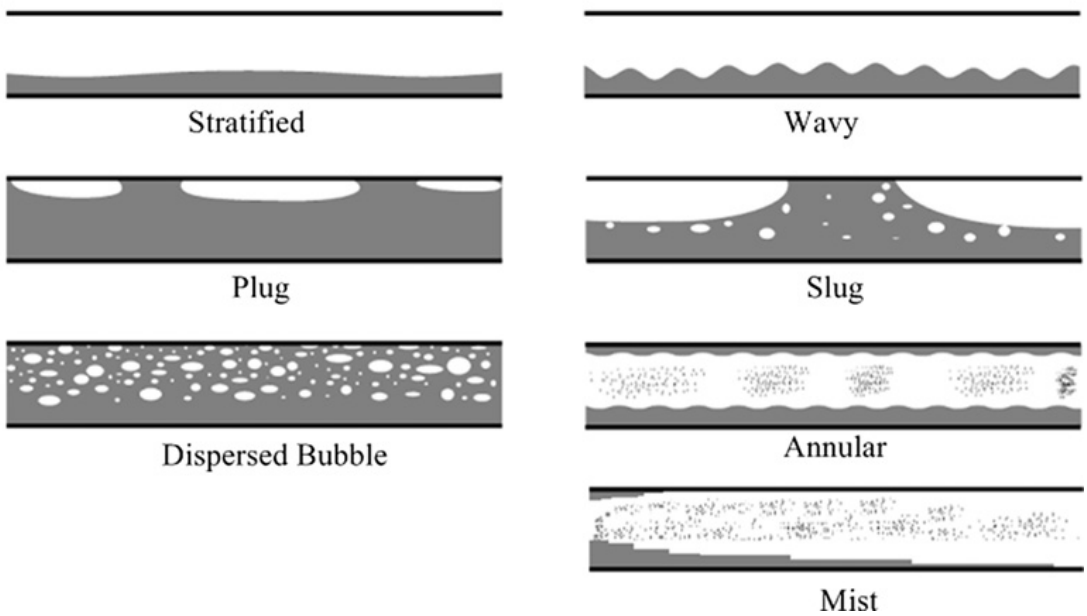

Figure 2.11: Flow regimes for horizontal flow boiling [35].

The origin of flow pattern maps for horizontal flows was laid by Baker in 1954 [41]. This map was for conventional channels with a diameter greater than 3 mm. Many different adjustments and additions have been made in the years since. In 2005, Wojtan made some important modifications to the flow pattern maps of Kattan, Thome and Favrat which include annular to dry-out and dry-out to mist flow regimes [42]. The Wojtan flow pattern map is illustrated in Figure 2.12.

The same operating points are evaluated in the Wojtan flow pattern map as the flow pattern map from Hewitt and Roberts. According to this flow pattern map, dry-out will occur in the evaporator above a vapor mass fraction of around 0.52, which results in a very low heat transfer coefficient and very poor performance of the evaporator. However, experimental experience shows that the prediction of where dry-out occurs is known to be very unreliable. In this case, a mass flux G of 255 kg/sm^2 corresponds to a mass flow of 0.2 g/s. These values will be covered in detail in the section about the experimental setup. Finally, with these prediction methods, an estimate can be made of the boiling behavior in the evaporator of a two-phase MPL thermal management system.

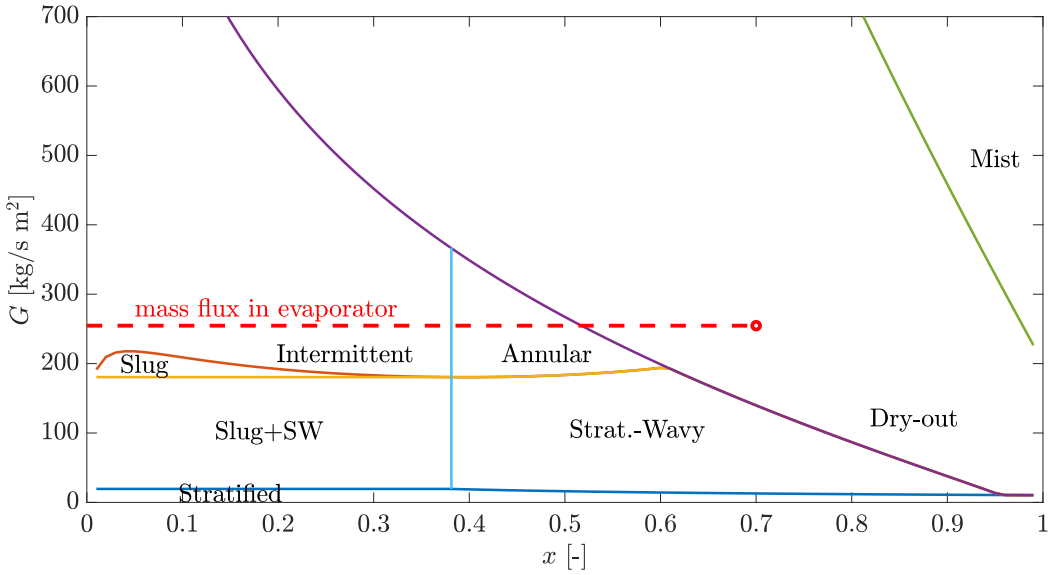

Figure 2.12: Flow pattern map for ammonia at 60 °C for horizontal tubes with 1 mm internal diameter and a mass flow of 0.2 g/s [42].

2.3 Heat transfer coefficient

The heat transfer coefficient is a measure between the heat flux and the temperature difference. The general definition of the heat transfer coefficient is given below.

$$h = \frac{q}{\Delta T} \quad \longrightarrow \quad h_{\text{fluid-wall}} = \frac{q}{(T_{\text{wall}} - T_{\text{fluid}})} \tag{2.5}$$

Where h is the heat transfer coefficient in W/cm^{2}K. Case specific, it is the rate of heat transfer between a surface and a fluid per unit surface area per unit time difference. The heat transfer coefficient is an important parameter to determine the heat transfer in a two-phase MPL thermal management system from fluid to the heat load. This research is limited to the evaporator and the heat transfer coefficient between the fluid and the wall. The heat transfer coefficient depends on a variety of properties, including the working fluid, tube diameter, heat flux, mass flux, and vapor mass fraction. An indication for the heat transfer coefficient and the wall temperatures in an evaporator was already shown in Figure 2.7 and 2.8.

According to Figure 2.7, let's first discuss the single-phase heat transfer coefficient. Before the liquid enters the evaporator, it shows single-phase heat transfer behavior. This can be calculated relatively easily with Equation 2.6. h_l is the heat transfer coefficient for liquid flow.

$$h_l = \text{Nu}\frac{k}{d} \tag{2.6}$$

Where Nu is the Nusselt number, which is the ratio of convective to conductive heat transfer. For fully developed laminar flow in a tube with circular cross-section, the Nusselt number is 4.36 [32]. It is assumed that there is a constant heat flux on the wall from the heat load. Turbulent flow cannot be determined analytically and empirical correlations must be used. Well-known correlations for turbulent flow in tubes are the

Dittus-Boelter equation and the Petukhov equation [43]. However, the accuracy of this relation at lower Reynolds numbers was improved by Gnielinksi. The Gnielinski equation from 1976 is shown in Equation 2.8 [44]. The equations to calculate the Nusselt number for single-phase fully developed flow in circular tubes are:

$$\mathrm{Nu} = 4.36 \qquad \mathrm{Re} < 2300 \tag{2.7}$$

$$\mathrm{Nu} = \frac{(f/8)\,(\mathrm{Re} - 1000)\,\mathrm{Pr}}{1 + 12.7(f/8)^{1/2}\left(\mathrm{Pr}^{2/3} - 1\right)} \qquad \mathrm{Re} > 3000, 0.5 \leq \mathrm{Pr} \leq 2000 \tag{2.8}$$

Where f is the friction factor and Pr is the Prandtl number. The method for calculating this and the Nusselt number for the transition region is described in detail in Appendix A.1.

2.3.1 Boiling heat transfer

More important in this research is the two-phase heat transfer behavior in the evaporator. Flow boiling is a very complex process and no universal prediction methods are available for minichannel flow boiling heat transfer so far [35] [45]. Many empirical correlations, based on experimental results, have been suggested by many investigators for different orientations and different fluids. However, none of these empirical correlations gives satisfactory results for all the fluids. Nevertheless, it is important for the design and during simulations of a two-phase MPL thermal management system to be able to estimate the heat transfer between the wall and the fluid.

Several prediction methods for the heat transfer coefficient in circular channels have been extensively investigated. These methods can be divided into three categories [46]:

- Strictly empirical correlations;
- Superposition correlations;
- Flow pattern based models.

Well-known strictly empirical correlations are the correlation from Shah (1982) and Kandlikar (1983) [47]. The original Kandlikar correlation was improved by himself in 2004, which makes it applicable for minichannels [48]. Chen is the pioneer of the superposition correlation. The Gungor & Winterton correlation (1987) [49] is an improved one of the original correlation from Chen (1966) [50]. The superposition correlations are based on the contribution of nucleate and convective boiling. The background has already been described in Section 2.2.3 and an indication for the heat transfer coefficient is shown in Figure 2.9. These two figures can be combined to one plot for the heat transfer coefficient according to several superposition correlations. The third method is based on flow pattern based models and the founders were Kattan and Thome which have already been mentioned in Section 2.2.5. With this method, the heat transfer correlations hold specifically for different flow regimes.

Over the years, many new empirical correlations have been added, but no universal ones. However, from the above correlations, Kandlikar shows the best results for minichannels in two-phase MPL thermal management demonstrators at NLR. In addition, it is one of the best applicable correlations for ammonia as a refrigerant [51]. Other correlations used in this research for comparison are those of Gungor & Winterton and the Kim

& Mudawar (2013) correlation [52] [53]. Details of the used empirical correlations are described in Appendix A.2. Since Kandlikar is the most used in this research, the empirical correlation is briefly summarized below.

$$h_{tp} = \max \begin{cases} h_{tp,nbd} = \left[0.6683\mathrm{Co}^{-0.2}(1-x)^{0.8} + 1058.0\mathrm{Bo}^{0.7}(1-x)^{0.8}\right] h_l \\ h_{tp,cbd} = \left[1.136\mathrm{Co}^{-0.9}(1-x)^{0.8} + 667.2\mathrm{Bo}^{0.7}(1-x)^{0.8}\right] h_l \end{cases} \tag{2.9}$$

Where the subscript *tp* means two-phase, *nbd* means nucleate boiling dominant and *cbd* means convective boiling dominant. Co is the Convection number and Bo is the Boiling number. Again, the details are in Appendix A.2. To give an illustration of the different empirical correlations, they are plotted in Figure 2.13.

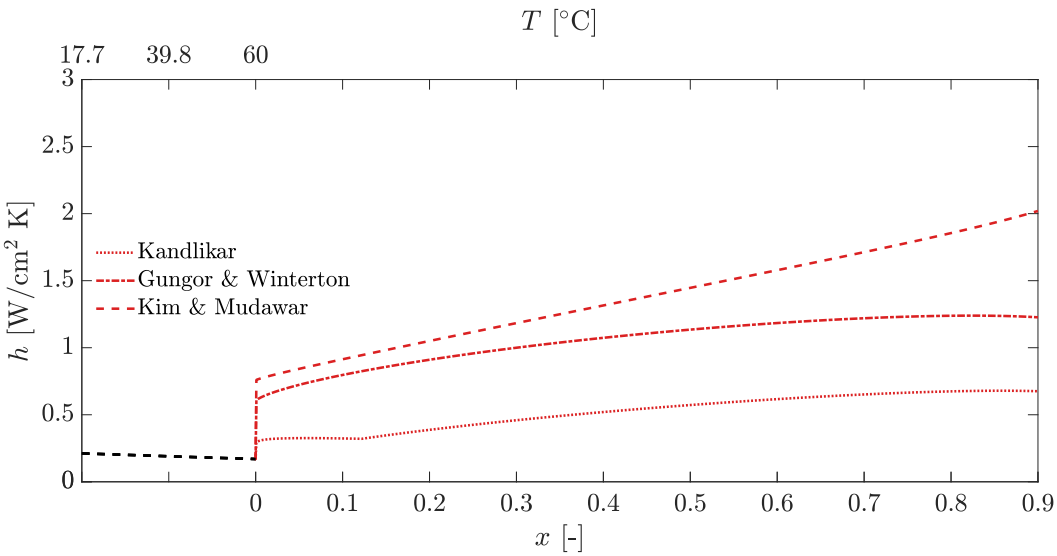

Figure 2.13: Heat transfer coefficient plot for different empirical correlations with ammonia as refrigerant. A saturation temperature of 60 °C, a 1 mm internal diameter, a mass flow of 0.1 g/s, and a heat flux of 1 W/cm^2 are used.

It is plotted for ammonia as a coolant with a saturation temperature of 60 °C, a mass flow of 0.1 g/s, and a heat flux of 1 W/cm^2. The y-axis represents the heat transfer coefficient. The upper x-axis contains the theoretical liquid temperature up to the boiling point. When the saturation temperature is reached, the liquid starts boiling and the lower x-axis with the vapor mass fraction rises. These axes are also used in other scientific papers and studies [54]. The black line represents single-phase heat transfer as described in the previous section. In addition, it can be seen that the turning point between nucleate and convective boiling in the Kandlikar correlation is around 0.12. Due to the low heat flux, no dry-out can be seen in the Kim & Mudawar correlation. The two-phase correlations are designed for saturated flow boiling. Theoretically, a liquid boils at $x = 0$, hence the vertical line in the figure. In practice and according to Figure 2.9, there is a transition region between the single-phase and the two-phase heat transfer coefficient. Since this research mainly focuses on the onset of boiling, there is more interest in low vapor mass fractions. A zoomed plot is shown in Figure 2.14 with a heat flux of 10 W/cm^2 added.

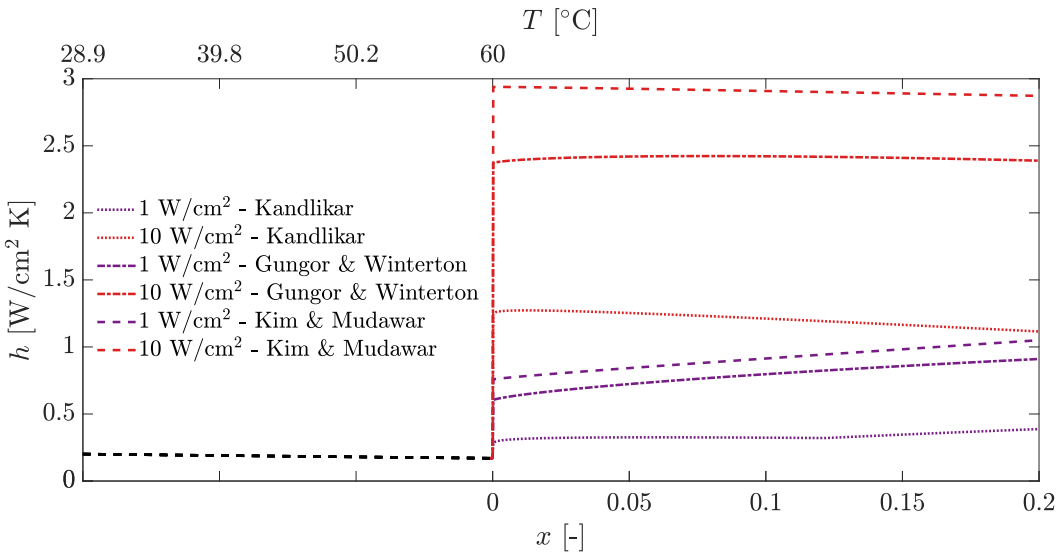

Figure 2.14: Heat transfer coefficient plot for different empirical correlations with ammonia as refrigerant at low vapor mass fractions. A saturation temperature of 60 °C, a 1 mm internal diameter, and a mass flow of 0.1 g/s are used.

2.4 Subcooled liquid

As mentioned in previous chapter and shown in Figure 2.7, there is a transition region between liquid and saturated flow boiling. This region is also referred as subcooled flow boiling and a zoomed representation is shown in Figure 2.15.

When the wall temperature T_{w} reaches the saturation temperature, the bulk flow is still liquid. From location B and C in the figure, a certain amount of wall superheat is required to activate the nucleation sites in the cavities and scratches at the wall [33]. Location C refers to the ONB and the moment that a bubble can exist on the heated wall. Small cavities or cracks in the heated wall serve as nucleation sites and a bubble may grow or condense in the liquid. If the bubble detaches from the surface while the average bulk temperature remains below the saturation temperature, this phenomenon is called subcooled boiling [19]. Note that the vapor mass fraction x is still less than 0. This region is characterized by significant radial temperature gradients, with bubbles forming at the heated wall and subcooled liquid flowing near the center of the tube [32]. The thickness of the bubble region increases farther downstream, and eventually, the core of the liquid reaches the saturation temperature of the fluid. Bubbles can then exist at any radial location, also known as homogeneous nucleation. From point H there is saturated flow boiling starting from a vapor mass fraction of $x = 0$.

Figure 2.8 shows a difference in the axial temperature gradient. So, the temperature rise in the downstream direction of the tube, i.e. in the $\mathrm{d}T/\mathrm{d}x$ direction. The bottom picture applies to relatively high heat fluxes and has a higher axial temperature gradient. As a result, the wall temperature reaches saturation temperature sooner. A higher heat flux also results in a lower radial temperature gradient and thus the bulk temperature in the center of the channel will rise faster. In this research, the term subcooled liquid represents that the bulk flow is liquid and at the wall, two-phase heat transfer is measured. Subcooled liquid has higher local heat transfer coefficients so that the heat can be dissipated better into the fluid [20].

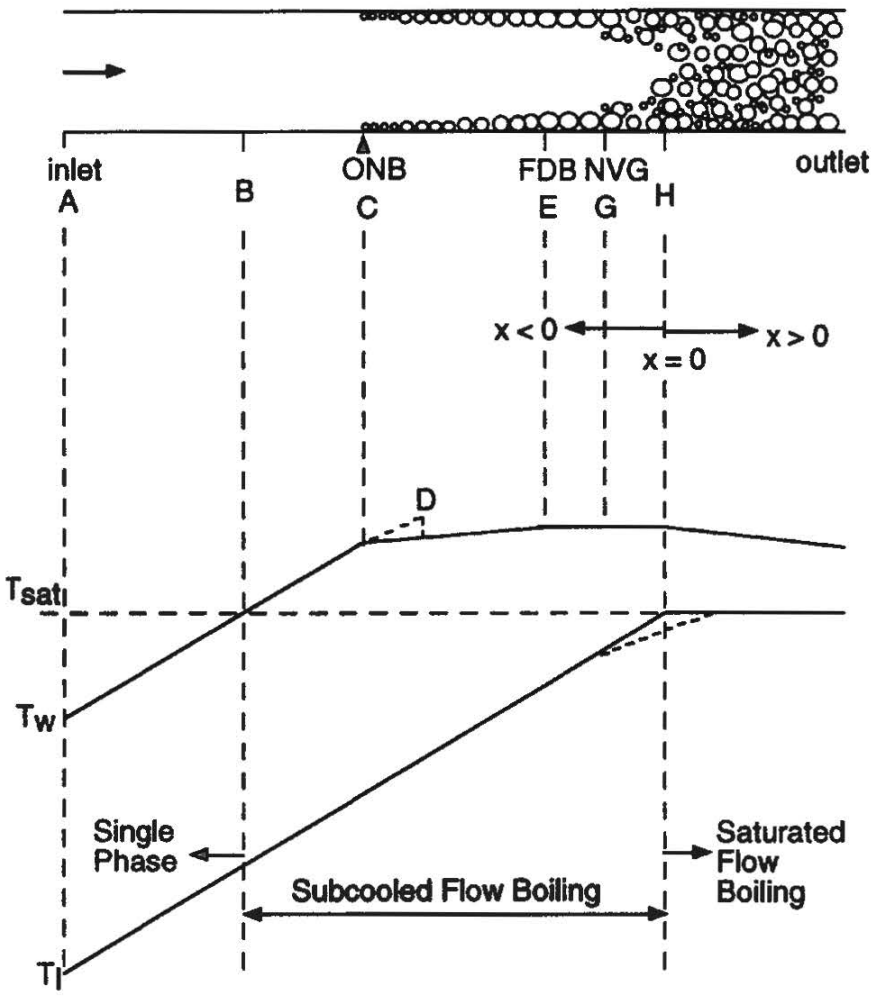

Figure 2.15: Schematic representation of subcooled flow boiling [33].

To ensure the flow enters the evaporator in two-phase state with a vapor mass fraction slightly above $x = 0.0$ and below $x = 0.1$. As shown in Figure 2.1, a recuperator and/or a preheater can be used to heat the liquid near the saturation temperature. The disadvantages are that a preheater entails extra power consumption and a recuperator extra mass. Therefore, it is advantageous to enter the evaporator section of a two-phase MPL thermal management with subcooled liquid. Entering the evaporator section as liquid also means a lower liquid heat transfer coefficient. This can result in higher wall temperatures and therefore higher heat load temperatures. An adverse effect can be overheating of the heat load. However, even worse would be that the liquid temperature exceeds the saturation temperature. This is covered in the next section.

2.5 Superheated liquid

In contrast to subcooled liquid, superheated liquid is an undesirable phenomenon in two-phase MPL thermal management systems. The phenomenon is shown in Figure 2.16, where vaporization takes place at the saturation temperature. The definition of superheated liquid is a liquid at a temperature and pressure at which it should be a vapor. In fact, the phenomenon superheated liquid can give rise to the occasion of liquid with a local temperature that is higher than the pressure-dependent saturation temperature. The superheated liquid exists temporarily and is an unstable process.

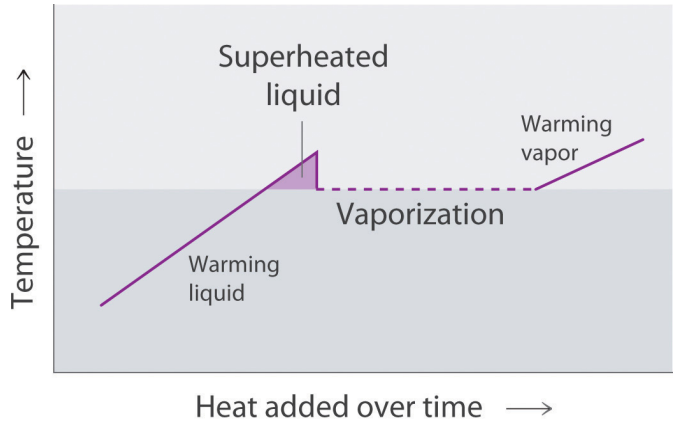

Figure 2.16: Illustration of the superheated liquid phenomenon over time with a constant heat flux [55].

Referring to Figure 2.8, the top picture applies to relatively low heat fluxes and the bottom picture applies to high heat fluxes. Experience within NLR with different previous projects about two-phase MPL thermal management demonstrators shows that superheated liquid occurs at relatively low heat fluxes and subcooled liquid at higher heat fluxes.

2.5.1 Uniform temperature distribution in radial direction

To make an estimate for superheated liquid, several assumptions have been made. First, a uniform temperature distribution in the radial direction is assumed for spherical bubbles. The reason for the superheated liquid is that inside a vapor bubble, the pressure (and therefore the saturation temperature) is slightly higher than outside the bubble. Suppose a vapor bubble inside a liquid as shown in Figure 2.17.

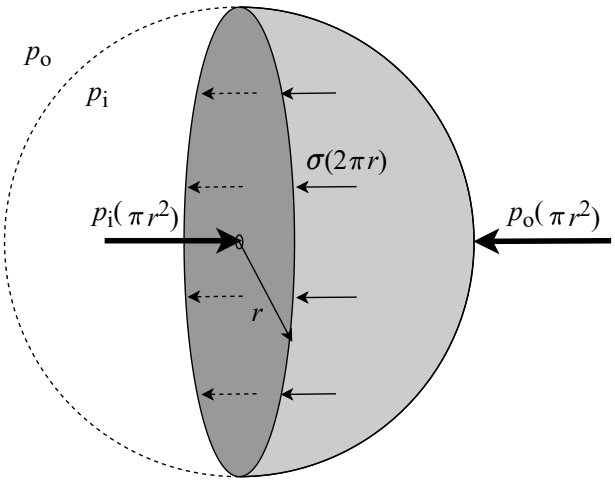

Figure 2.17: Cross section of a small vapor bubble with internal pressure p_i and external pressure p_o. The black arrows indicate the surface tension σ. As a result of the surface tension, the pressure inside the bubble is higher than outside the bubble.

The pressure jump between the vapor bubble and the liquid is related to the radius of the bubble and the surface tension. Equation 2.10 shows the Young-Laplace equation

[56].

$$2\pi r\sigma + p_o \pi r^2 = p_i \pi r^2 \quad \longrightarrow \quad \Delta p = p_i - p_o = \frac{2\sigma}{r} \tag{2.10}$$

This increase in pressure results in an increase in the saturation temperature inside the bubble. Later in the report, the equation below is called the modified Young-Laplace equation [57].

$$\Delta T_{\text{sat}} = \frac{2\sigma}{r} / \left(\frac{\partial p}{\partial T}\right)_{\text{sat}} \quad \longrightarrow \quad T_{\text{sup}} = \Delta T_{\text{sat}} \tag{2.11}$$

For example, suppose a small ammonia vapor bubble of ammonia at 60 °C with a radius of $1 \cdot 10^{-7}$ m. $\left(\frac{\partial p}{\partial T}\right)_{\text{sat}}$ is also known as the Clausius-Clapeyron relation [56] and is a fluid property which can be obtained from MATLAB and REFPROP. For ammonia at 60 °C it is 0.64 bar/K and the surface tension is 0.013 N/m. This results in a superheated liquid temperature inside the bubble of 4.0 °C, which is 4.0 °C above the saturation temperature. This means that if the superheat is below 4.0 °C, the vapor temperature inside the small bubble is below the local boiling temperature and any vapor inside the bubble will condense into liquid. When the superheat is above 4.0 °C, the temperature is above the local boiling temperature and the bubble will grow and the fluid will quickly start to evaporate.

A fluid property that influences the superheated liquid temperature is surface tension. The typical two-phase refrigerants from Table 2.1 are shown in Figure 2.18. Water is also shown for comparison because it is often used as a liquid refrigerant. As the temperature increases, the surface tension decreases, which means that the superheated liquid temperature decreases.

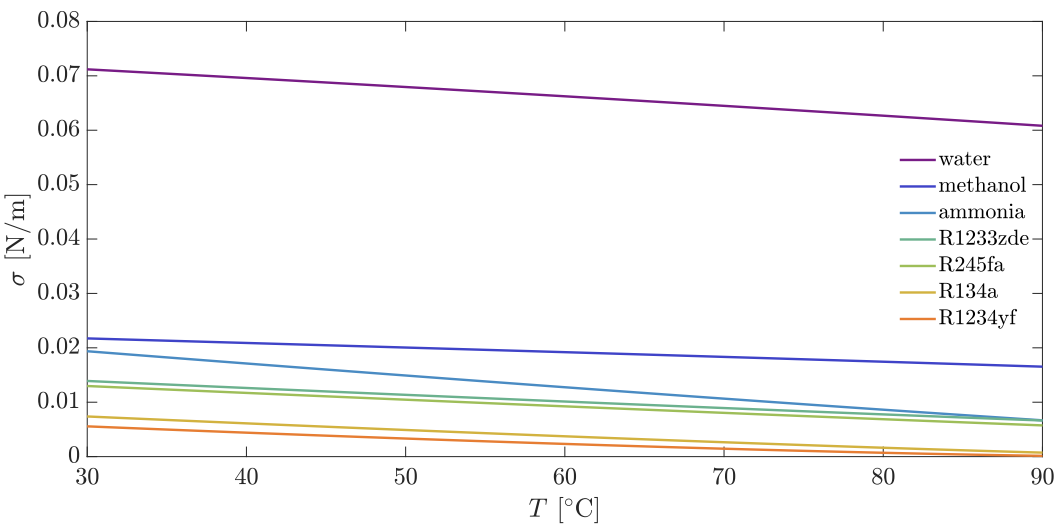

Figure 2.18: The surface tension plotted against the temperature for typical two-phase refrigerants from Table 2.1 and water for comparison.

The superheated liquid temperature for typical two-phase refrigerants at varying bubble radii are shown in Figure 2.19. The figure shows that methanol is most sensitive to superheating. The plot has been converted to logarithmic axes which is shown in Figure 2.20.

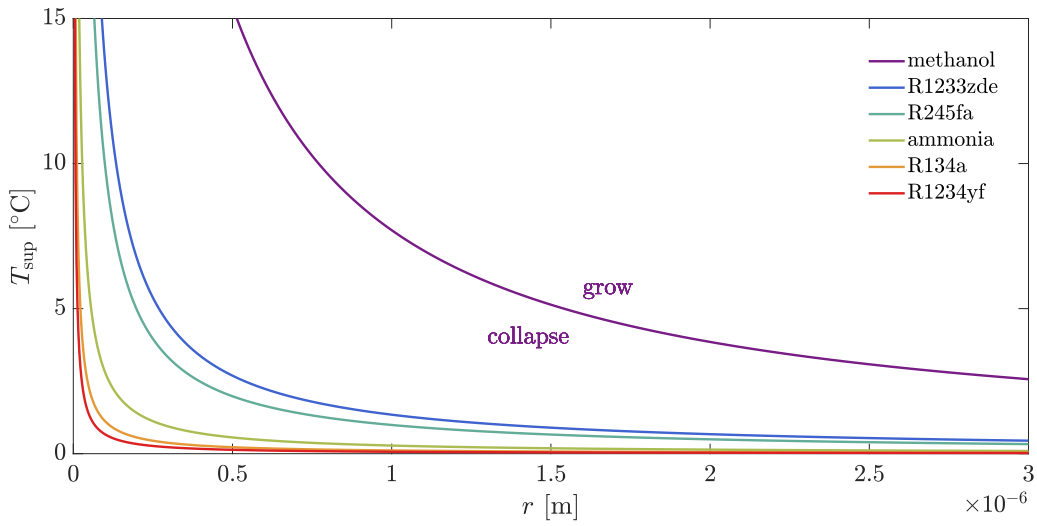

Figure 2.19: A prediction for the superheated liquid temperature for a range of nucleation bubble radii for typical two-phase refrigerants.

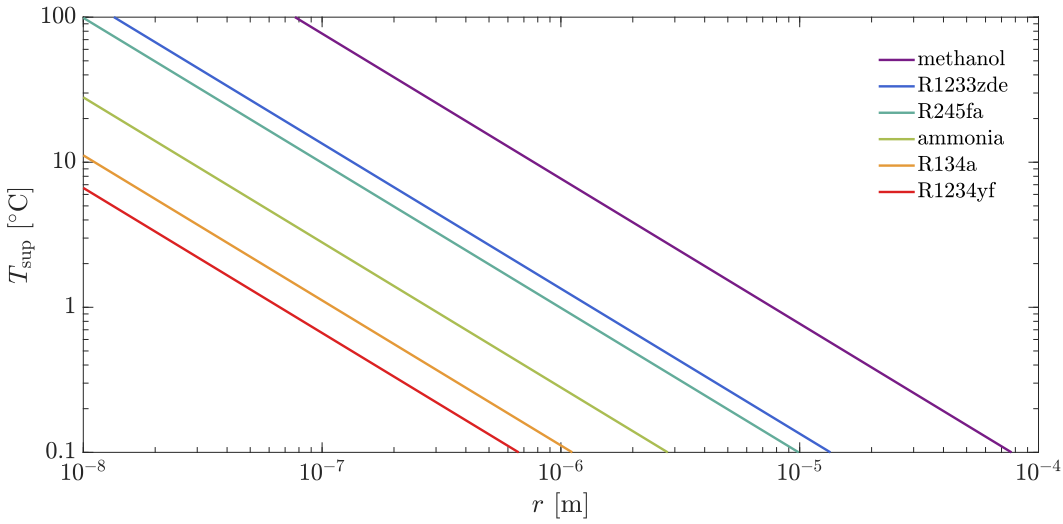

Figure 2.20: A prediction for the superheated liquid temperature for a range of nucleation bubble radii for typical two-phase refrigerants with logarithmic axes.

The influence on the superheated liquid temperature of different typical operating temperatures in two-phase MPL thermal management systems is shown in Figure 2.21. What was already known from Figure 2.18 is also visible here; at a higher saturation temperature, the superheated liquid temperature is lower. However, it should be taken into account that this is a first assumption to estimate the superheated liquid temperature. A nucleation bubble size corresponds to a certain superheated liquid temperature.

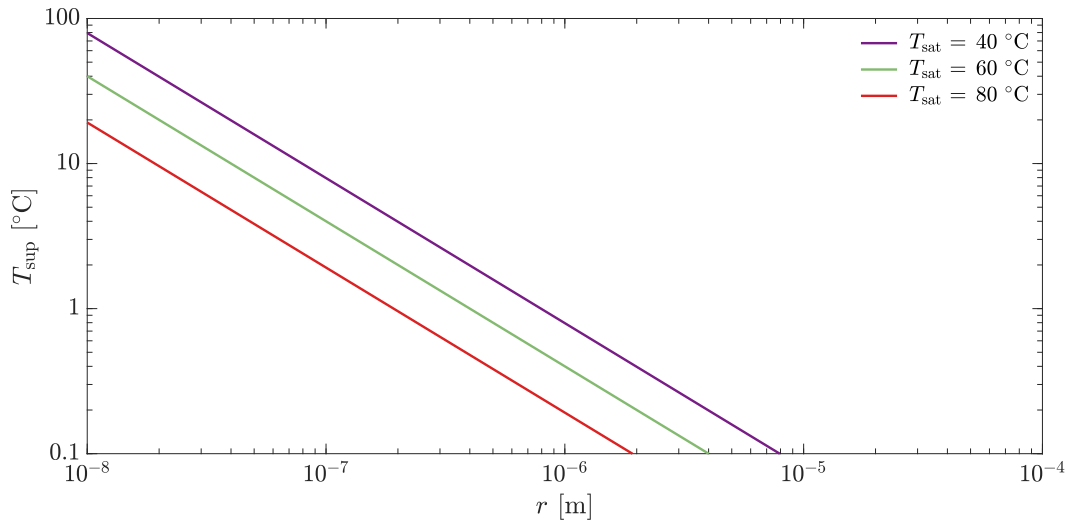

Figure 2.21: A prediction for the superheated liquid temperature for a range of nucleation bubble radii for ammonia and different saturation temperatures.

2.5.2 Radial temperature distribution

Heterogeneous nucleation where a bubble arises from a heated surface was not considered. Therefore, the theory behind non spherical bubbles and the contact angle of bubbles with the tube wall has not been examined. Instead, an analysis was made of the radial temperature gradient from the tube wall to the center of the tube. As shown in Figure 2.15, the flow starts with only bubbles at the wall. Because of this observation, it is interesting to predict the radial temperature difference between the bulk liquid and the liquid near the wall. If there is a big radial temperature distribution in the tube, it is expected that there is a higher chance that superheated liquid occurs and also a higher superheated liquid temperature. A possibility to predict the liquid temperature is to use the convection-diffusion equation in combination with the Hagen-Poiseuille flow. The made assumptions are:

- Axi-symmetric flow;
- Incompressible flow;
- Steady flow;
- No-slip at the boundary;
- Zero gravity.

The convection-diffusion equation in cylindrical coordinates [58] become:

$$\rho c_p u(r) \frac{\partial T}{\partial L} = k \frac{1}{r} \frac{\partial}{\partial r} \left(r \frac{\partial T}{\partial r} \right) \tag{2.12}$$

Where $u(r)$ is the Hagen-Poiseuille flow velocity [39], which is only valid for laminar flow through a channel of uniform circular cross-section:

$$u(r) = 2 \left[1 - \left(\frac{r}{r_0} \right)^2 \right] u_{\text{mean}} \tag{2.13}$$

With two boundary conditions and an initial condition, respectively:

$$\left.\frac{\partial T}{\partial r}\right|_{r=0} = 0 \tag{2.14}$$

$$\left.\frac{\partial T}{\partial r}\right|_{r=r_0} = \frac{q}{k} \tag{2.15}$$

$$T(L=0) = T_{\text{in}} \tag{2.16}$$

The fluid temperature is given as T, and flow velocity is given as $u(r)$, depending on the radial coordinate r. The first boundary condition is due to symmetry at the center of the tube at $r = 0$. The heat flux on the wall at $r = r_0$ is given by q. The radial temperature distribution in a circular channel can be calculated, along the length (L) of the tube. The partial differential equation (PDE) can be solved numerically with the MATLAB PDE solver. Here we can use different heat fluxes, mass flows, and inlet temperatures to look at the different influences. This will be discussed in Chapter 4 about modelling. In addition, this method can also be used for subcooled liquid where the evaporator is approached with a lower inlet temperature than the saturation temperature.

The main goal of this research is to investigate if it is possible to reduce superheated liquid temperature or ultimately, prevent superheated liquid completely in a two-phase MPL thermal management system. As mentioned in Chapter 1, several mechanisms such as rough walls [20], the addition of nanofluids [21], and the addition of dissolved gases [22] [23] [24] can be introduced to a two-phase MPL system to increase the number of bubble nucleation sites, and thus improve the onset of boiling. Since this research only deals with dissolved gases in refrigerants, the next section will discuss the solubility of refrigerants.

2.6 Solubility of refrigerants

Table 2.1 lists the typical refrigerants in a two-phase MPL thermal management system. In this research, it is necessary to know the solubility of a dissolved gas in a refrigerant. The refrigerant is the solvent and a dissolved gas is the solute. First, a general look is taken at the solubility of non-condensable gases (NCGs) in liquids. The definition of NCGs is that they are gases that do not want to condense into a liquid within the operating temperatures of the refrigeration system. However, for a two-phase MPL thermal management system, the gases must be dissolved in the liquid refrigerant after the condenser to prevent cavitation of the pump. Well-known examples of NCGs are air, nitrogen, hydrogen, and carbon dioxide [59]. Over the lifetime of a system, NCGs can negatively impact a system. For example, that NCGs spoil the energy efficiency of a compression vapour refrigerating circuit [60]. However, this research avoids the disadvantages and the advantages that emerge in the evaporator section according to the hypothesis. An example of success is that dissolved air resulted in a significant reduction in wall temperature [57].

2.6.1 Henry's law

Henry's law can be used to describe the solubility of gases in liquids. There are many fundamental types and variants of Henry's law [61]. A large variation of Henry's law constants are possible where different unit are used, for instance, dimensionless, in atm,

or mol/Latm. Henry's law is a gas law that states that the amount of dissolved gas in a liquid is proportional to its partial pressure above the liquid [62]. The simplified form of Henry's law is given in Equation 2.17.

$$H = \frac{X}{p} \tag{2.17}$$

Where H^{cc} is Henry's constant, X is the mole fraction, and p is the partial pressure of the dissolved gas. Henry's constant is not constant when the temperature in a system changes, then Henry's constant also changes. In literature, much is known about gases dissolved in water and not about gases in refrigerants. Hence, first an example of gases in water at 25 °C. Henry's constant for oxygen, hydrogen, carbon dioxide, and nitrogen is 43000, 71000, 1600, and 91000 atm, respectively. These values are plotted and shown in Figure 2.22.

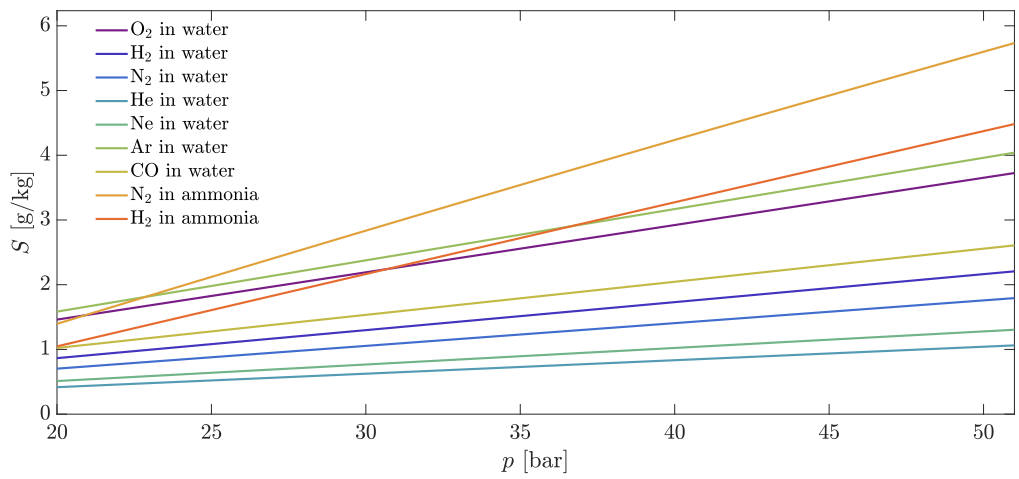

Figure 2.22: Henry's law for different gases in water and the experimental data for nitrogen and hydrogen in liquid ammonia (NH_3).

Where S is an easy-to-use unit for solubility. The trend is that the solubility increases as the pressure increases at a constant temperature. This also applies to nitrogen and hydrogen gas in liquid ammonia, which comes from experimental data described in the next section.

2.6.2 Experimental data

There is virtually no experimental data available in the literature on the solubility of NCGs in the typical two-phase refrigerants. Usually, it concerns the solubility of refrigerants in water, so not the desired data. Furthermore, the Henry's constant for nitrogen dissolved in various refrigerants is very limited [62]. However, there is only one paper dating from 1937 that tabulates the solubility of nitrogen and hydrogen in liquid ammonia [63]. This table has been converted into a contour plot and interpolated using MATLAB, which is shown in Figure 2.23.

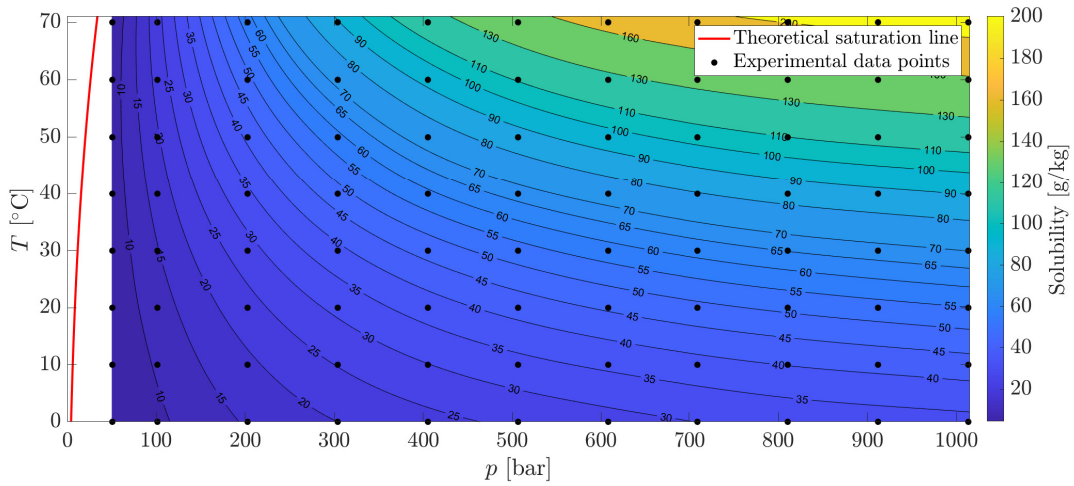

Figure 2.23: Interpolated experimental data for the solubility of nitrogen in liquid ammonia.

The solubility units have been converted from cc/g to the more practical unit g/kg. The original data is plotted and shown in Appendix B. The red line represents the theoretical saturation line for ammonia which is the transition from liquid to vapor. The black dots are the experimental data points from the table in the paper. The paper deals with solubility at very high pressures, which is not relevant in a two-phase MPL system. Hence the above data has been extrapolated in MATLAB to lower pressures which are in the range of interest. The extrapolated data is shown in Figure 2.24.

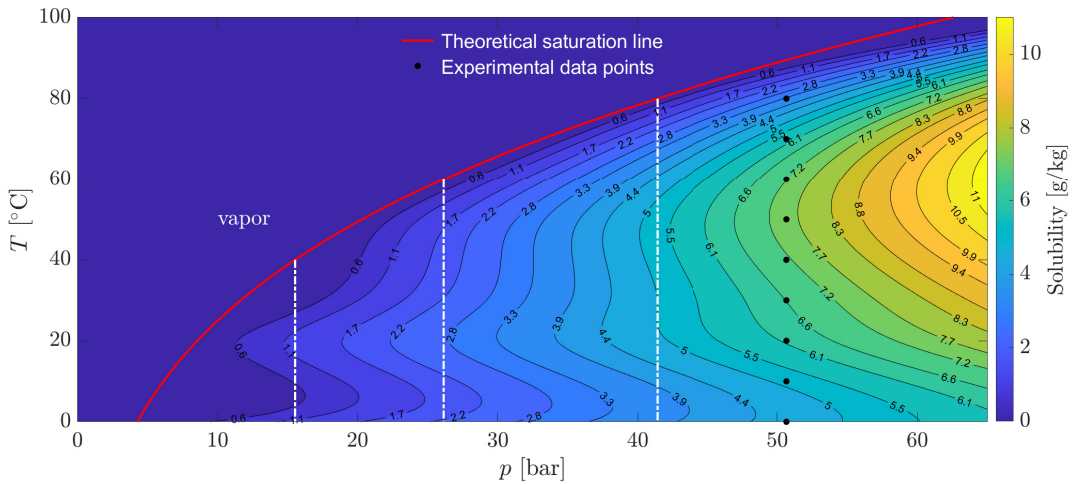

Figure 2.24: Extrapolated experimental data for the solubility of nitrogen in liquid ammonia.

The added vertical white lines represent the corresponding system pressures of interest which will be covered in the experimental part of this research. These system pressures are 15.5, 28.1, and 41.4 bar with corresponding saturation temperatures of 40, 60 and 80 °C. It is visible that there are still experimental data points at 50.7 bar, the data to the left of this is therefore entirely based on extrapolation. Below approximately 40 °C the data shows wobbly behavior, but towards the saturation line, the solubility becomes zero. Since the temperature before the evaporator section is near the saturation temperature, there is only interest in the solubility near the saturation temperature. As

a result, experiments should be carried out not too far from the saturation temperature to avoid getting into wobbly behavior. Because of the assumed constant system pressure near the evaporator section in a two-phase MPL thermal management system, Figure 2.24 is converted into a S-T diagram.

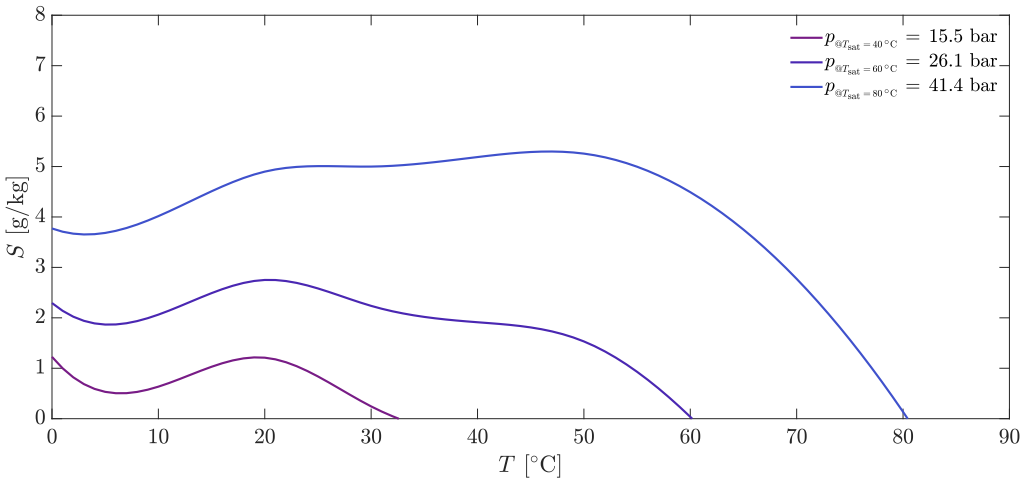

Figure 2.25: Solubility vs temperature plot with the constant system pressures as range of interest.

This clearly shows the wobbly behavior at low temperatures. It also provides a good insight into the solubility as the refrigerant flows towards the evaporator section in a two-phase MPL thermal management system. A higher working pressure results in a higher solubility, which leads to more possible nucleation sites to stimulate the start of the boiling process. However, a disadvantage of higher working pressure (and thus a higher saturation temperature) is the lower superheated liquid temperature as shown in Figure 2.21 for ammonia.

The above solubility data is all that is available in literature. Despite the uncertainty due to the extrapolation, it will still be applied and used in the remainder of the study. This concludes the theoretical section and the research question is repeated below:

- *Do dissolved gases in refrigerants have a reducing effect on the superheated liquid temperature?*

Based on the above section and the available materials and experience within NLR, this research will only use nitrogen gas as NCG and ammonia as refrigerant. Due to the uncertainty in solubility data and the lack of fully reliable empirical correlations for predicting boiling heat transfer [35], this research is limited to qualitatively demonstrating that dissolved gases reduce the superheated liquid temperature.

3

Experimental setup

From the previous chapter, it has become clear that the main research question will be answered using an experimental setup with ammonia as refrigerant and nitrogen as NCG. An existing two-phase MPL thermal management demonstrator that will be used is described in this chapter and the necessary adjustments such as the nitrogen injection system will be explained. In addition, single-phase flow measurements are made to verify the setup, which are compared with analytically calculated results. Finally, a test plan is described to measure subcooled and superheated liquid and the nitrogen injection steps will be described.

3.1 Ammonia

First, a brief description of the used refrigerant. According to Section 2.1.2 and Table 2.1, ammonia is an extremely suitable refrigerant in two-phase MPL thermal managemant systems. However, ammonia is mostly used for high-pressure applications and is toxic. Therefore, leak tightness and pressure resistance are a priority in the design process of the setup. The chemical formula to produce ammonia is shown in the equation below.

$$N_2 + 3H_2 \longrightarrow 2NH_3 \tag{3.1}$$

NH_3 is produced by the Haber process and is the main industrial procedure for production of ammonia today. The chemical reaction of nitrogen with hydrogen using a metal catalyst under high pressures (150-200 bar) and temperatures (400-500 °C) [64].

The existing setup has already been used with ammonia and the phenomenon of superheated liquid has also been observed in this setup. At that time, no further consideration was given to specific values of the superheated liquid. For refrigerants, only the solubility of ammonia is present in literature, hence this is a logical choice to use in this research.

3.2 Setup design

The flowchart of the existing setup as used in previous NLR projects with ammonia is shown in Figure 3.1. It is an fundamental setup and not a real cooling system. The test tube represents part of the evaporator section. It is clammed between two copper blocks by which an electrical current can be directed through the tube. This electrical current heats the test tube and provides the desired amount of heat flux on the fluid-tube interface. The fluid has to enter the test tube with a specified inlet temperature which is achieved by the preheater. In this preheater, the desired inlet temperature is generated by sending an electrical current through the preheater tube (i.e. similar to the test tube). With this setup, the heat transfer coefficient in the test tube can be measured as a function of vapor mass fraction, heat flux, mass flow, and temperature. The T and p symbols are temperature and pressure sensors in the setup.

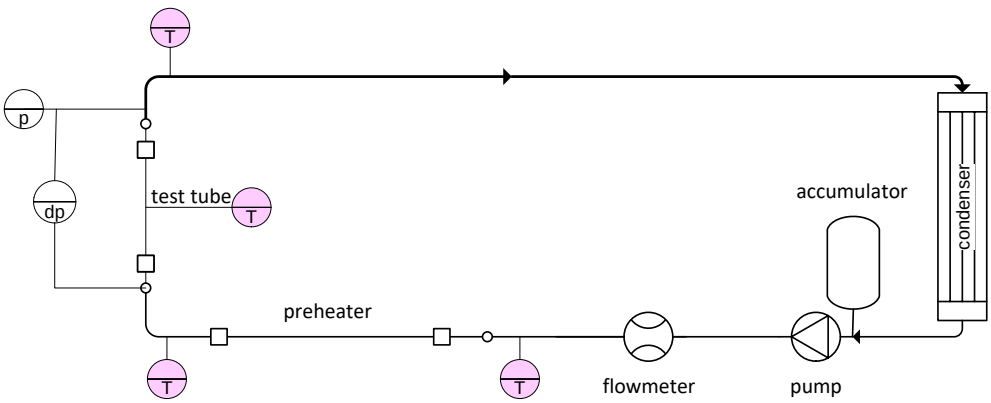

Figure 3.1: Schematic flowchart of the two-phase MPL demonstrator.

An image of the setup in the NLR lab is shown in Figure 3.2. The main components are visible except for the preheater and the evaporator. These are located in the thermostated plates which are controlled to keep the ambient temperature at the saturation temperature. This simulates the environment of an object to be cooled and minimizes heat leak. The thermostated plates are connected to a condenser bath which contains a mixture of water and ethylene glycol. These condenser baths have a much higher thermal mass than the loop volume. In previous NLR experiments, the preheater was located in the first thermostated plate and the evaporator in the second thermostated plate. Later, this was combined in the second thermostated plate and the first plate became obsolete. The condenser is a spiral tube-in-tube heat exchanger which is also connected to a condenser bath. The location where the measurements take place is at the evaporator section. Figure 3.3 shows a photo of the second thermostated plate with the preheater and test tube with only a part of the isolation. In operation, the tubing is completely insulated and another plate is placed on top. Therefore the entire test section is completely isolated from the environment as shown in Figure 3.2.

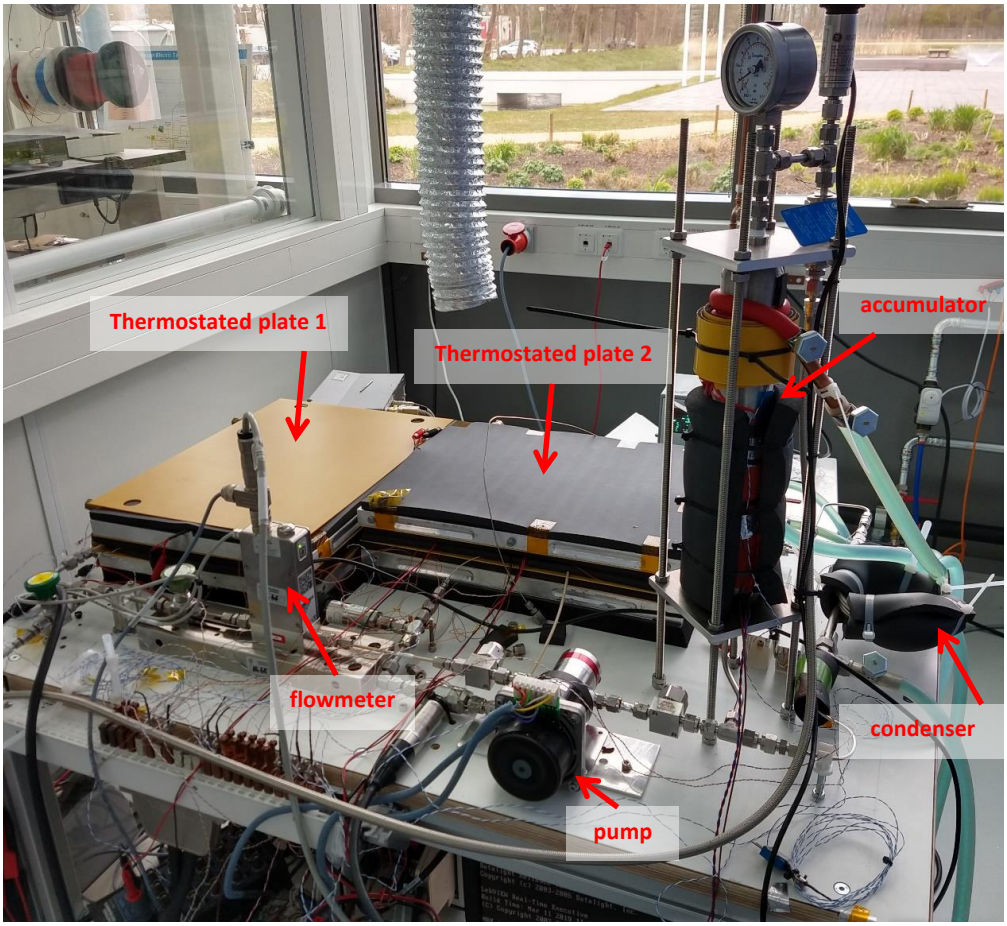

Figure 3.2: Image of the existing two-phase MPL demonstrator.

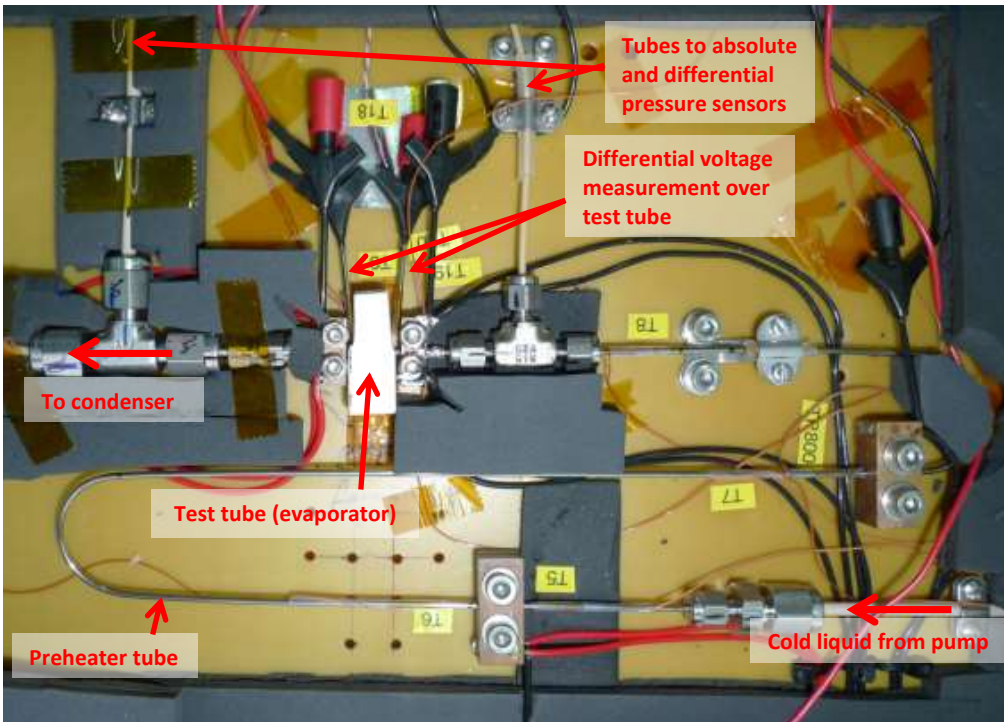

Figure 3.3: Part of the current setup design of a two-phase MPL demonstrator.

Figure 3.3 contains the test tube with insulation, the figure below shows a photo of the thermocouple without the ceramic insulation around the test tube.

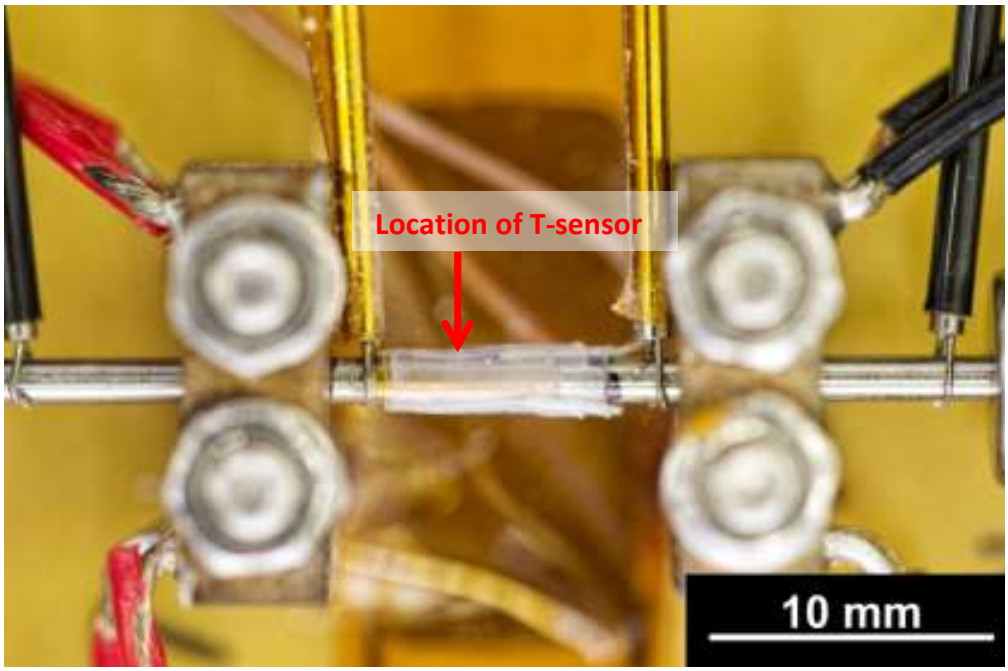

Figure 3.4: Photo of the test tube section without insulation.

The current experimental setup is suitable for the typical operating temperatures of a two-phase MPL thermal management system. As described in Chapter 2, this study uses 40, 60 and 80 °C as operation temperatures.

3.2.1 Heat transfer calculation in the setup

The goal in this research is to qualitatively demonstrate that dissolved gases reduce the superheated liquid temperature. In addition, it is desired to show the difference in subcooled liquid and superheated liquid temperature for varying parameters like saturation temperature and heat flux. This will be demonstrated using the heat transfer coefficient. Despite the relatively simple formula given in Equation 2.5, the heat transfer coefficient between the fluid and the evaporator wall is not so simple to measure accurately. Figure 3.5 shows a cross section of a circular tube, used as evaporator section.

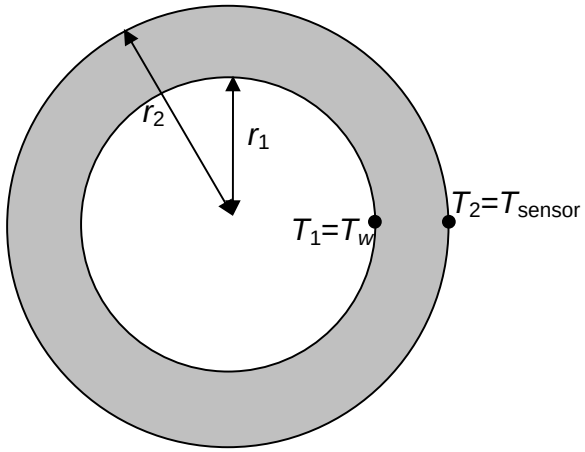

Figure 3.5: Cross section of the test tube.

Where r is the radius of the circular test tube. With r_1 as inner radius and r_2 the outer radius. The experimental setup uses a 1/16" tube for the evaporator section so $r_2 = 1.5875$ mm, the inner radius $r_1 = 1$ mm. It is assumed that the tube is uniformly heated in radial and longitudinal direction by sending a high electrical current through the tube. The total amount of generated heat in the tube can be calculated with Equation 3.2.

$$P = UI \tag{3.2}$$

Where U is the voltage and I is the current in ampere. The heat flux at the inner wall is shown in Equation 3.3.

$$q = \frac{P}{2\pi r_1 L_{\text{tube}}} \tag{3.3}$$

Basically, q in W/cm^2 is the power uniformly distributed over the surface area. L_{tube} is the length of the heated test tube in meters. The temperature sensor (T_{sensor}) is located at the outside of the tube wall as shown in Figure 3.5. However, for accurate heat transfer coefficient estimations, the temperature at the fluid-wall interface is desired. Fortunately, via analytical derivation, the outer wall temperature can be calculated from the inner tube wall temperature and geometric information. This results in the equation below. A detailed derivation can be found in Appendix C.

$$T_{\text{wall}} = T_{\text{sensor}} + \frac{\dot{q}}{4k}\left(r_2^2 - r_1^2\right) - \frac{\dot{q}}{2k} r_2^2 \ln\left(\frac{r_2}{r_1}\right) \tag{3.4}$$

For clarity, Equation 2.5 is repeated below. Obtaining the wall temperature is explained above. The missing parameter is the bulk fluid temperature. The temperature cannot be measured in the center of the evaporator. That is why the liquid temperature is measured before and after the evaporator, when no power is supplied. The average of these two temperatures is taken, which should not differ too much from each other. Due to the thermostated plates which keep the ambient temperature at the saturation temperature, heat leakage is minimized and confirms the assumption.

$$h_{\text{fluid-wall}} = \frac{q}{(T_{\text{wall}} - T_{\text{fluid}})} \tag{3.5}$$

Where the fluid temperature becomes:

$$T_{\text{fluid}} = \frac{T_{\text{liquid,tube,in}} + T_{\text{liquid,tube,out}}}{2} \tag{3.6}$$

A schematic representation of the temperature sensors on the wall is given in Figure 3.6.

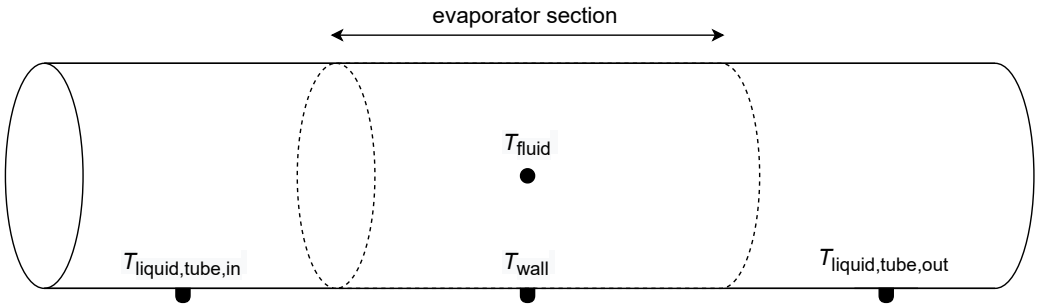

Figure 3.6: Schematic representation of the temperature sensors on the wall.

3.2.2 System volume estimation

The amount of vapor ammonia at atmospheric pressure that goes into the setup is 180 gr, which is measured when filling the system. During operation, there is liquid and vapor ammonia in the loop, assuming that the tubing and components from condenser to evaporator are in a fully liquid state. From datasheets and manual measurements, the volume per part has been estimated. It follows that the accumulator contains 97% of the loop volume. This is important to know for the amount of nitrogen gas to inject into the experimental setup. The current setup was used in a previous project to measure the heat transfer coefficient in the evaporator section. Therefore, the accumulator volume is so large compared to the rest of the loop volume to have no temperature instabilities.

3.3 Modified setup

Firstly, it is necessary that subcooled and superheated liquid can be measured with the setup. For this, the inlet temperature had to be more variable. This is solved by sticking the PEEK tubing to the first thermostated plate with aluminum tape which no longer had any function. This is shown in Figure 3.7, where the upper part (second thermostated plate) contains the preheater and the evaporator. PEEK tubing has been used in this part of the setup because it is flexible. Before and after the preheater and the evaporator PEEK tubing is used for the electrical insulation. Moreover, PEEK is an increasingly used material in the aerospace industry due to these benefits [65].

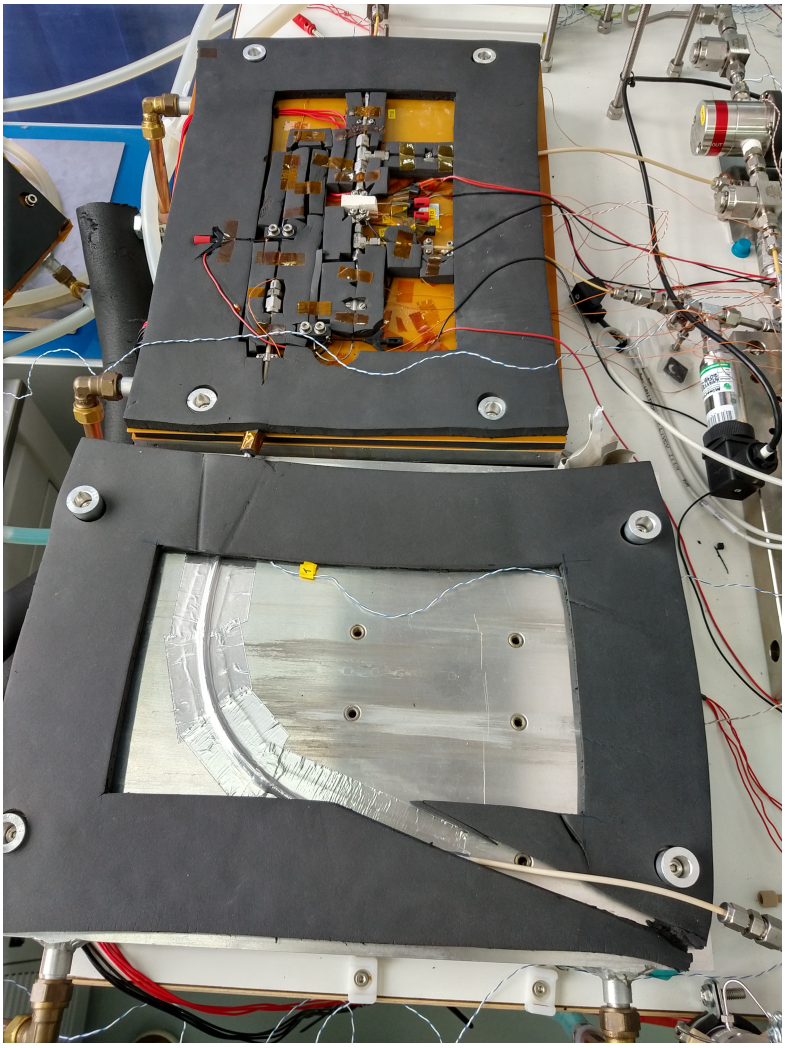

Figure 3.7: Photo of the modified thermostated plate in the setup.

3.3.1 Non-condensable gas injection system

To make measurements with dissolved gases in refrigerants, an injection system must be added to the current setup. This injection system has a requirement that it can supply a small amount of gas to the system. It is too labour-intensive to refill the setup each time with a different amount of dissolved gas. If the hypothesis is correct and it will be applied in the future in two-phase MPL thermal management systems then a certain amount of gas is dissolved in the refrigerant beforehand. Since the hypothesis that dissolved gases in refrigerants can have a reducing effect on the superheated liquid

temperature had already been considered within NLR, an injection system was already in stock. The injection system was analyzed and assessed whether it would also be applicable in the current setup. Available volumes for this injection system are 0.01, 0.02, 0.25, 2 and 10 mL. The injection system is a so-called six port injection valve (SPIV) and the theoretical working principle is shown in Figure 3.8.

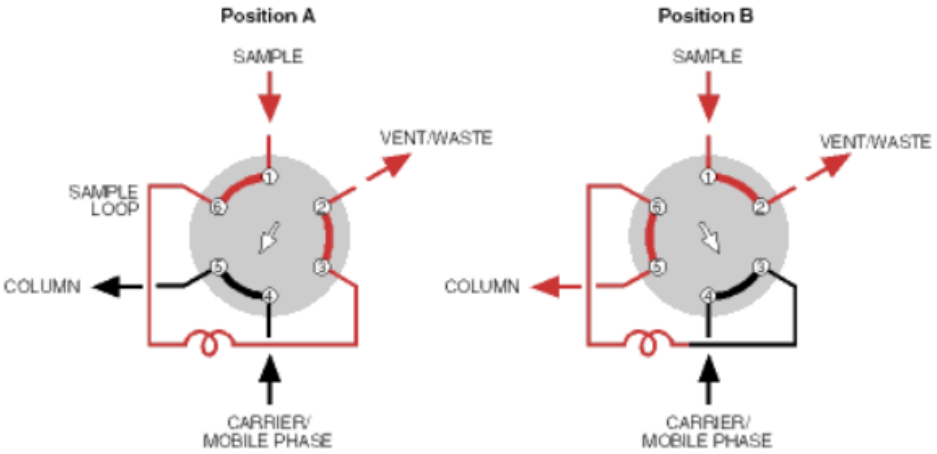

Figure 3.8: Theoretical working principle of the SPIV [66].

Where position A is the 'closed' phase, here the sample volume is filled with nitrogen gas. When the SPIV is set to position B for the short time unit, the nitrogen gas will enter the setup and the SPIV is 'open'. Before the SPIV is implemented, a functional test is done. This is described in Appendix D. Contrary to the figure above, the "column" and "vent/waste" contain a sealing plug. The reason for this is that no ammonia flows through the sample volume, but the nitrogen gas is pushed into the loop. This is done at a pressure twice as high as the loop. This assumes that half of the sample volume ends up in the loop based on the ideal gas law. After the successful functional test, the SPIV was implemented in the experimental setup which is shown in Figure 3.9.

According to Figure 3.1, the SPIV is placed in front of the preheater and after the flowmeter. This is the "cold side" of the loop where the coolant is always liquid. Based on the solubility of nitrogen in ammonia from Section 2.6 and the loop volume estimation, it was concluded to use the sample volume of 0.02 mL.

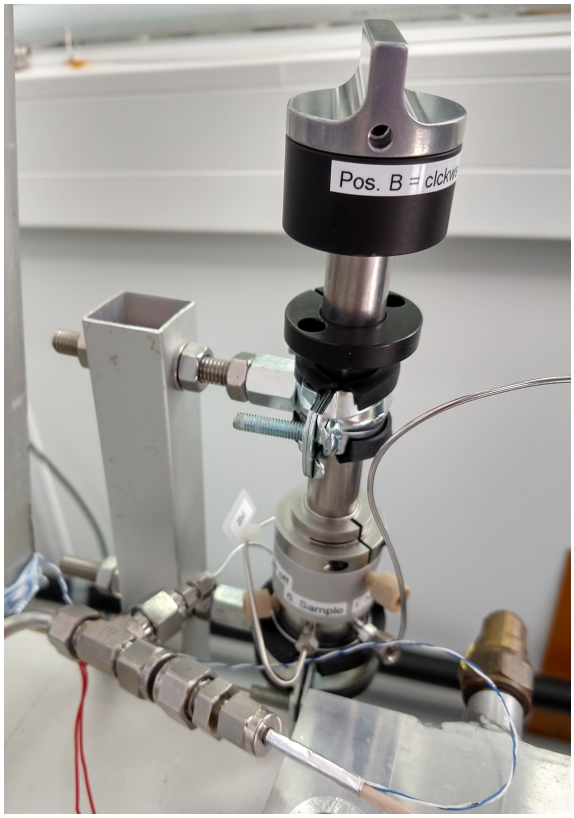

Figure 3.9: Implemented SPIV in the experimental setup.

3.4 Setup verification

As described in Section 2.3, empirical correlations for the two-phase heat transfer coefficient can be very inaccurate. However, correlations for single-phase liquid heat transfer are much more accurate. To validate the experimental setup, the heat transfer coefficient for liquid flow has been measured and compared with the analytical equation for laminar flow. For turbulent flow, the heat transfer coefficient is compared with the empirical Gnielinski correlation. After the setup verification, the reproducibility of the results was also examined. Since the current experimental setup has not been in operation for a year.

Let's first use the theory from Section 2.2.4 for the flow characterization. The pump in the current experimental setup can work with mass flows up to 1.2 g/s. As a result, it was decided to look at mass flows from 0.1 g/s. This value is used to calculate the Froude number from Equation 2.1 and the Reynolds number from Equation 2.4 to create Table 3.1.

Table 3.1: Typical two-phase refrigerants with different dimensionless numbers considered at a temperature of 60 °C and 1 mm internal tubing diameter.

	R134a	R1234yf	R245fa	R1233zd(E)	Ammonia	Methanol
Fr	14.7	12.9	50.5	62.0	62.8	1248.2
Eo	2.5	3.5	1.3	1.1	0.4	0.4
ξ	0.6	0.5	0.9	0.9	1.6	1.6
Re	1030	1312	496	623	1400	370

The other dimensionless numbers from Section 2.2.4 have also been used. For all typical

two-phase refrigerants, the conditions of $\xi > 0.5$ and Eo < 4 are met. Therefore, the minichannel assumption is valid. When a higher mass flow is used, the Froude number and Reynolds number also become larger. This does not affect the assumption of the minichannels. All refrigerants are laminar at the mass flow of 0.1 g/s since Re < 2300. It has already been decided to use ammonia as the refrigerant, the second last column is important.

To create an internal laminar flow in circular tubes, the Reynolds number must be below 2300 as shown in Equation 2.7. In the case of the current setup, the internal diameter is fixed at 1 mm. As a result, the Reynolds number only depends on the mass flow and the dynamic viscosity. Dynamic viscosity is a fluid property which is related to the saturation temperature. Figure 3.10 shows the saturation temperature versus the Reynolds number for different mass flow rates.

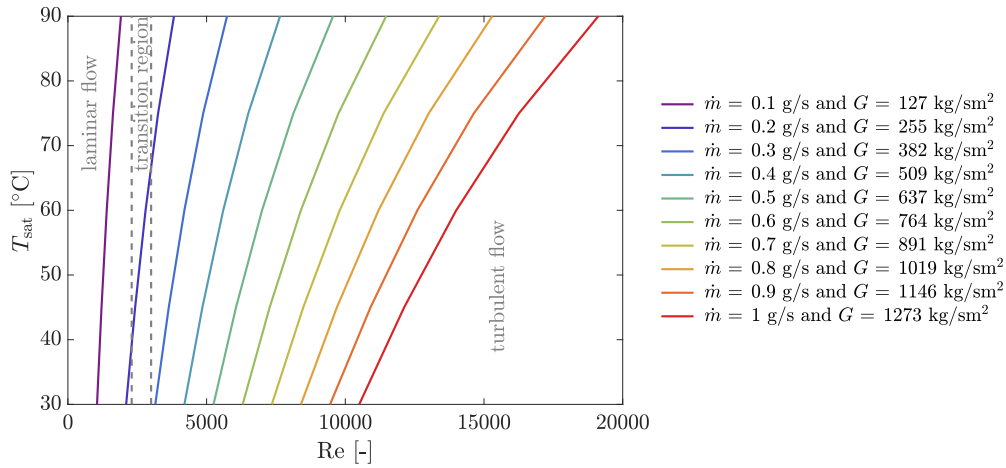

Figure 3.10: Saturation temperature versus the Reynolds number for different mass flow rates with their corresponding mass fluxes. The flow regimes are shown with the gray dashed lines.

Because the mass flux is important for the Wojtan flow pattern map, the corresponding values are next to the mass flow. This figure shows that there is only a fully laminar flow at a mass flow of 0.1 g/s. Since a turbulent flow occurs more often in a two-phase MPL thermal management system, mass flows of 0.2 to 0.4 g/s are also examined during the verification test.

3.4.1 Liquid heat transfer

In the verification test, the liquid temperatures are around 45 °C while the saturation temperature is set to 80 °C. Figure 3.11 show the mass flows during the measurement. According to Figure 3.10, the flow of 0.1 g/s is fully laminar, 0.2 g/s is in the transition region, and 0.3 and 0.4 g/s are fully turbulent. For each mass flow, the heater power is varied in steps. The heater power is related to the heat flux and is varied between just 1 W/cm^2 to 20 W/cm^2. Anticipating the test plan, these heat fluxes are 1, 2, 3, 4, 5, 7.5, 10, and 20 W/cm^2.

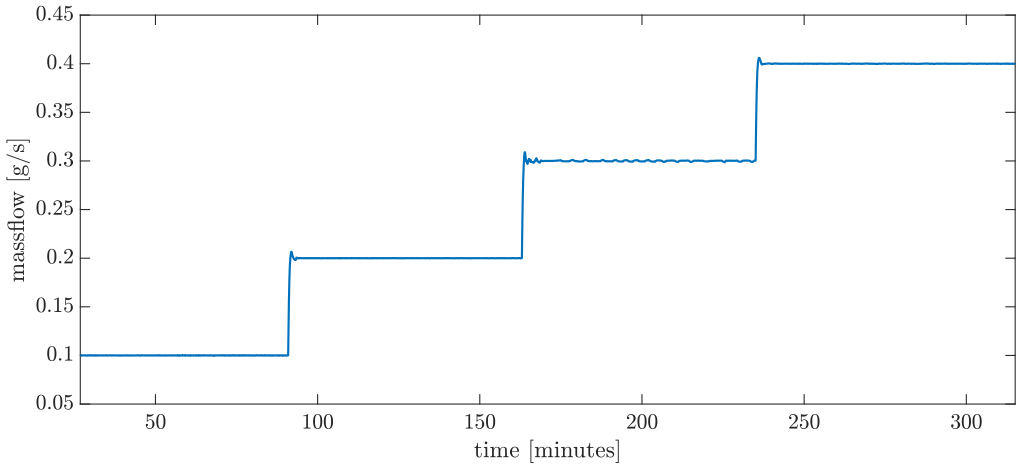

Figure 3.11: Mass flow during the verification test.

Figure 3.12 shows the measured liquid temperatures before and after the test tube and the temperature of the test tube wall. After 8 minutes at a certain heat flux, a steady-state is achieved after which the next heat flux is applied. From the measured temperatures and the applied heat fluxes, the heat transfer coefficient can be derived with Equation 3.5.

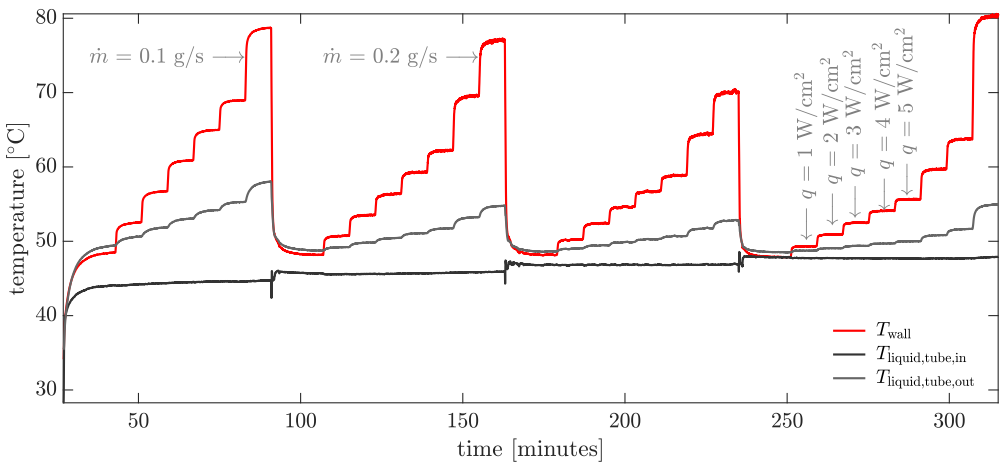

Figure 3.12: Measured temperatures as function of time during the verification test. The saturation temperature is set to 80 °C, the mass flows are 0.1, 0.2, 0.3, and 0.4 g/s, and the heat fluxes are 1, 2, 3, 4, 5, 7.5, 10, and 20 W/cm^2.

Figure 3.13 shows the measured heat transfer coefficient together with the empirical

heat transfer coefficient from Equation 2.6 (dashed lines). As mentioned, a flow of 0.1 g/s is fully laminar and therefore, the heat transfer coefficient can be determined analytically. Unfortunately, the heat transfer coefficient is overestimated, where the average deviation is 38%. The overestimation of the heat transfer coefficient also applies to the flow in the transition region, where the average deviation is 33%. For the turbulent flow measurements, the heat transfer coefficient is underestimated and here the average deviation is 17%.

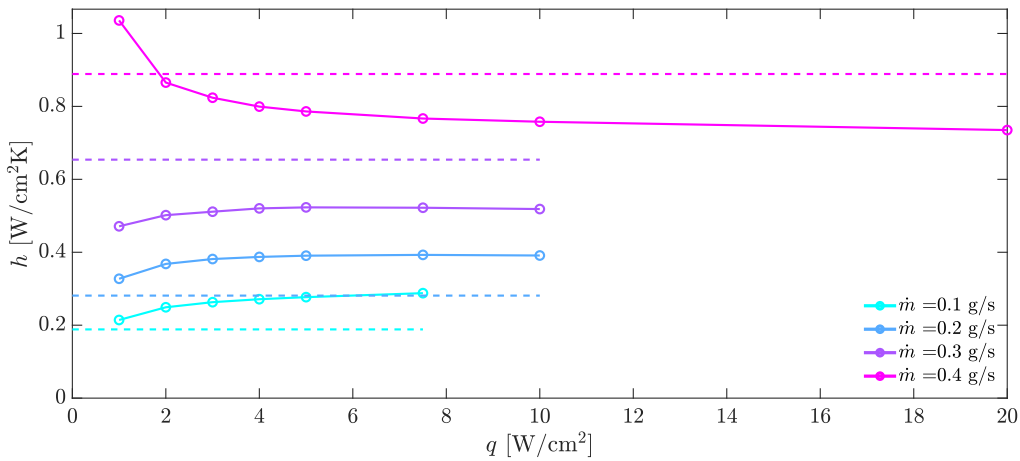

Figure 3.13: The open circles (o) are the measured heat transfer coefficient together with the calculated heat transfer coefficient (dashed lines).

However, the results in a previous project with the same setup showed better results. The crosses in Figure 3.14 show measurements from November 2019. These results show that there is a much better correspondence between the empirical and measured heat transfer coefficient with an average deviation of 7%.

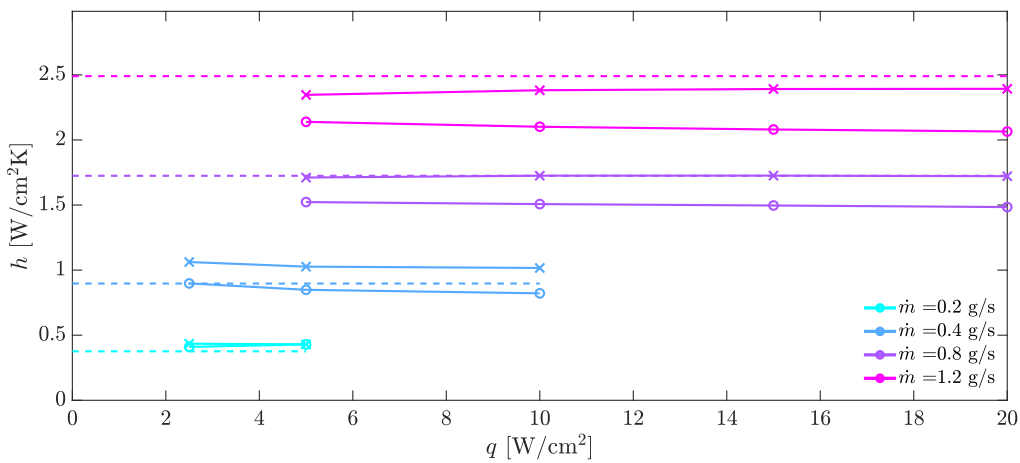

Figure 3.14: The crosses (x) are a heat transfer coefficient experiment from 2019 together with the calculated heat transfer coefficient (dashed lines). The open circles are a reproduction test done in 2021.

3.4.2 Reproducibility of the heat transfer coefficient

The above liquid heat transfer verification experiments were repeated after three days. The same procedure was used and the results are shown in Figure 3.15. The figure is similar to Figure 3.13 except that the triangles are a measurement from three days later. This shows that the deviation is greater with larger mass flows. In addition, the heat transfer coefficient has increased in all cases. The average deviation between the reproduction test is 5%. According to the data files, the same amount of power is supplied to the test section. However, the measured temperatures deviate a few degrees, which causes the deviation in the heat transfer coefficient.

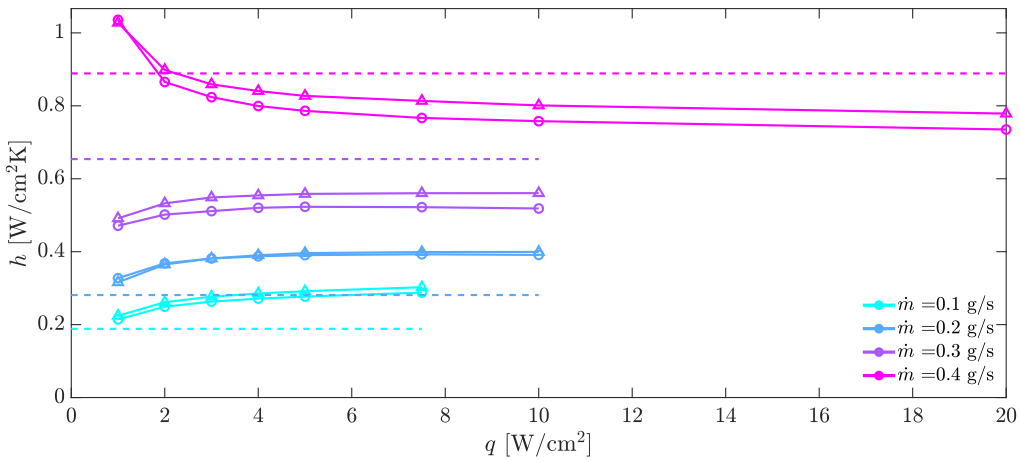

Figure 3.15: The open circles (o) are the measured heat transfer coefficient together with the calculated heat transfer coefficient (dashed lines). The triangles (△) are a reproduction test repeated after three days.

The solid lines with crosses in Figure 3.14 shows the reproduction between two years. At the low mass flow of 0.2 g/s, the average deviation is only 3%. Nevertheless, the higher mass flows show a higher deviation with an average of 15%.

When measurements were performed on the same day, the deviation between the measurements was minimal. The reason for this may be that the system will not be turned off. The deviations between the measured and empirical heat transfer coefficient indicate that it is not very accurate. However, this research aims to characterize subcooled and superheated liquid and to investigate the influence of dissolved gases. This is still possible with the current setup without being able to compare it very accurately with empirical correlations.

3.5 Demonstration of superheated liquid & fit parameter for superheated liquid modelling

Before a test plan can be written regarding superheated liquid, it must first be shown whether it occurs in the system. At the start of this study, the system was already in operation and the verification has been explained above. From Figure 2.21 in the theory section, a lower saturation temperature means a higher superheated liquid temperature. As a result, the first experiment is performed at a saturation temperature of 40 °C. The aim is to obtain a fit parameter for superheated liquid in the modelling section.

According to Equation 2.11, there are two unknowns, namely the bubble radius and the temperature gradient. In the experimental setup, an smooth extruded stainless steel tube with an inner diameter 1.00 mm is used. The outer diameter is 1.58 mm. The tolerance is 0.02 mm measured with CT scans which were made up to the tube ends, giving local erratic wall thickness results. Therefore, the bubble radius is setup specific. When a superheated liquid temperature is measured, a bubble radius can be obtained from Figure 2.21. This can be fitted to the other saturation temperatures. A constant mass flow and fixed geometry is used but a disadvantage of this method is that it does not include heat flux dependence. However, the aim is that the modified Young-Laplace equation will be a good indication for the superheated liquid temperature.

Superheated liquid is expected to occur at relatively low heat fluxes. First, two low heat fluxes of 1 and 2 W/cm^2 are used. A reference experiment with pure ammonia is done to see if superheated liquid occurs which is shown in Figure 3.16.

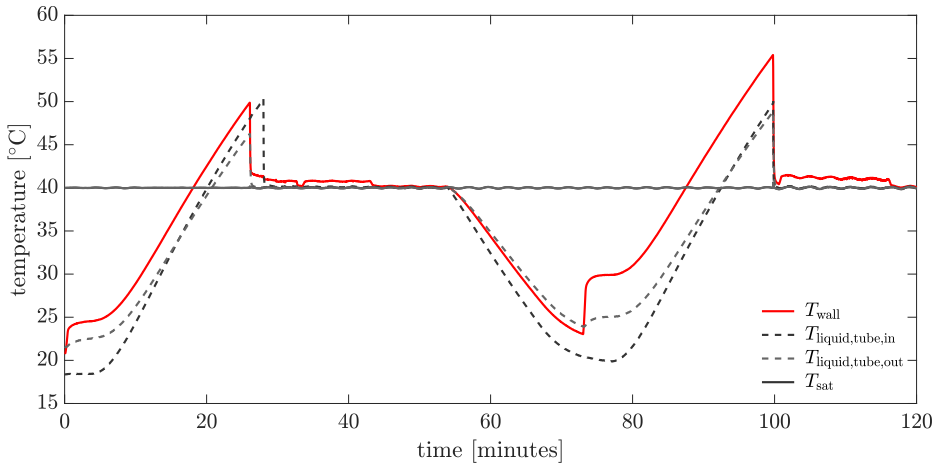

Figure 3.16: Occurrence of superheated liquid in the experimental setup. Measured with a saturation temperature of 40 °C, a mass flow of 0.1 g/s, and the heat fluxes are 1, and 2 W/cm^2.

It shows that it is indeed possible to show superheated liquid with ammonia in the experimental setup. The black and gray dashed lines exceed the saturation temperature of 40 °C. For the first peak, the maximum $T_{\text{liquid,tube,in}}$ is 50.3 °C and $T_{\text{liquid,tube,out}}$ is 46.3 °C. Using Equation 3.6, $T_{\text{fluid}} = 48.3$ °C. The second peak with a heat flux of 2 W/cm^2 has a maximum $T_{\text{liquid,tube,in}}$ of 49.8 °C and $T_{\text{liquid,tube,out}}$ is 48.8 °C. Again, using Equation 3.6, $T_{\text{fluid}} = 49.3$ °C. This results in an average fluid temperature of 48.8 °C. According to Equation 2.11, the superheated liquid temperature is 8.8 °C. Figure 2.21 is plotted again where the gray dashed lines are an indication for the superheated liquid temperature with a 10% margin.

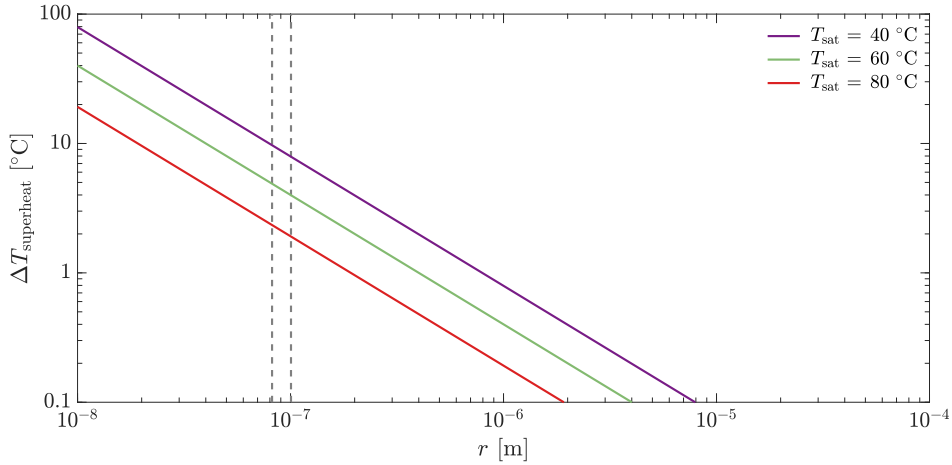

Figure 3.17: Superheated liquid prediction for different bubble radii with ammonia as refrigerant and different saturation temperatures. The gray dashed lines used a 10% margin as a fit parameter to use in the modelling section.

It corresponds to a bubble radius of $8.2 \cdot 10^{-8}$ till $10.0 \cdot 10^{-8}$ m. This results in the superheated liquid temperatures of 8.8, 4.4, and 2.1 °C being used in the modelling section for the saturation temperatures of 40, 60, and 80 °C, respectively.

3.6 Methods & test plan

The previous section demonstrates the occurrence of superheated liquid in the experimental setup. This section describes a test plan to measure subcooled and superheated liquid as reference experiments. In addition, the tests with the injections of nitrogen are also described. The results from the superheated liquid reference experiments can be used to compare the experiments with injected nitrogen in ammonia.

Resulting from the previous section, it has been found that the reproduction of the low used mass flows gives a smaller average deviation than for the higher mass flows. As a result, it was decided not to vary the mass flows and to keep them constant at 0.1 g/s. Section 2.2.3 describes that the flow boiling heat transfer is strongly dependent on the heat flux when nucleate boiling dominates, which is the case at low vapor mass fractions in these experiments. Moreover, many papers confirm that a relatively low mass flow has a smaller influence on the flow boiling heat transfer [67] [54].

A mass flow of 0.1 g/s combined with a 1 mm internal diameter tube gives a mass flux of 127 kg/sm^2. This is plotted in the Wojtan flow pattern map from the theory section with the other mass flows used in the setup verification.

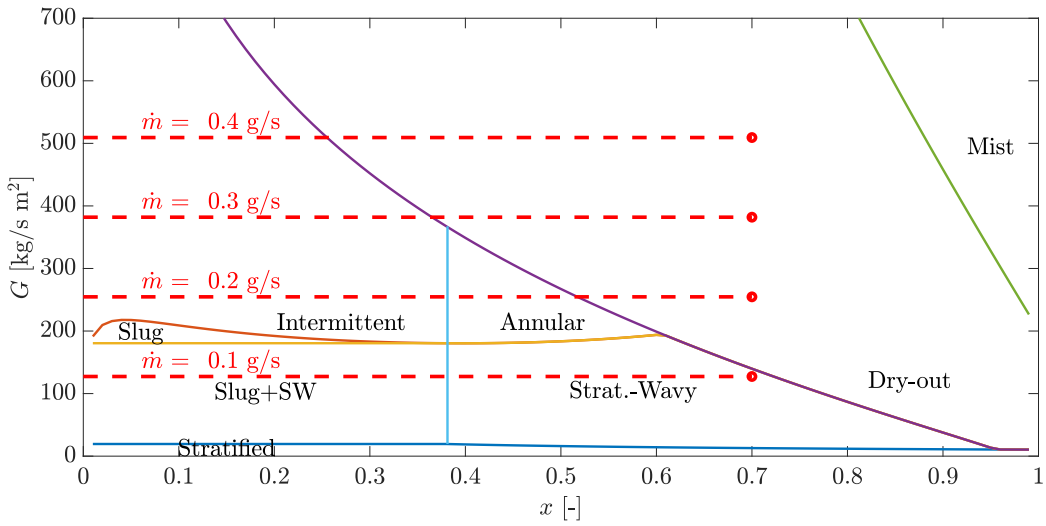

Figure 3.18: Wojtan flow pattern map for ammonia at 60 °C for horizontal tubes with 1 mm internal diameter. The red lines represent the mass flux in the evaporator for different mass flows according to the setup verification [42].

The above figure suggests that dry-out occurs earlier at a high mass flux. As already explained in the theory section, experimental experience shows that the prediction of dry-out occurs is known to be very unreliable. In addition, for subcooled and superheated liquid the experiments do not have to go to high vapor mass fractions. The experiments are more about the phase transition from liquid to a mixture around a vapor mass fraction of $x = 0$.

After some manual tests, it was decided that the heat flux applied to the system ranges from 1 to 20 W/cm^2. The low heat fluxes for the superheated liquid reference experiments and the higher heat fluxes for subcooled liquid. The set delay after the thermostated plates is because the connected condenser bath has a higher thermal mass. For instance, the heat flux applied to the test section needs less delay due to the lower thermal mass and because the environment is already at saturation temperature. The test sequence for the subcooled liquid reference experiment is as follows:

1. No injection of nitrogen: 0 mL;
2. $\dot{m} = 0.1$ g/s;
3. $T_{\text{first,thermostated,plate}} = 1$ °C;
   $T_{\text{sat}} = 40$ °C;
   $T_{\text{second,thermostated,plate}} = 40$ °C;
   Delay 1800 s;
4. $q = 5$ W/cm^2;
   Delay 180 s;
5. $T_{\text{first,thermostated,plate}} = 90$ °C;
   Delay 2400 s;
6. Repeat step 3 till 5 for $q = [7.5\ 10\ 20]$ W/cm^2;
7. Repeat step 3 till 6 for $T_{\text{sat}} = [60\ 80]$ °C;
8. $q = 0$ W/cm^2;
   $\dot{m} = 0.0$ g/s;
   Delay 120 s.

The test sequence for the superheated liquid reference experiments is the same except for the heat fluxes. The range for the heat flux is $q = [1\ 2\ 3\ 4\ 5]$ W/cm^2. These reference measurements can serve as a comparison for the experiments with the addition of nitrogen. First, it must be demonstrated that adding nitrogen gas in liquid ammonia has any effect on the start of the boiling process. The saturation temperature of 40 °C was analysed initially, since the highest superheated liquid temperature was observed here. As a result, the nitrogen is injected at a pressure of 31.1 bar. To measure any influence, a relatively large amount of nitrogen gas is added. The same method for the measurements of superheated liquid reference experiment can be used. Nitrogen can then be added beforehand with the SPIV with a delay of 240 seconds. When nitrogen is fully saturated in the liquid ammonia is showed in Figure 2.25. The solubility decreases as the saturation temperature is approached, causing the gas to be released from the ammonia. If any effect of the dissolved gas has been observed manually, all measurements can be repeated with different amounts of nitrogen. The test sequence for the dissolved nitrogen in liquid ammonia experiment is as follows:

1. Injection of nitrogen: 0.01 mL;
   Delay 240 s;
2. $\dot{m} = 0.1$ g/s;
3. $T_{\text{first,thermostated,plate}} = 1$ °C;
   $T_{\text{sat}} = 40$ °C;
   $T_{\text{second,thermostated,plate}} = 40$ °C;
   Delay 1800 s;
4. $q = 1$ W/cm^2;
   Delay 180 s;
5. $T_{\text{first,thermostated,plate}} = 90$ °C;
   Delay 2400 s;
6. Repeat step 3 till 5 for $q = [2\ 3\ 4\ 5]$ W/cm^2;
7. Repeat step 3 till 6 for $T_{\text{sat}} = [60\ 80]$ °C;

8. Repeat step 1 till 6 for injection of nitrogen = [0.02 0.03 0.04] mL;
9. $q = 0$ W/cm^2;
   $\dot{m} = 0.0$ g/s;
   Delay 120 s.

The amount of nitrogen injected depends on the influence at the first manual experiments. The experimental setup does not have complete accuracy. The uncertainties in the measured parameters are listed below:

- Thermocouple temperature sensors ±0.1 °C;
- Pressure sensors ±0.1 bar;
- Mass flow ±0.001 g/s;
- Applied heat flux to the test section. This error is based on several components as the electrical conductance, the applied power, the wall thickness, and the length of the tube. Combing these components gives an error margin of 3%.

4

Modelling

This chapter discusses the modelling of heat transfer correlations for different conditions and the radial flow analysis as theoretically described in Chapter 2. The goal is to be able to better predict the two-phase behavior in two-phase thermal management systems using modelling.

4.1 Boiling heat transfer correlations

The different empirical correlations have already been mentioned in Section 2.3.1. This study looks at the Kandlikar, Kim & Mudawar, and the Gungor & Winterton correlations. In Figure 2.14, these correlations are already shown for a heat flux of 1 and 10 W/cm^2. In comparison, Kandlikar estimates the heat transfer coefficient lower than the other two correlations, and Kim & Mudawar estimates the highest. The influences of the different parameters do not differ per empirical correlation and therefore Kandlikar is used for the modelling below. In addition, Kandlikar is one of the best applicable correlations for ammonia as a refrigerant [51]. This section discusses the parameters from the test plan and the influence of the heat flux, saturation temperature, and mass flow on the heat transfer coefficient. This is necessary in order to be able to better link the results later to the subcooled and superheated liquid experiments.

4.1.1 Influence of the heat flux on the heat transfer coefficient

The Kandlikar correlation for various heat fluxes from the test plan are plotted in the figure below. A higher heat flux results in a higher boiling heat transfer coefficient. Unfortunately, the difference between the single-phase and the two-phase heat transfer coefficient is relatively small for low heat fluxes. For the lowest heat flux of 1 W/cm^2, the heat transfer coefficient increases from 0.17 to 0.30 W/cm^{2}K. For the heat flux of 20 W/cm^2, this is more than 10 times higher.

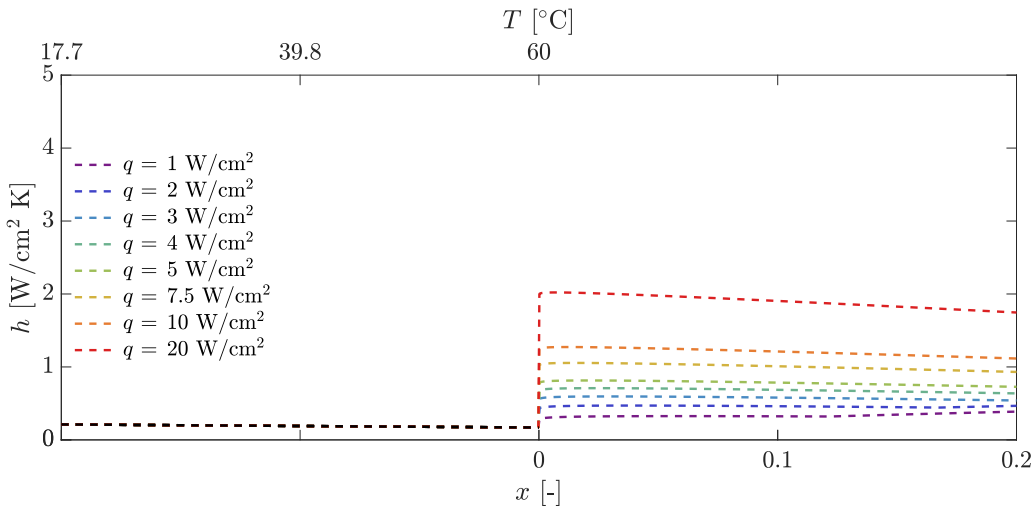

Figure 4.1: Heat transfer coefficient plot for the Kandlikar correlation with ammonia as refrigerant. A saturation temperature of 60 °C, a 1 mm internal diameter, a mass flow of 0.1 g/s, and various heat fluxes are used.

The same figure with the whole range for the vapor mass fraction is shown in Appendix E. The influence of the heat flux becomes less as the vapor mass fraction increases. Furthermore, the Gungor & Winterton and Kim & Mudawar correlations are also shown in the appendix.

4.1.2 Influence of the saturation temperature on the heat transfer coefficient

As described in the theory section, the influence of the saturation temperature will affect the subcooled and superheated liquid. This section investigates the influence of the saturation temperature on the empirical correlations. Figure 4.1 is plotted again for the saturation temperatures of 40 and 80 °C in Figure 4.2 and 4.3, respectively.

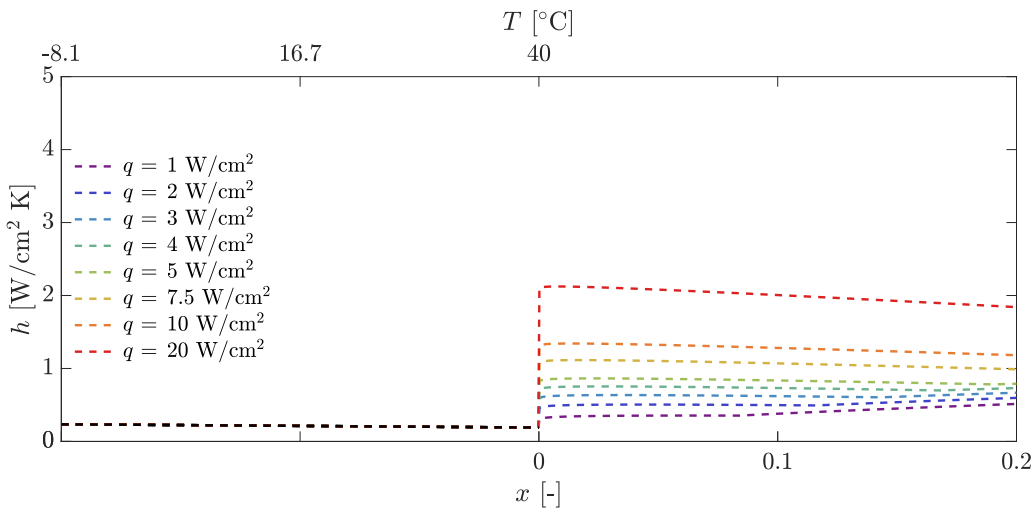

Figure 4.2: Heat transfer coefficient plot for the Kandlikar correlation with ammonia as refrigerant. A saturation temperature of 40 °C, a 1 mm internal diameter, a mass flow of 0.1 g/s, and various heat fluxes are used.

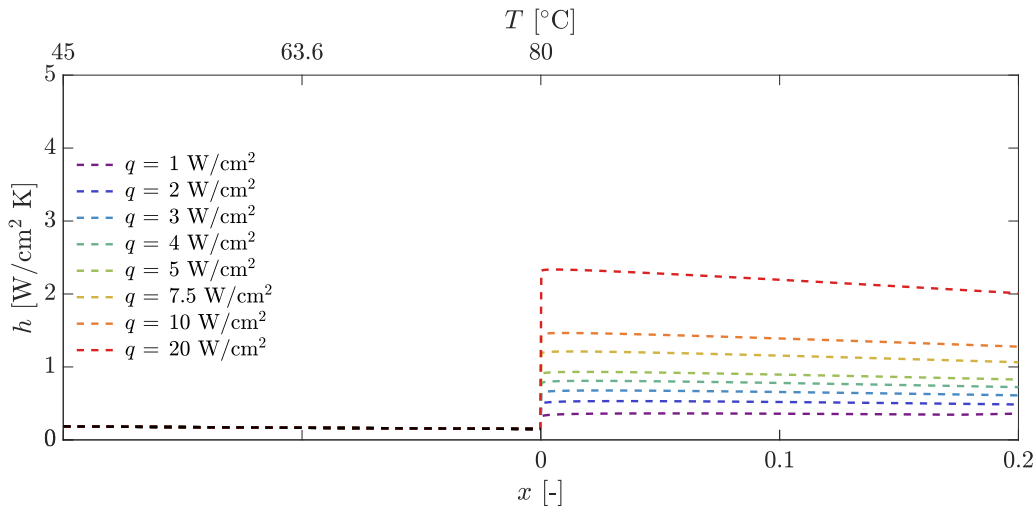

Figure 4.3: Heat transfer coefficient plot for the Kandlikar correlation with ammonia as refrigerant. A saturation temperature of 80 °C, a 1 mm internal diameter, a mass flow of 0.1 g/s, and various heat fluxes are used.

The differences between the heat transfer coefficient for the various saturation temperatures is minimal. At a higher saturation temperature, the single-phase heat transfer coefficient decreases from 0.19 to 0.17 to 0.15 W/cm^{2}K, respectively for a saturation temperature of 40, 60, and 80 °C. With two-phase heat transfer, the difference is also visible, but again minimal. The saturation temperature has more influence on the location of the phase change. So with subcooled liquid the vertical line will move to the left and with superheated liquid to the right. At a lower saturation temperature, a higher superheated liquid temperature is expected and so the vertical line will be further to the right.

Although only a mass flow of 0.1 g/s is considered in the experiments, it is also interesting to examine the influence of the mass flow on the heat transfer coefficient. Therefore it is briefly explained in Appendix E. The influence of the mass flow on the heat transfer coefficient is shown in Figure E.4.

4.2 Radial temperature distribution

As discussed in Section 2.5.2, the convection-diffusion equation with the Hagen-Poiseuille flow can be used to make a prediction of the radial temperature distribution in the channel. The PDE has been solved numerically with the MATLAB PDE solver. The internal diameter is 1.0 mm for all calculations as indicated in the experimental setup section. In the model, different heat fluxes, mass flows, and inlet temperatures can be used to look at the different influences. First, subcooled liquid will be treated where the inlet temperature (T_{in}) of the evaporator is lower than the saturation temperature. Next, the fit parameter from Section 3.5 is used to make an estimation for the radial temperature distribution and the location of occurrence for superheated liquid in the heated tube.

4.2.1 Subcooled liquid modelling

According to what is achievable with the experimental setup and the environment in the NLR lab, the inlet temperatures of 17, 27, and 47 °C are used for the saturation

temperatures of 40, 60, and 80 °C, respectively. The inlet temperatures depend on various factors and parameters, such as the heat leak, condenser bath, and the mass flow. An ammonia mass flow of 0.1 g/s is used and the heat flux on the wall varies as described in the test plan. Not all specific cases are shown, only important observations are mentioned.

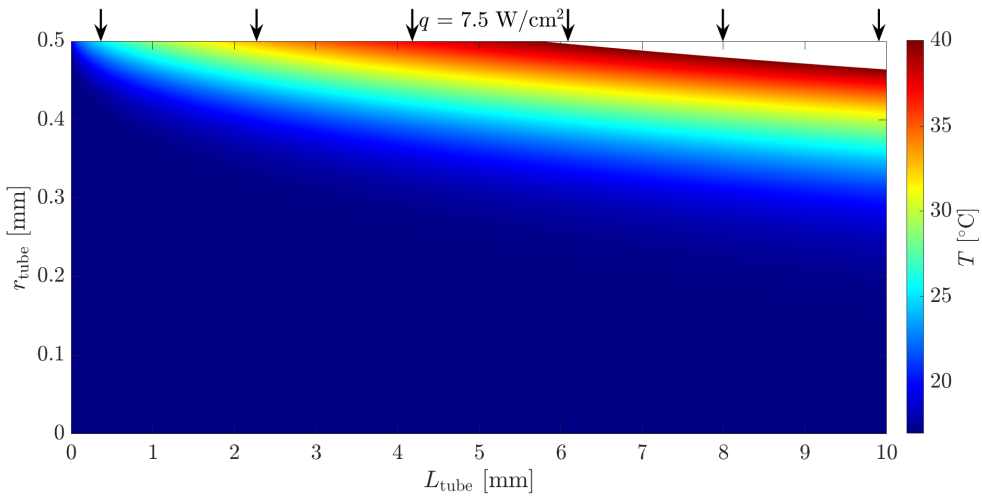

Figure 4.4: Calculated liquid temperature for laminar Hagen-Poiseuille flow in a contour plot for subcooled liquid at $T_{\text{sat}} = 40$ °C, $T_{\text{in}} = 17$ °C, and $q = 7.5$ W/cm^2.

In the two-dimensional temperature field above, the lower axis represents the axi-symmetric center of the tube. The top axis is the tube wall where the heat flux is applied. The flow is from left to right and L_{tube} is the length of the heated tube. When the saturation temperature is reached for subcooled liquid, it is assumed that there is two-phase behavior on the heated wall. Figure 4.4 is not a good example for subcooled liquid because the saturation temperature is only reached after 5.7 mm due to the relatively low heat flux. Figure 4.5 shows a plot with the same conditions but with a heat flux of 20 W/cm^2.

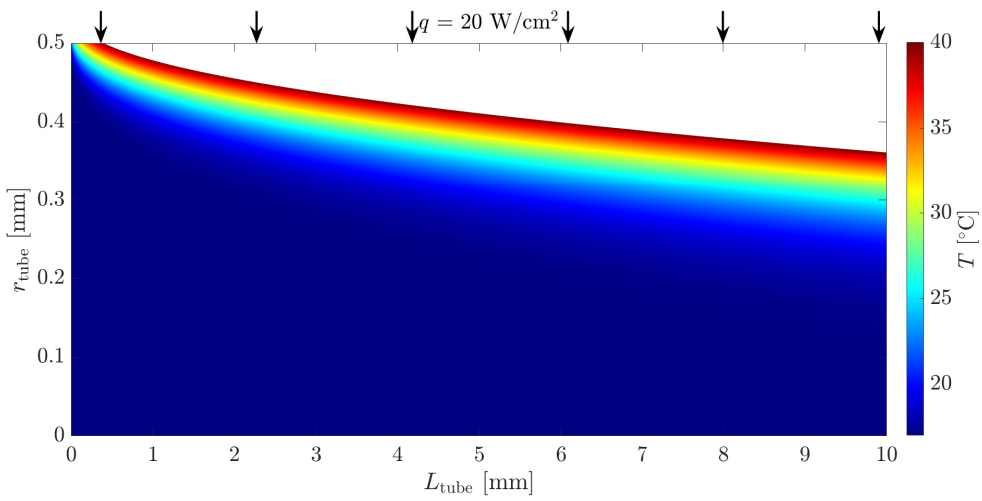

Figure 4.5: Calculated liquid temperature for laminar Hagen-Poiseuille flow in a contour plot for subcooled liquid at $T_{\text{sat}} = 40$ °C, $T_{\text{in}} = 17$ °C, and $q = 20$ W/cm^2.

It can be observed that two-phase behavior on the wall occurs much earlier, namely

after 0.4 mm of the length of the tube. With this low inlet temperature and the short heated tube of 10 mm, the bulk liquid does not yet reach the saturation temperature. In practical two-phase MPL thermal management systems, it is inefficient to let the preheater heat the liquid all the way to the saturation temperature. Often, the system is designed with an inlet temperature that is 5 or 10 °C below the saturation temperature. Hence, Figure 4.6 has a somewhat higher inlet temperature of 30 °C to illustrate this effect.

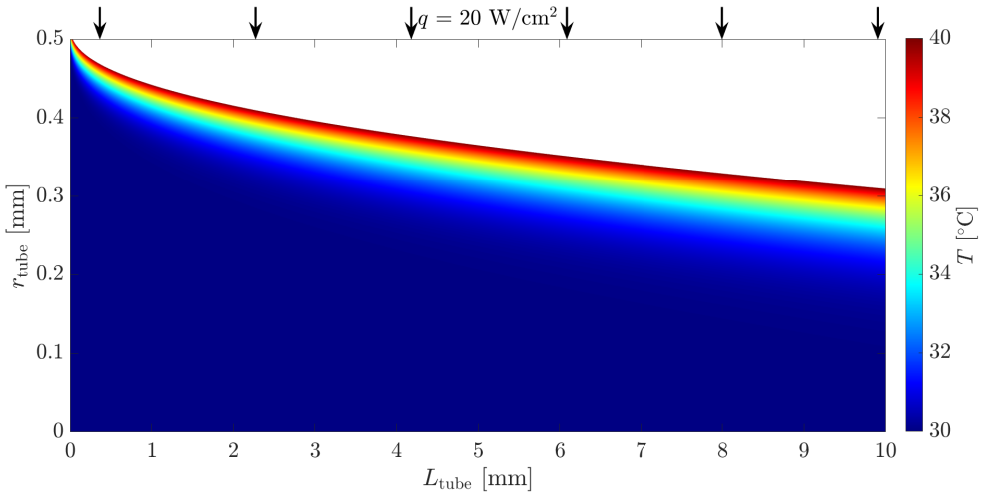

Figure 4.6: Calculated liquid temperature for laminar Hagen-Poiseuille flow in a contour plot for subcooled liquid at T_{sat} = 40 °C, T_{in} = 30 °C, and q = 20 W/cm^2.

The temperature on the wall already reaches the saturation temperature after 0.04 mm. This means that the tube wall has immediately reached the uniform temperature. To not plot all the different heat flux plots, the saturation temperature line for the different heat fluxes is plotted in one figure. This is shown in Figure 4.7 for the same inlet temperature of 17 °C and a saturation temperature of 40 °C.

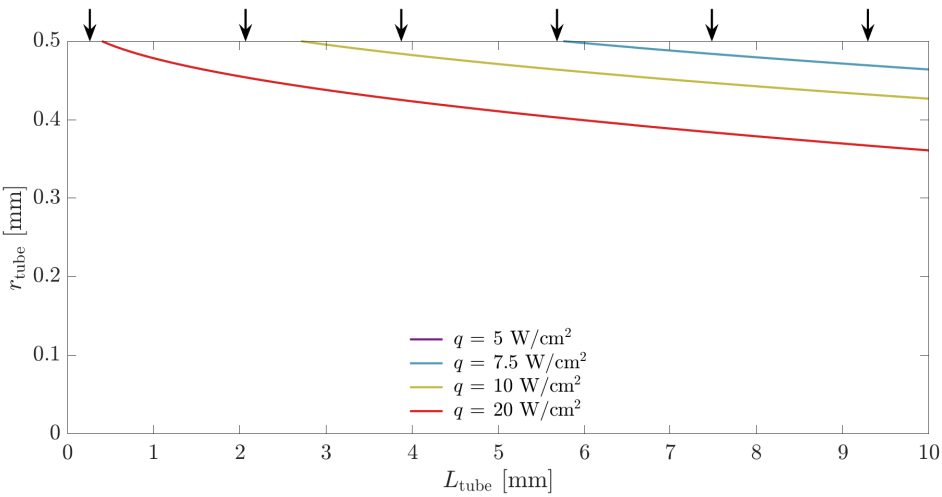

Figure 4.7: Calculated saturation temperature lines for laminar Hagen-Poiseuille flow at T_{sat} = 40 °C, T_{in} = 17 °C, and various heat fluxes applied to the wall.

The effect of the applied heat flux on the wall is visible here. At a heat flux of 20 W/cm^2, the wall reaches saturation temperature much earlier. The saturation temperature at

the wall is not reached at a heat flux of 5 W/cm^2.

Table 4.1: The location on the heated tube where the temperature reaches the saturation temperature for the different parameters from the test plan.

	T_{sat} = 40 °C	T_{sat} = 60 °C	T_{sat} = 80 °C
q [W/cm^2]		L_{sat} [mm]	
5	>10	>10	>10
7.5	5.8	>10	>10
10	2.7	6.6	5.9
20	0.4	1.0	0.9

L_{sat} is the location on the heated tube where the temperature reaches the saturation temperature. It is assumed that two-phase behavior on the wall occurs from this point. The ">10" values mean that the saturation temperature is not reached on the heated wall due to the short tube length. At a relatively high heat flux of 20 W/cm^2, subcooling occurs sooner than at the lower heat fluxes.

4.2.2 Superheated liquid modelling

The fit parameter from Section 3.5 is used to make an estimation for the radial temperature distribution and the location of occurrence for superheated liquid in the heated tube. The average nucleation radius is $9.1 \cdot 10^{-8}$ m determined in Section 3.5 and shown in Figure 3.17. This results in superheated liquid temperatures of 8.8, 4.4, and 2.1 °C for the saturation temperatures of 40, 60, and 80 °C, respectively.

Again, a two-dimensional temperature field has been created where the liquid temperature can now rise to the superheated liquid temperature. After the superheated liquid temperature is reached it will jump to the saturation temperature. In practice, several NLR projects often tell us that the superheated liquid temperature is not reproducible and that vibration can also trigger the liquid to start boiling. Figure 4.8 shows the modelling with a low heat flux of 1 W/cm^2.

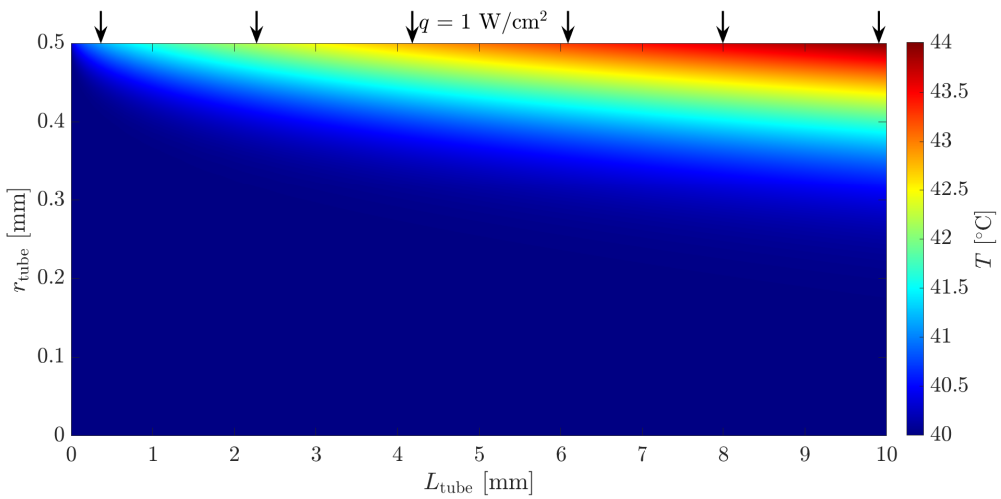

Figure 4.8: Calculated liquid temperature for laminar Hagen-Poiseuille flow in a contour plot for superheated liquid at $T_{sat} = T_{in} = 40$ °C, $T_{superheat} = 48.8$ °C, and $q = 1$ W/cm^2.

This shows that the maximum superheated liquid temperature is not achieved. In the experimental setup, the thermocouple is located at 5.60 mm from the beginning of

the tube. This means that a liquid temperature of 43.2 °C may be measured in the experiment. The figure below shows the comparison of 3 W/cm^2. According to the figure, the maximum superheated liquid temperature could not be measured because it is in front of the thermocouple location. However, it depends on when the trigger for boiling occurs, before or after the location of the thermocouple.

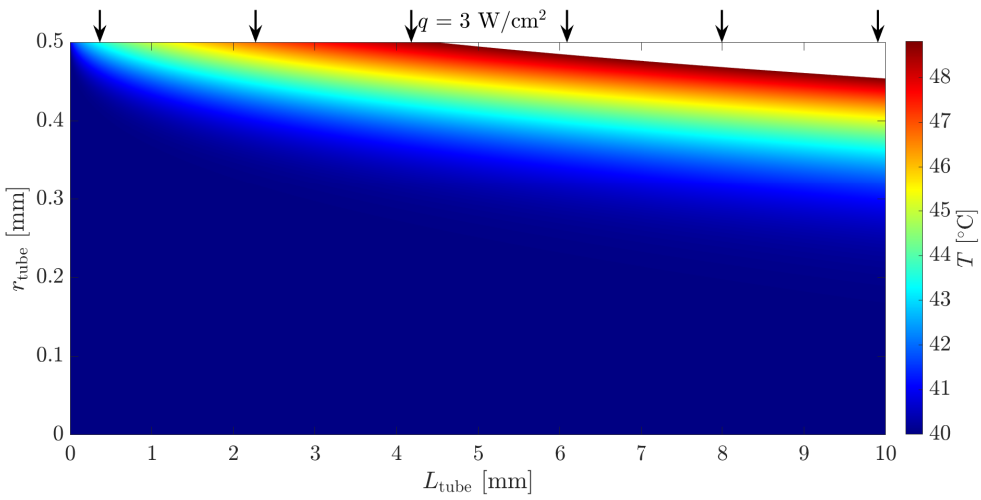

Figure 4.9: Calculated liquid temperature for laminar Hagen-Poiseuille flow in a contour plot for superheated liquid at $T_{\text{sat}} = T_{\text{in}} = 40$ °C, $T_{\text{superheat}} = 48.8$ °C, and $q = 3$ W/cm^2.

Figure 4.10 has been made to show various heat fluxes in one plot for a superheated liquid temperature of 48.8 °C. These lines are the front up to where superheat occurs, above these lines, there is two-phase behavior. At the higher heat flux of 5 W/cm^2, superheated liquid still occurs, but this should be quickly triggered by the applied heat flux to start boiling.

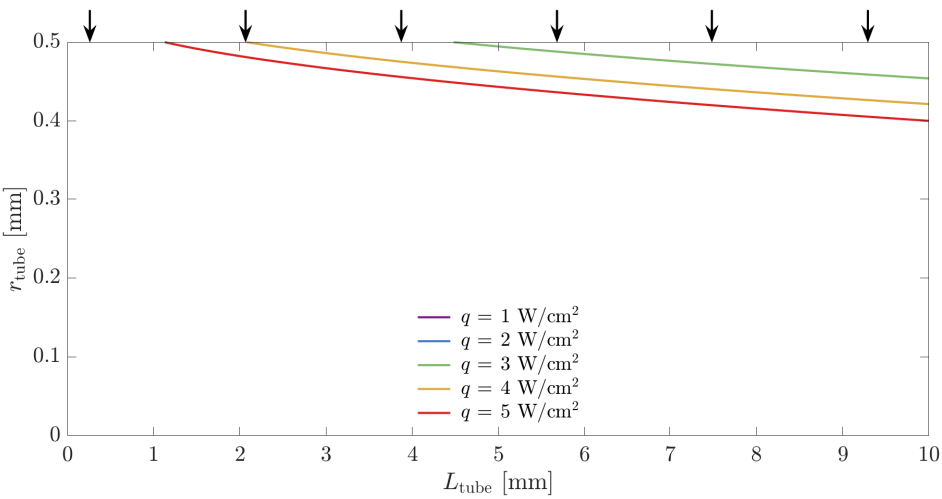

Figure 4.10: Calculated superheated liquid temperature lines for laminar Hagen-Poiseuille flow at $T_{\text{sat}} = T_{\text{in}} = 40$ °C, $T_{\text{superheat}} = 48.8$ °C, and various heat fluxes applied to the wall.

The same plot is shown below for a higher saturation temperature of 80 °C. This higher saturation temperature has a lower superheated liquid temperature and thus results in a less overheated wall. For the heat fluxes of 2 to 5 W/cm^2, the superheated liquid

temperature should be reached almost immediately upon entering the heated tube.

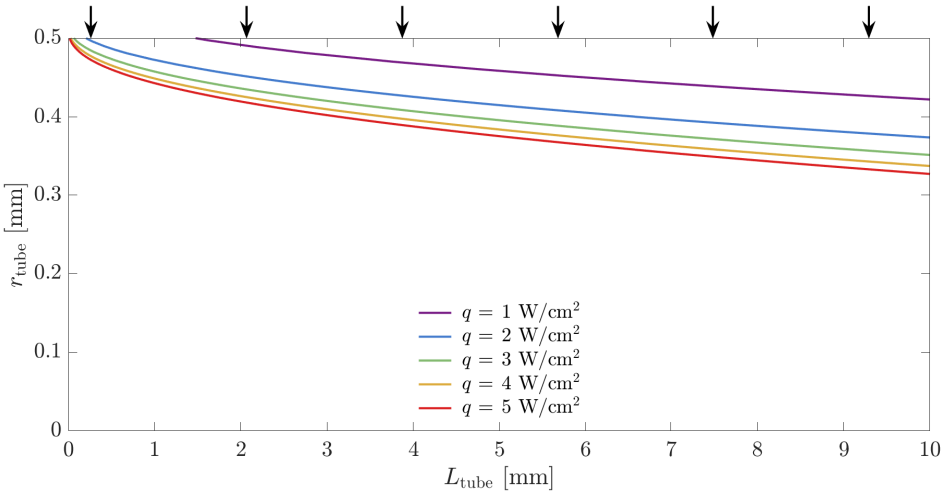

Figure 4.11: Calculated superheated liquid temperature lines for laminar Hagen-Poiseuille flow at $T_{\text{sat}} = T_{\text{in}} = 80$ °C, $T_{\text{superheat}} = 82.1$ °C, and various heat fluxes applied to the wall.

As for subcooled liquid, all lengths are summarized in a table. The difference is that it is not the location of the saturation temperature that matters, but the location of the superheated liquid temperature L_{sup}.

Table 4.2: The location on the heated tube where the temperature reaches the superheated liquid temperature for the different parameters from the test plan.

	$T_{\text{sat}} = 40$ °C	$T_{\text{sat}} = 60$ °C	$T_{\text{sat}} = 80$ °C
q [W/cm^2]		L_{sup} [mm]	
1	>10	>10	1.5
2	>10	1.8	0.2
3	4.5	0.6	0.06
4	2.1	0.3	0.03
5	1.1	0.1	0.02

L_{sup} is the location on the heated tube where the temperature reaches the superheated liquid temperature. It is assumed that two-phase behavior on the wall occurs from this point. The ">10" values mean that the whole heated wall is superheated and that there is occurrence of two-phase behavior on the wall. At a higher saturation temperature, the length of the tube that experiences wall superheat is lower. In addition, L_{sup} decreases as the heat flux increases.

The goal with this model is to be able to predict the behavior of subcooled and superheated liquid in a two-phase MPL thermal management system. In the experimental setup, the thermocouple is located at 5.6 mm from the beginning of the tube. The temperature is measured at this point on the test tube. So if $L_{\text{sat}} <$ 5.6 mm or $L_{\text{sup}} <$ 5.6 mm, then two-phase behavior is measured on the heated wall. This means that according to the contour plots above, two-phase behavior is often experimentally measured since the superheated liquid temperature is already reached before the thermocouple. The above results can be compared with the experiments described in the next chapter.

5

Results

This chapter uses the experimental setup described in Chapter 3 to arrive at the results which are compared with the modelling from previous chapter. First, the subcooled liquid experiments are discussed. Next, the superheated liquid experiments are treated, after which nitrogen is dissolved in ammonia to look if the onset of boiling can be enhanced.

5.1 Subcooled liquid experiments

According to the test plan described in Section 3.6, the subcooled reference experiments are performed with heat fluxes of 5, 7.5 10, and 20 W/cm^2. The tube and fluid temperatures over time for the different heat fluxes at a saturation temperature of 40 °C are shown in Figure 5.1.

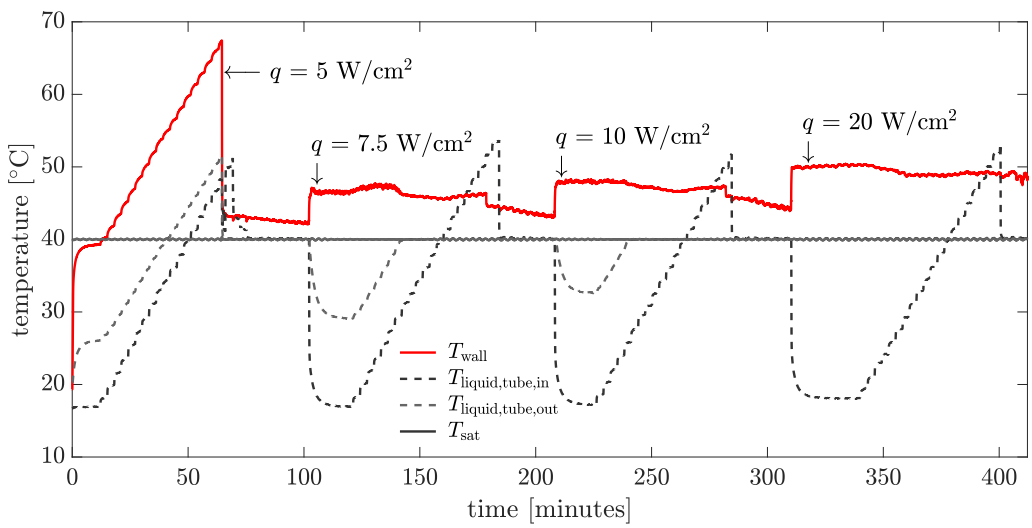

Figure 5.1: Temperature over time for the applied heat fluxes of 5, 7.5, 10, and 20 W/cm^2 with a saturation temperature of 40 °C.

The heat fluxes of 5, 7.5 10, and 20 W/cm^2 are applied after approximately 10, 120, 230, and 340 minutes, respectively. The heat flux of 5 W/cm^2 is also used in the superheated liquid experiments. Logically, superheated liquid is also visible here with a

superheated liquid temperature of 11.0 °C. At higher heat fluxes, the wall immediately shows two-phase behaviour due to the relatively constant wall temperature. In addition, the liquid temperatures are below the saturation temperature. $T_{\text{liquid,tube,in}}$ shows superheated liquid for all cases. However, the question then is whether superheated liquid occurs at the location of T_{fluid} in the test section according to Figure 3.6. At a heat flux of 7.5 W/cm^2, the subcooled liquid temperature is 17 °C below the saturation temperature, assuming that T_{fluid} is the average of the $T_{\text{liquid,tube,in}}$ and $T_{\text{liquid,tube,out}}$. The figure below shows the same experiment, except that the saturation temperature here is 60 °C.

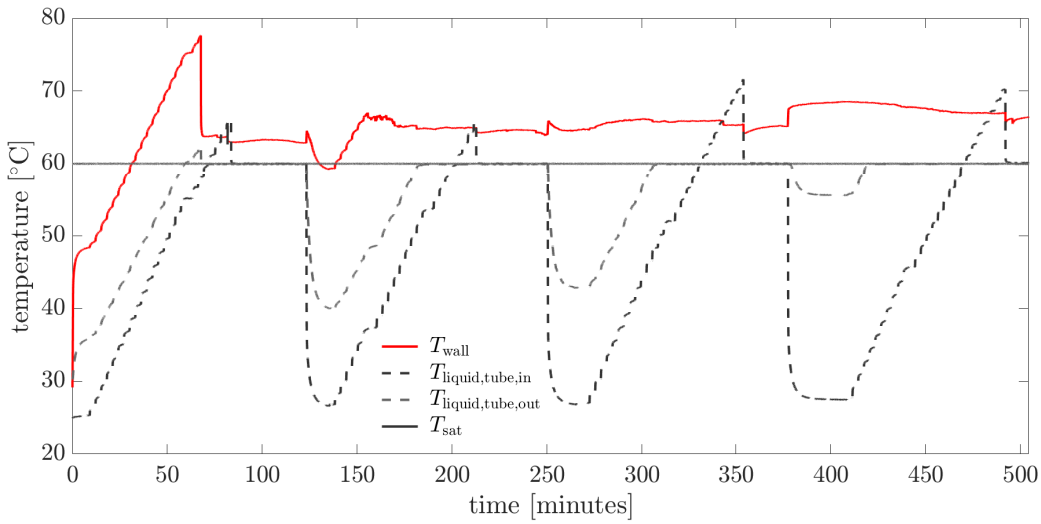

Figure 5.2: Temperature over time for the applied heat fluxes of 5, 7.5, 10, and 20 W/cm^2 with a saturation temperature of 60 °C.

A similar pattern is visible at a saturation temperature of 40 °C. However, the wall superheat and the superheated liquid temperature decrease at a higher saturation temperature. The wall superheat drops from 27.4 to 17.6 °C and the superheated liquid temperature from 11.0 to 3.7 °C for 5 W/cm^2.

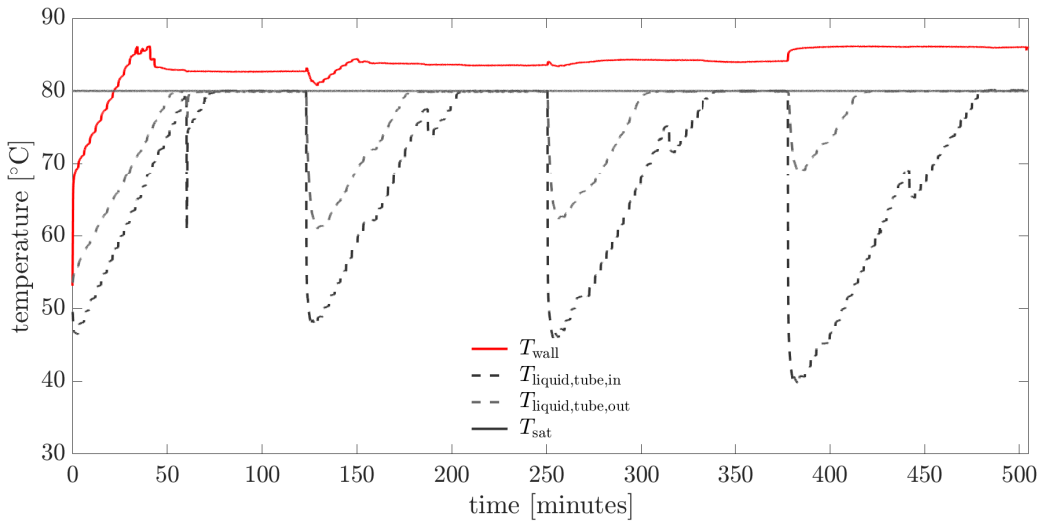

Figure 5.3: Temperature over time for the applied heat fluxes of 5, 7.5, 10, and 20 W/cm^2 with a saturation temperature of 80 °C.

Figure 5.3 shows the superheated liquid reference experiment with a saturation temperature of 80 °C. No superheated liquid is measured at all heat fluxes. At the high heat flux of 20 W/cm^2, subcooling is smoothly visible. The wall temperature is constant and therefore shows immediate two-phase behavior at the tube inlet. $T_{\text{liquid,tube,in}}$ is 39.8 °C and $T_{\text{liquid,tube,out}}$ is 69.1 °C. This results in a T_{fluid} of 54.5 °C. While processing the results, it was decided to not plot T_{fluid} in the figures above. For instance, the measurement with a saturation temperature of 60 °C and a heat flux of 10 W/cm^2 would then result in unrealistic modelling. In addition, the T_{fluid} at the superheating tipping point is in some cases difficult to model which is discussed in the next section.

5.2 Superheated liquid experiments

As described in Section 3.5, superheated liquid can be measured with the existing setup. Previous experiments were performed for verification only. During these experiments, an automatic script was used that automatically sets the saturation temperatures of 40, 60, and 80 °C for the different heat fluxes of 1, 2, 3, 4, and 5 W/cm^2. The wall and fluid temperatures over time for the different saturation temperatures for 1 W/cm^2 are shown in Figure 5.4.

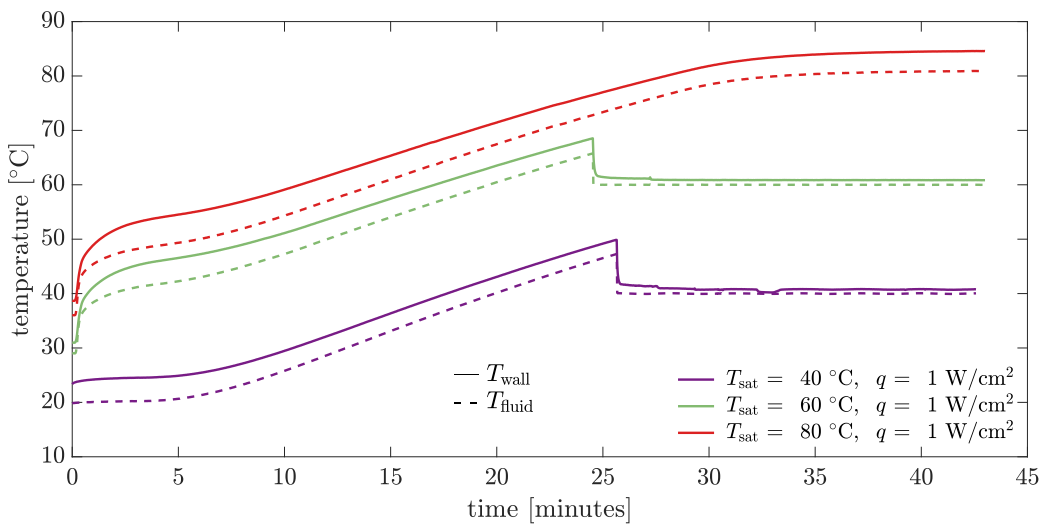

Figure 5.4: Temperature over time for the different saturation temperatures at a constant heat flux of 1 W/cm^2.

In this figure, the superheated liquid phenomenon is clearly visible at saturation temperatures of 40 and 60 °C. The fluid temperature exceeds the corresponding saturation temperature and drops towards the saturation temperature at some point. The superheated liquid temperature is 7.3 and 5.7 °C for a saturation temperature of 40 and 60 °C respectively. It seems that there is no superheated liquid at a saturation temperature of 80 °C. Yet the fluid temperature is 0.9 °C above the saturation temperature and drops at the end of the experiment. As earlier mentioned, the T_{fluid} at the superheating tipping point is sometimes difficult to determine. Figure 5.5 shows the same plot as above but with $T_{\text{liquid,tube,in}}$ and $T_{\text{liquid,tube,out}}$.

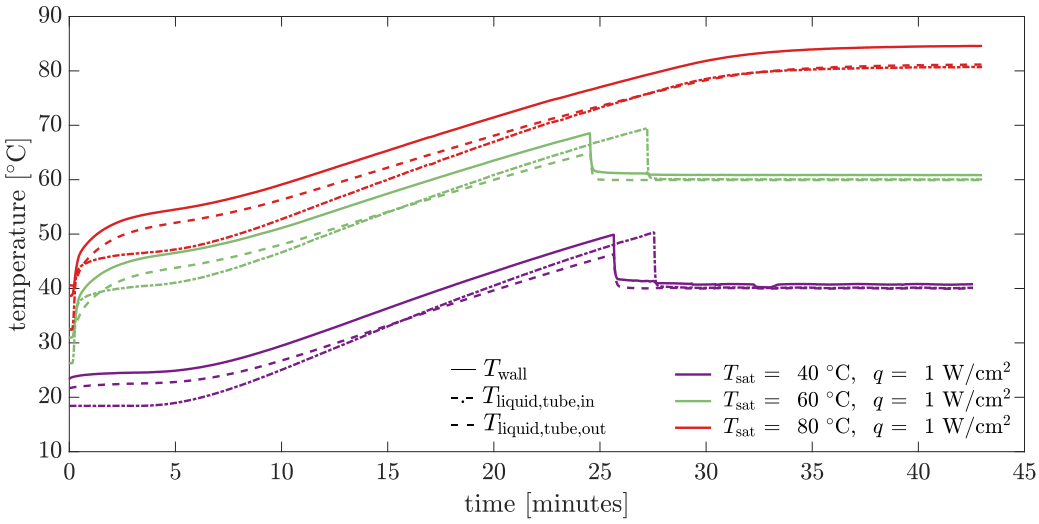

Figure 5.5: Temperature over time for the different saturation temperatures at a constant heat flux of 1 W/cm^2 with $T_{\text{liquid,tube,in}}$ and $T_{\text{liquid,tube,out}}$.

It is visible that $T_{\text{liquid,tube,in}}$ continues while T_{wall} has already jumped back. In the above case, T_{fluid} is determined by taking the average until T_{wall} jumps back. The figures above for the other heat fluxes of 2, 3, 4, and 5 W/cm^2 can be found in Appendix F. In these figures, T_{wall} sometimes does not jump back immediately but drops towards two-phase behavior in several steps. Therefore, T_{fluid} is difficult to determine in several cases. All superheated liquid temperatures for the applied heat fluxes are combined in Figure 5.6.

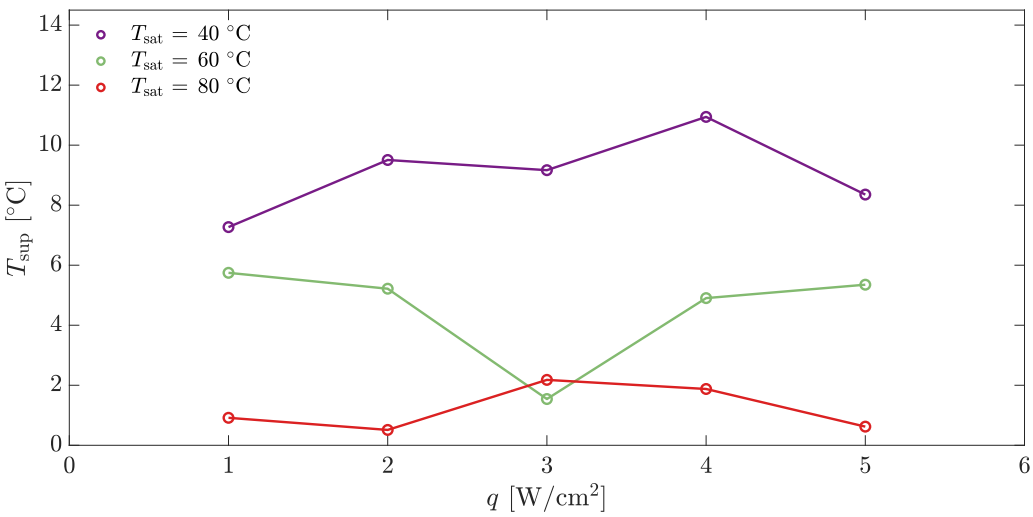

Figure 5.6: Superheated liquid temperature for the different applied heat fluxes and three different saturation temperatures.

A higher superheated liquid temperature is measured for lower saturation temperatures. However, the measured superheated liquid temperature deviates at 60 °C and 3 W/cm^2 since it is below the data point of 80 °C. This may be due to an inaccuracy in the measurement setup or to external factors such as vibration. In Figure F.2, the fluid temperature shows an earlier drop than the tube temperature. From the above figure, no relation can be made between heat flux and the superheated liquid temperature.

Figure 5.7 shows the temperature over time for the saturation temperature of 40 °C and the various heat fluxes as in the previous section. There is a larger temperature gradient between the saturation temperature and the wall temperature when a higher heat flux is applied. In addition, wobbly behavior is visible at a heat flux of 4 and 5 W/cm^2. At 4 W/cm^2, the wall temperature jumps up once while it lasts longer over time for 5 W/cm^2.

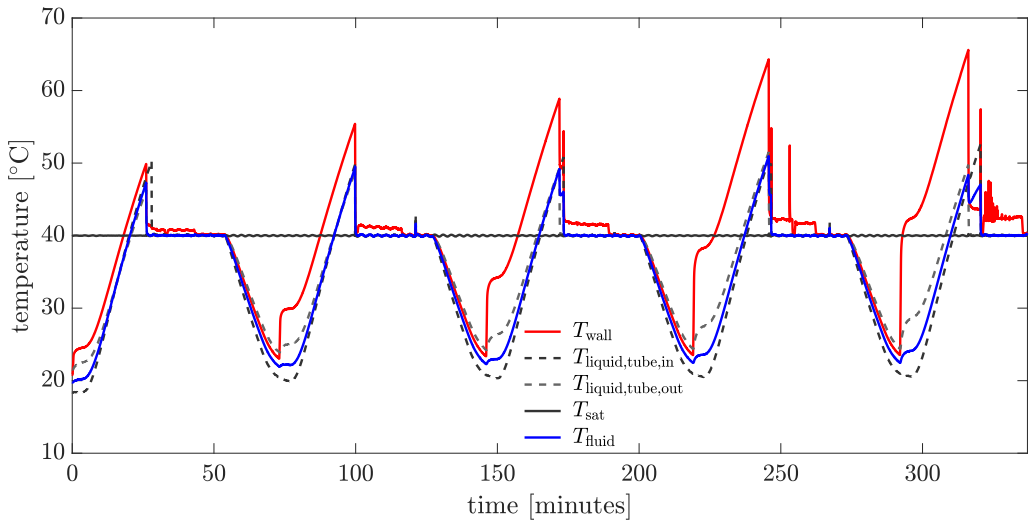

Figure 5.7: Temperature over time for the applied heat fluxes of 1, 2, 3, 4, and 5 W/cm^2 with a saturation temperature of 40 °C.

The figure above for the saturation temperatures of 60 and 80 °C can be seen in Figure F.5 and F.6 in Appendix F.

5.2.1 Results comparison with the modelling

This section compares the results of the modified Young-Laplace equation and the results of Section 4.2 on modelling. In Section 3.5, the superheated liquid temperatures were estimated at 8.8, 4.4, and 2.1 °C for the saturation temperatures of 40, 60, and 80 °C, respectively. These results are compared with the experimental tests, where the superheated liquid temperatures (T_{sup}) were given in Table 5.1.

Table 5.1: Experimental results for the superheated liquid temperature.

	T_{sat} = 40 °C	T_{sat} = 60 °C	T_{sat} = 80 °C
q [W/cm^2]		T_{sup} [°C]	
1	7.3	5.7	0.9
2	9.5	5.2	0.5
3	9.2	1.5	2.2
4	10.9	4.9	1.9
5	8.4	5.4	0.6

The estimated superheated liquid temperatures of 8.8, 4.4, and 2.1 °C for the corresponding saturation temperatures have all been exceeded at some point. However, it is a realistic estimate. The average superheated liquid temperatures are 9.1, 4.5, and 1.2 °C for the saturation temperatures of 40, 60, and 80 °C, respectively. The absolute

deviation is 0.3, 0.1, and 0.9 °C which makes it a suitable estimate for superheating in two-phase MPL thermal management systems.

The modelling of the radial temperature distribution with the convection-diffusion equation for the Hagen-Poiseuille flow provides insight into the location of superheated liquid in the heated tube. The thermocouple is located at 5.60 mm from the beginning of the heated tube. Therefore, no superheated liquid should be measured when $L_{\text{sup}} <$ 5.6 mm. The modelling result are in Table 4.2. Since the inlet temperature is increased over time, these results cannot be compared directly. The modelling uses $T_{\text{in}} = T_{\text{sat}}$. In Figure 5.7, the point where $T_{\text{liquid,tube,in}}$ reaches the saturation temperature represents the situation in the model. At this point, the interest is in the value of T_{fluid} which is unknown. Nevertheless, the model can be used to gain insight into the boiling behavior in the evaporator of a two-phase MPL thermal management system.

5.2.2 Results comparison with the empirical correlations

The theory and modelling section have already described the heat transfer coefficient and various correlations. In this section, the theoretical heat transfer coefficient is compared with the superheated liquid experiments. Equation 2.5 is used to calculate the heat transfer coefficient between the fluid and the wall. T_{fluid} is used from Figure 5.7, F.6, and F.6. In most cases, this produces logical results from the assumed T_{fluid}. Figure 5.8 shows the heat transfer coefficient over time at a saturation temperature of 40 °C and a heat flux of 1 W/cm^2.

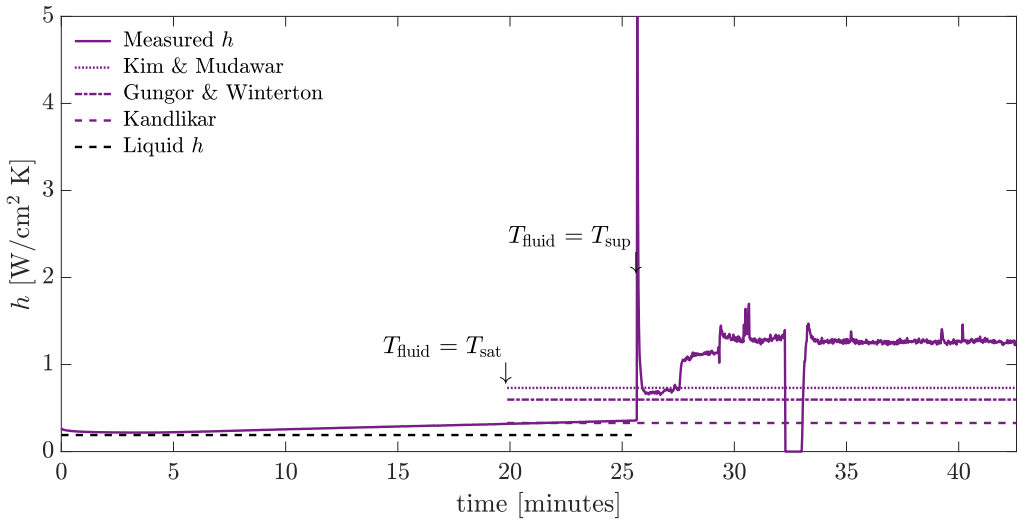

Figure 5.8: Heat transfer coefficient plotted over time for the measured data and the empirical correlations with ammonia as the refrigerant. The saturation temperature is 40 °C and the applied heat flux is 1 W/cm^2. The black arrows represent the time indices at which T_{fluid} reaches the value of T_{sat} and T_{sup}.

In previous heat transfer coefficient plots, the vapor mass fraction was on the x-axis. In the figure above, time is taken as the x-axis since the vapor mass fraction in the experiments showed little variation around $x = 0$. With time on the x-axis, the phase transition is easier to see. The measured heat transfer coefficient h is the drawn line which is not filtered and thus, displays the real measurement data. The analytic liquid heat transfer coefficient continues to the point where the fluid temperature equals the superheated liquid temperature. The empirical correlations for the boiling heat transfer

coefficient start at the theoretical $x = 0$ saturation point. At this point, the fluid temperature is equal to the saturation temperature. In Figure 5.7, this is the intersection of the fluid temperature with the saturation temperature. The high peak at the phase transition in Figure 5.7 is because the difference between the fluid temperature and the wall temperature becomes small over a short time. This results in a peak of 6.2 W/cm^{2}K at this point. Furthermore, the fluid temperature immediately drops towards the saturation temperature, while the wall temperature needs a little more time to become more stable. As a result, it takes a while before a reasonably constant boiling heat transfer coefficient is measured, such as from 35 minutes. Around 33 minutes there was a malfunction in the system that caused the power to go off at the test section. As a result, the heat transfer coefficient briefly drops to zero.

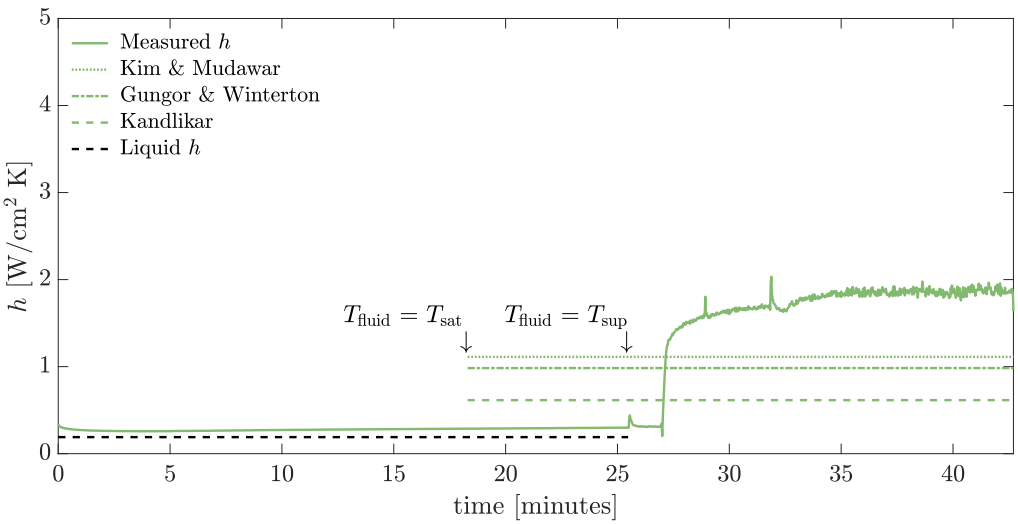

Figure 5.9: Heat transfer coefficient plotted over time for the measured data and the empirical correlations with ammonia as the refrigerant. The saturation temperature is 40 °C and the applied heat flux is 3 W/cm^2. The black arrows represent the time indices at which T_{fluid} reaches the value of T_{sat} and T_{sup}.

Figure 5.9 shows a good representation of the heat transfer coefficient and also clearly shows that the two-phase heat transfer coefficient is much higher than the liquid h. The empirical boiling heat transfer correlation shows an underestimation of the h for all different heat fluxes at a saturation temperature of 40 and 60 °C. At the saturation temperature of 80 °C, the measured two-phase heat transfer coefficient is always between the Kandlikar and Kim & Mudawar correlation.

5.3 Addition of dissolved gases to the experimental setup with the SPIV

After the reference experiments for subcooled and superheated liquid without dissolved gases, the SPIV can be used in the experimental setup. The superheated liquid temperature for different parameters is known from previous section as reference and for comparison. This section treats the addition of different amounts of nitrogen in ammonia and its influence on the boiling process.

First, tests were done to add nitrogen with steps per one sample volume. However, no clear effect was measured of increasing the amount of nitrogen. As a result, the tests

were repeated several times and it was eventually decided to add much more nitrogen. In Figure 5.10, three measurements are shown on the same day where a total of 23, 33, and 43 times nitrogen was added with the SPIV. This equates to a total amount of nitrogen of 0.23, 0.33, and 0.43 mL of nitrogen. The experiments were conducted on the same day to avoid startup effects. As a result, not the entire range of heat fluxes has been tested, but only at 3 and 5 W/cm^2.

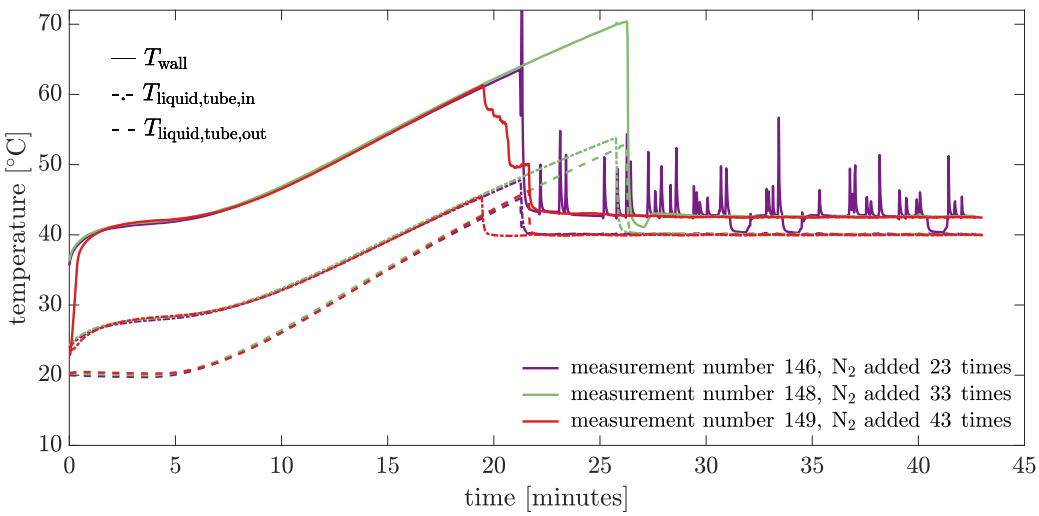

Figure 5.10: Temperature over time for the applied heat flux of 5 W/cm^2 with a saturation temperature of 40 °C for different amounts of added nitrogen.

When measuring with the addition of nitrogen 23 times, strange behavior can be seen on the wall of the heated tube. Wall superheat is a recurring phenomenon that has not previously occurred in two-phase MPL thermal management systems at NLR. With a higher amount of nitrogen, this behavior no longer occurs. At an addition of 33 times, the superheated liquid temperature is the highest, at 23 and 43 times it is both lower. As a result, it was decided to add even more nitrogen, which is shown in Figure 5.11. These measurements were also performed on the same day and one day later than the above measurements.

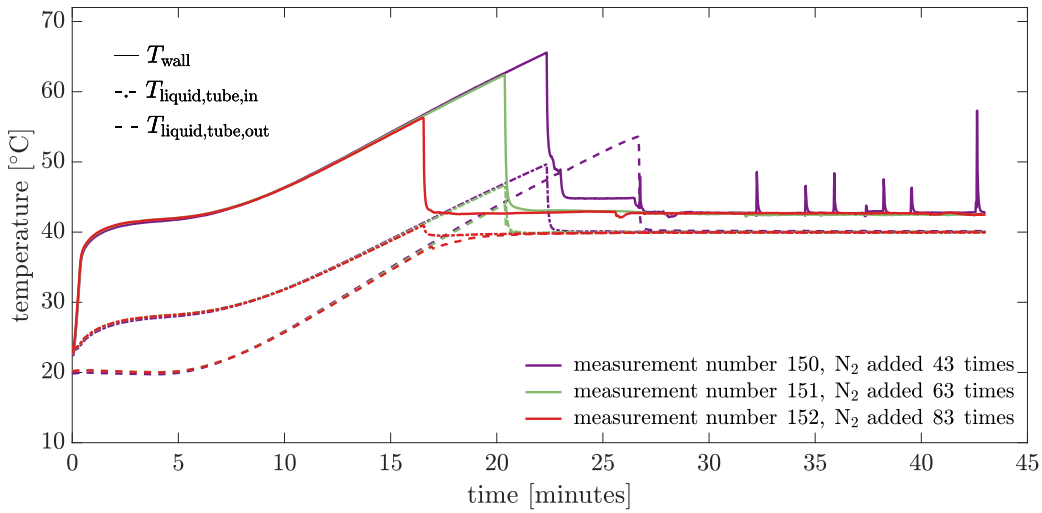

Figure 5.11: Temperature over time for the applied heat flux of 5 W/cm^2 with a saturation temperature of 40 °C for higher amounts of added nitrogen.

Recurring wall superheat was also observed in the first measurement, but not in the other two measurements. This figure shows the desired effect of dissolved nitrogen in ammonia. With a higher amount of dissolved nitrogen in ammonia, the superheated liquid temperature decreases. However, Figure 5.12 does not show this effect when measuring at a heat flux of 3 W/cm^2.

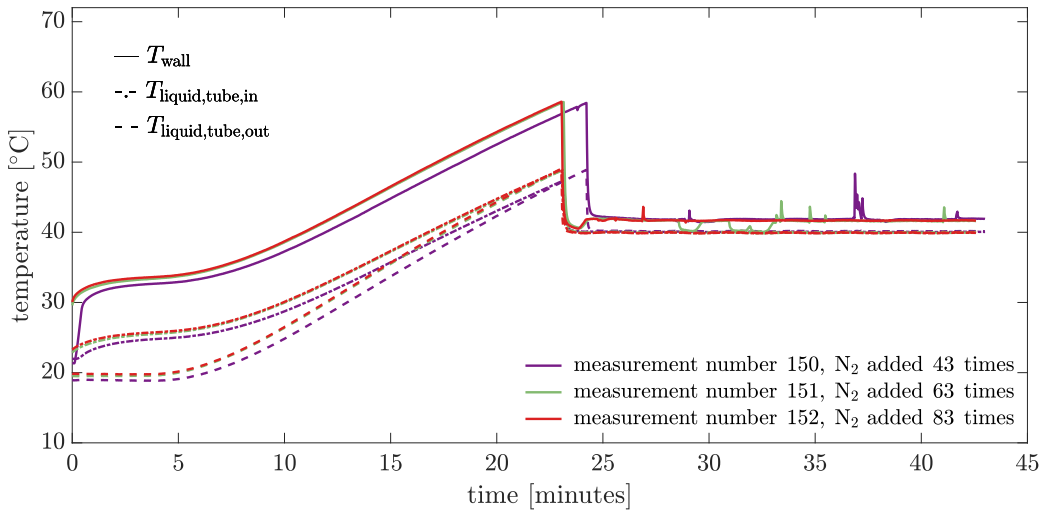

Figure 5.12: Temperature over time for the applied heat flux of 3 W/cm^2 with a saturation temperature of 40 °C for higher amounts of added nitrogen.

The reference experiment shows superheated liquid temperatures of 9.2 and 8.4 °C for the heat flux of 3 and 5 W/cm^2 showed in Table 5.1. The above experiments with dissolved nitrogen were performed on two consecutive days. The superheated liquids temperatures of these measurements are combined into the figure below.

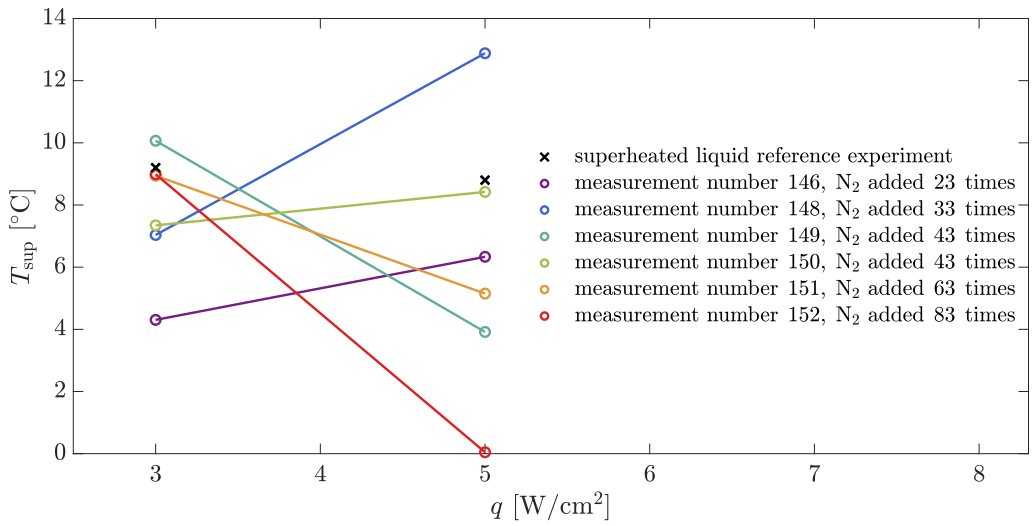

Figure 5.13: Superheated liquid temperature for increasing amount of added nitrogen.

The crosses indicate the results of the reference experiments without added nitrogen. No clear correlation can be seen here between added nitrogen and the superheated liquid temperature. Apart from the above experiments, several tests have been done with different amounts of nitrogen and no unambiguous relationship can be discovered. In addition, a higher saturation temperature of 60 °C and turbulent mass flow of 0.3 g/s were considered.

5.3.1 Possible nitrogen accumulation in the accumulator

A possible reason that no effect of the dissolved gas is observed could be an accumulation of nitrogen in the used accumulator, namely the HCA described in Section 2.1. Since the accumulator contains 97% of the total system volume, it is likely that liquid ammonia with dissolved nitrogen will flow into the accumulator. During operation, the HCA is set to the saturation temperature and it is possible for the nitrogen gas to accumulate in the accumulator. Nitrogen gas (N_2) accumulates between the liquid and vapor ammonia (NH_3) due to its molecular mass.

Different measured parameters in the data files were examined. For example, the influence of the power to keep the accumulator at saturation pressure was assessed. If there is more nitrogen in the accumulator, the power should theoretically decrease over the entire period of measurements. In addition, the startup pressure difference was examined, with a slight increase in the latest measurements with more injected nitrogen. Moreover, the measured saturation temperature for the last measurements is shown in Figure 5.15. A sidenote afterwards is that only 83 injections were made, which means that a maximum of 0.13% of the accumulator can be filled with nitrogen. Initially, the scenario of the accumulator was not taken into account and only the loop volume was considered. This is discussed in more detail in the discussion and recommendations.

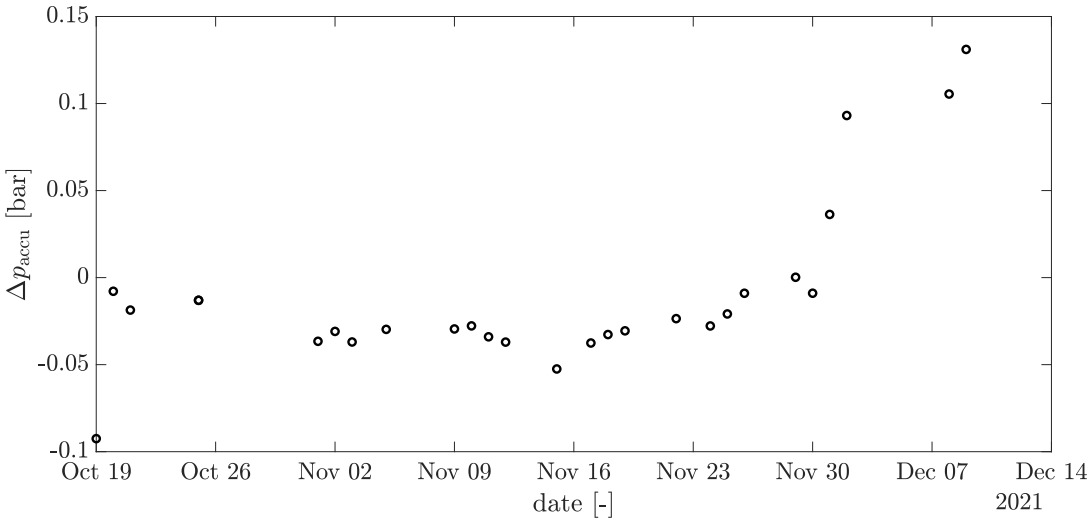

Figure 5.14: Startup pressure difference accumulator.

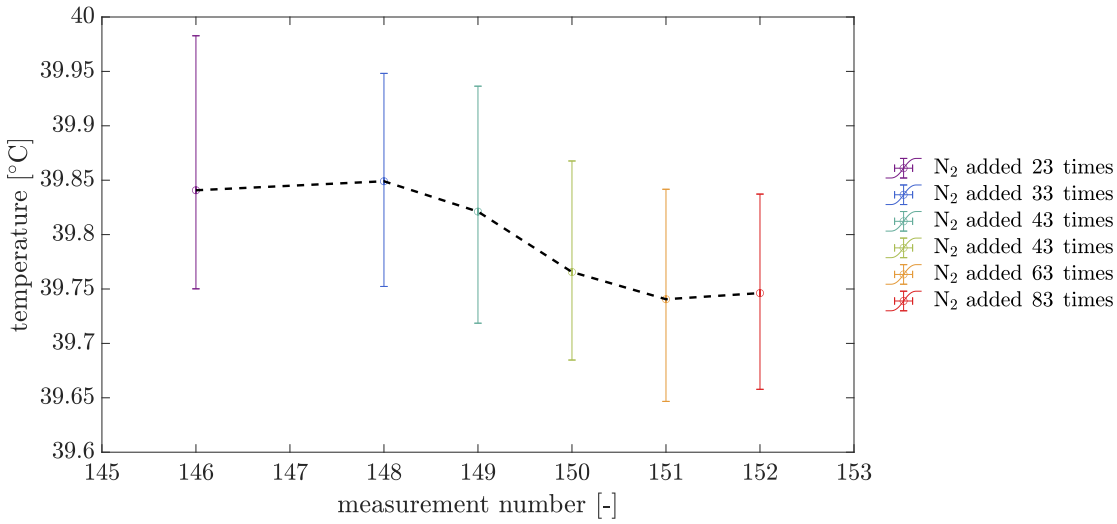

Figure 5.15: Measured saturation temperature accumulator.

6

Discussion

Throughout the research, several points of attention were highlighted. This will be treated in the order of the report and only the most important points are discussed.

First, the method for determining the superheated liquid fit parameter using the modified Young-Laplace equation is assessed. It is assumed that there is a uniform temperature distribution over the radius with spherical bubbles. Homogeneity is assumed, where homogeneous effects are highly likely, such as bubble nucleation on the wall, and the presence of non-spherical bubbles. This theory could be a whole study in itself applied to the typical setup conditions of two-phase MPL thermal management systems.

Next, the usability of the applied solubility data is assessed. This data is from 1937 and the experiment in the presented study with adding nitrogen is based on this data. Moreover, the trend of this data is reversed compared to dissolved gases in water. At higher temperatures, the solubility decreases. An important point to investigate is the physics behind the deviant trend. At the end of the research, another document was found about the solubility of nitrogen in ammonia [68]. A fit equation was made based on six references including the 1937 paper used in this study. Unfortunately, the other references are untraceable. The data from the papers were processed as a group to yield the following smoothing equation:

$$\ln(X_1) = -12.6529 + 5.3410\ln(T/100) + 0.88689\ln(p) + 6.0544 \cdot 10^{-6}p^2 \tag{6.1}$$

Where X_1 is the mole fraction which can be converted to the solubility in g/kg. This is plotted in the same way as Figure 2.24 which is shown in Figure 6.1. The smoothing function does not take into account the theoretical saturation line, which the experimental data from 1937 did. The above figure is converted into an S-T diagram shown in Figure 6.2. It is striking that the trend is similar to Henry's law; a higher temperature and/or pressure means a higher solubility.

In addition, the setup verification described in Section 3.4 did not go entirely as expected. The mean deviation for the liquid heat transfer coefficient is 38% which is a relatively big deviation. However, the average deviation between the reproduction of 5% was a lot more positive, which makes the reproduction more reliable. The error margins in the different sensors were already given at the end of Section 3.6. Another point is to measure T_{fluid}, which is now done by averaging the inlet and outlet temperatures of the evaporator section. The experiments showed that $T_{\text{liquid,tube,in}}$ sometimes shows

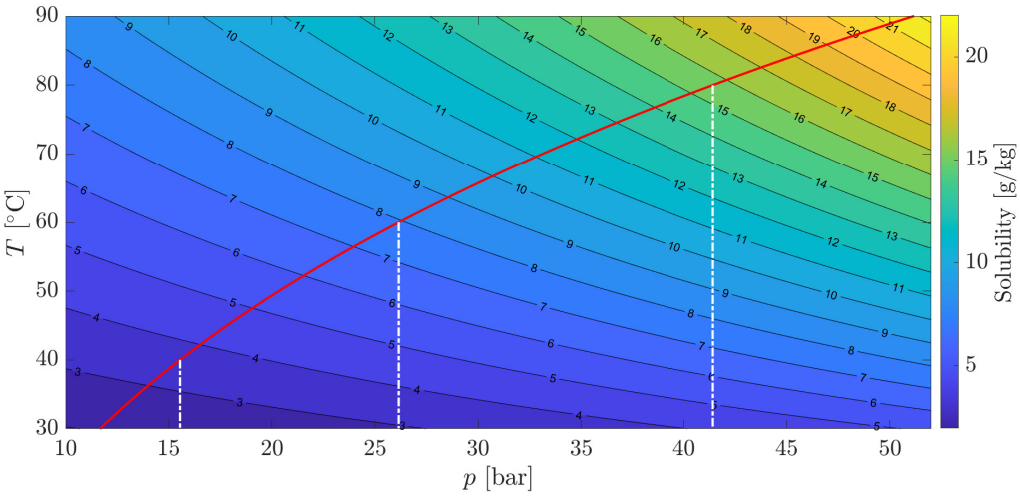

Figure 6.1: Solubility of nitrogen in liquid ammonia with the theoretical saturation line in red and typical operation pressures in white.

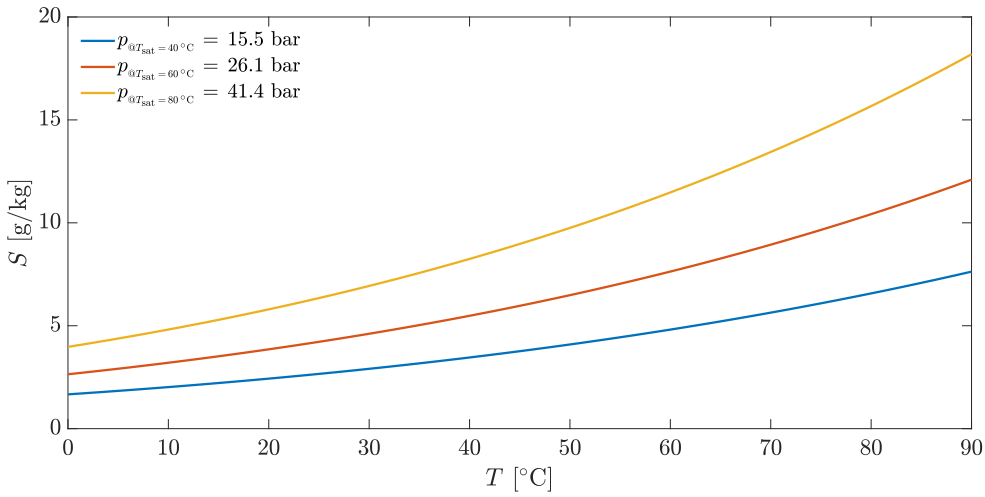

Figure 6.2: Solubility vs temperature plot for nitrogen in liquid ammonia at typical operation pressures.

superheated liquid and $T_{\text{liquid,tube,out}}$ does not. As a result, the average temperature calculation is not entirely realistic.

The experiments with dissolved gas did not yield the desired results. The main question here is why there is no measurable difference after adding nitrogen gas. The cause can be looked at where the nitrogen gas is located in the experimental setup and whether it possibly accumulates. A uniform distribution is assumed after a certain number of cycles. However, liquid ammonia with dissolved nitrogen will flow into the accumulator. Since an HCA is used, the accumulator contains both liquid ammonia and gas. During operation, the HCA is set to the saturation temperature and it is possible for the nitrogen gas to accumulate in the accumulator. When the system is at rest, the accumulator temperature drops back to approximately ambient temperature. As a result, there is uncertainty about the amount of nitrogen that may dissolve again in the liquid ammonia. Moreover, there is uncertainty about the amount of injected nitrogen gas. The tolerance of the sample volume internal diameter is ±0.0254 mm which can have a significant effect

on the volume [69]. So in the case of the used 0.02 mL sample volume, it can be 0.19 or 0.21 mL. At the end of the experiments, the SPIV has been opened more than 100 times and so the liquid ammonia should be saturated. A more ideal experimental setup is discussed in the recommendations chapter.

7

Conclusion

The main research question during this research to answer was if dissolved gases in refrigerants have a reducing effect on the superheated liquid temperature. The hypothesis has neither been confirmed or rejected. With ammonia as refrigerant, no conclusive reduction of superheated liquid temperature as result of solving nitrogen has been found. A follow-up study is needed to find out. However, the research has provided valuable insight into the incipience of subcooled and superheated liquid in two-phase MPL thermal management systems and gained experience.

To answer the research question, several subquestions were formulated. First, the solubility of NCGs in refrigerants is addressed. Many studies have been done on the solubility of gases in water, where Henry's law is often used. However, for typical two-phase refrigerants is less data known. The subcooled and superheated liquid temperature can be quantified for a pure refrigerant flow through a circular channel at a heated wall. An indication of the superheated liquid temperature has been made with the modified Young-Laplace equation. With the convection-diffusion equation and the Hagen-Poiseuille flow valid for fully-developed laminar flow, the temperature distribution and the effect of subcooling and superheating in the evaporator have been obtained. The superheated liquid temperature has been verified with experiments.

The heat flux does not influence the superheated liquid temperature in the studied heat flux regime, but on the location where boiling starts. So at a higher heat flux, the liquid will boil earlier on the wall. At lower heat fluxes, the liquid has more time to develop into a superheated liquid along the length of the heated wall. A higher saturation temperature results in a lower superheated liquid temperature. This is due to the higher surface tension at lower saturation temperatures. In parallel with the hypothesis, the subquestion if dissolved gases in refrigerants improve the boiling heat transfer can neither be confirmed nor rejected. With an enhanced experimental setup, the remaining hypotheses can be assessed experimentally, and the recommendations for this follow-up project are described in the next chapter.

8

Recommendations

As described in the previous chapter, the hypothesis has not been approved or rejected. To be able to do this, a follow-up study for the near future is defined. To answer the main question, a more ideal experimental setup is described in this chapter.

The most important discussion point was why there was no apparent influence of NCGs. To remove the uncertainty of the accumulator, the HCA can be replaced by a PCA. This accumulator is pressure regulated and contains only liquid refrigerant which is not near the saturation temperature. As a result, it is expected that no nitrogen gas can accumulate in the accumulator because the temperature in the accumulator is below the saturation temperature and the solubility cannot be zero. A schematic drawing is shown in Figure 8.1. The gas at system pressure can be air or nitrogen and can be separated from the refrigerant via a bellows, bladder, or diaphragm. It is also important to consider the volume ratio between the accumulator and the rest of the loop. In the current setup, 97% of the system volume was in the accumulator.

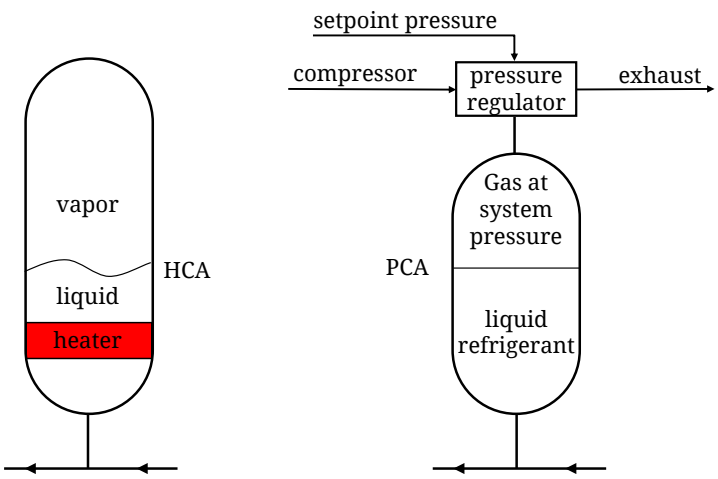

Figure 8.1: Schematic drawing of an HCA at the left and a PCA at the right.

A recent study uses a viewing glass in combination with a high-speed camera to visualize the liquid-vapor mixture [54] for a study into subcooled liquid. This could also be an option in a new experimental setup to visualize the vapor bubbles and the NCGs. In addition, several viewing glasses could then be implemented to gain a better insight

into where the bubbles are located and where they originate. Suitable locations for the viewing glasses could then be after the SPIV, before and after the preheater, and before and after the evaporator. To better verify the convection-diffusion model and to better measure superheated liquid, the test section could be made longer to accommodate more thermocouples. This makes it possible to better determine the location of the superheated liquid and the superheated liquid temperature. A disadvantage of this is the possibly lower heat flux that can be applied to the test tube or less uniform heating, so this must be taken into consideration. In addition, it would be beneficial to have more control over the inlet temperature of the evaporator. In the current setup, this was solved by the PEEK tubing that was embedded in the first thermostated plate. For instance, this could be done with an extra condenser.

To better understand the solubility of NCGs in refrigerants, standalone solubility tests could be performed with the typical two-phase refrigerants. A separate setup could be made for this, which could be tested for different two-phase refrigerants. Wall bubble nucleation is being researched. However, there is still a lack of knowledge on wall bubble nucleation for dissolved gasses. Once this research reaches a new level of understanding, the understanding of the boiling process in two-phase MPL thermal management systems will be advanced. An in-depth study on bubble nucleation is an opportunity to better connect the underlying theory to the boiling process in two-phase MPL thermal management systems.

Bibliography

[1] P. Rincon, "COP26: New global climate deal struck in Glasgow." https://www.bbc.com/news/world-59277788. Online, retrieved on December 17th 2021.

[2] A. Dewan and A. Cassidy, "COP26 ended with the Glasgow Climate Pact. Here's where it succeeded and failed." https://edition.cnn.com/2021/11/14/world/cop26-glasgow-climate-pact-intl-cmd/index.html. Online, retrieved on December 17th 2021.

[3] COP26, "UN Climate Change Conference UK 2021." https://ukcop26.org/. Online, retrieved on December 17th 2021.

[4] COP26, "International Aviation Climate Ambition Coalition." https://ukcop26.org/cop-26-declaration-international-aviation-climate-ambition-coalition. Online, retrieved on December 17th 2021.

[5] M. Zimmer, "Boeing's sustainable aerospace vision takes flight at COP26." https://onfirstup.com/boeing/BNN/articles/boeing-s-sustainable-aerospace-vision-takes-flight-at-cop26-1?bypass_deeplink=true. Online, retrieved on December 17th 2021.

[6] C. Henderson, "A record-breaking commercial-scale hydrogen plane has taken off in the UK, with more set to join it soon. How far can such planes go in cutting the aviation industry's emissions?." https://www.bbc.com/future/article/20210401-the-worlds-first-commercial-hydrogen-plane. Online, retrieved on December 17th 2021.

[7] Airbus, "ZEROe; Towards the world's first zero-emission commercial aircraft." https://www.airbus.com/en/innovation/zero-emission/hydrogen/zeroe. Online, retrieved on December 18th 2021.

[8] Embraer, "Future Aircraft Concepts." https://embraercommercialaviationsustainability.com/concepts. Online, retrieved on December 18th 2021.

[9] Greenspec, "Fuel Cells: Heat and Electricity." https://www.greenspec.co.uk/building-design/fuel-cells/#:~:text=Fuel%20Cells%3A%20Heat%20and%20Electricity,-%E2%80%A2&text=A%20fuel%20cell%20is%20a,gas%2C%20methanol%2C%20etc.)&text=Engine%2Dbased%20systems%20(typically%201.5,buildings%20with%20low%20heat%20demand. Online, retrieved on December 18th 2021.

[10] A. Wileman, S. Aslam, and S. Perinpanayagam, "A road map for reliable power electronics for more electric aircraft," *Progress in Aerospace Sciences*, vol. 127, p. 100739, 2021.

[11] V. Madonna, P. Giangrande, and M. Galea, "Electrical power generation in aircraft: Review, challenges, and opportunities," *IEEE Transactions on Transportation Electrification*, vol. 4, no. 3, pp. 646–659, 2018.

[12] G. Buticchi, S. Bozhko, M. Liserre, P. Wheeler, and K. Al-Haddad, "On-board microgrids for the more electric aircraft—technology review," *IEEE Transactions on Industrial Electronics*, vol. 66, no. 7, pp. 5588–5599, 2019.

[13] G. Zhang and S. G. Kandlikar, "A critical review of cooling techniques in proton exchange membrane fuel cell stacks," *International Journal of Hydrogen Energy*, vol. 37, no. 3, pp. 2412–2429, 2012.

[14] T. Luten, "Design of a cooling system for fuel cell-powered electrical aircraft," 2021.

[15] A. Fly and R. Thring, "A comparison of evaporative and liquid cooling methods for fuel cell vehicles," *International Journal of Hydrogen Energy*, vol. 41, 06 2016.

[16] M. Ellis and C. Kurwitz, "Development of a pumped two-phase system for spacecraft thermal control," *46th International Conference on Environmental Systems*, 07 2016.

[17] H. van Gerner, T. van den berg, J. Es, A. Tailliez, A. Walker, C. Ortega, M. Centeno, and C. Castro, "Preliminary design of a mechanically pumped cooling system for active antennae," *50rd International Conference on Environmental Systems*, 07 2021.

[18] F. Barbir, *PEM Fuel Cells, Theory and Practice.* (Second Edition), London: Elsevier, 2013.

[19] O. Al-Yahia and D. Jo, "Onset of nucleate boiling for subcooled flow through a one-side heated narrow rectangular channel," *Annals of Nuclear Energy*, vol. 109, pp. 30–40, 2017.

[20] S. Kandlikar, D. Li, S. Colin, S. Garimella, and M. King, *Heat Transfer and Fluid Flow in Minichannels and Microchannels.* (First Edition), London: Elsevier, 2005.

[21] S. Yaoa, X. Huang, Y. Song, Y. Shen, and S. Zhang, "Effects of nanoparticle types and size on boiling feat transfer performance under different pressures," *AIP Advances 8, 025005*, 2018.

[22] P. Wu and T. Simon, "Effects of dissolved gases on subcooled flow boiling from small heated regions with and without streamwise concave curvature," *4th Intersociety Conference on Thermal Phenomena in Electronic Systems (I-THERM)*, pp. 23–31, 1994.

[23] H. Müller-steinhagen, N. Epstein, and A. Watkinson, "Effect of dissolved gases on subcooled flow boiling heat transfer," *Chemical Engineering and Processing: Process Intensification*, vol. 23, no. 2, pp. 115–124, 1988.

[24] M. Steinke and S. Kandlikar, "Control and effect of dissolved air in water during flow boiling in microchannels," *International Journal of Heat and Mass Transfer*, vol. 47, pp. 1925–1935, 04 2004.

[25] H. van Gerner, J. Es, A. Pauw, G. van Donk, E. Laudi, Z. He, C. Gargiulo, and B. Verlaat, "Ams02 tracker thermal control cooling system commissioning and operational results," *43rd International Conference on Environmental Systems*, 07 2013.

[26] H. van Gerner, R. van Benthem, J. Es, D. Schwaller, and S. Lapensée, "Fluid selection for space thermal control systems," *44th International Conference on Environmental Systems*, 07 2014.

[27] National Fire Protection Association, "NFPA 704, Standard System for the Identification of the Hazards of Materials for Emergency Response." https://www.unep.org/ozonaction/who-we-are/about-montreal-protocol. Online, retrieved on December 28th 2021.

[28] SafetySign, "NFPA Reference Chart." https://www.safetysign.com/products/6903/nfpa-reference-chartl. Online, retrieved on December 28th 2021.

[29] UN Environment Programme (UNEP), "About Montreal Protocol." https://www.unep.org/ozonaction/who-we-are/about-montreal-protocol. Online, retrieved on December 28th 2021.

[30] SKM Enviros, "Possible Bans for New RAC Equipment." https://ec.europa.eu/clima/system/files/2016-11/refrigeration_air_conditioning_en.pdf. Online, retrieved on December 28th 2021.

[31] United States Environmental Protection Agency (EPA), "Refrigerant Transition & Environmental Impacts." https://www.epa.gov/mvac/refrigerant-transition-environmental-impacts. Online, retrieved on December 28th 2021.

[32] F. Incropera, D. Dewitt, T. Bergman, and A. Lavine, *Fundamentals of Heat and Mass Transfer.* (Sixth Edition), John Wiley & Sons, 2006.

[33] S. Kandlikar, M. Shoji, and V. Dhir, *Handbook of Phase Change: Boiling and Condensation.* (First Edition), Boca Raton: Taylor & Francis Group, 1999.

[34] V. Kalikmanov, *Nucleation Theory.* (Second Edition), New York: Springer, 2018.

[35] S. Saha, *Microchannel Phase Change Transport Phenomena.* Oxford: Elsevier, 2015.

[36] L. Tong and Y. Tang, *Boiling Heat Transfer and Two-Phase Flow.* (Second Edition), New York: Taylor & Francis Group, 1997.

[37] J. Thome and A. Cioncolini, *Two-Phase Flow Pattern Maps for Microchannels*, pp. 47–84. 10 2015.

[38] C. Ong and J. Thome, "Macro-to-microchannel transition in two-phase flow: Part 1 – two-phase flow patterns and film thickness measurements," *Experimental Thermal and Fluid Science*, vol. 35, pp. 37–47, 2011.

[39] Y. Çengel and A. Ghajar, *Heat and Mass Transfer: Fundamentals & Applications.* New York: McGraw Hill Education, 2015.

[40] G. Hewitt and D. Roberts, "Studies of two-phase flow patterns by simultaneous x-ray and flast photography," *Atomic Energy Research Establishment*, 1969.

[41] J. Thome, "Heat transfer engineering data book iii," 2006.

[42] L. Wojtan, T. Ursenbacher, and J. Thome, "Investigation of flow boiling in horizontal tubes: Part I, a new diabatic two-phase flow pattern map," *International Journal of Heat and Mass Transfer*, vol. 48, pp. 2955–2969, 2005.

[43] F. Dittus and L. Boelter, "Heat transfer in automobile radiators of the tubular type," *University of California Publications in Engineering*, vol. 2, pp. 443–461, 1930.

[44] Y. Çengel, J. Cimbala, and R. Turner, *Fundamentals of Thermal-Fluid Sciences.* New York: McGraw Hill Education, 2017.

[45] B. Bhabesh, "A new correlation for heat transfer during flow boiling," 1981.

[46] Y. Shuai, W. Cheng, Y. Nian, Q. Zhong, Y. Fan, and J. He, "Evaluation of prediction methods for heat transfer coefficient of annular flow and a novel correlation," *Applied Thermal Engineering*, vol. 114, pp. 10–23, 2017.

[47] S. Kandlikar, "A general correlation for saturated two-phase flow boiling heat transfer inside horizontal and vertical tubes," *Journal of Heat Transfer*, vol. 112, no. 1, pp. 219–228, 1990.

[48] S. Kandlikar and P. Balasubramanian, "An extension of the flow boiling correlation to transition, laminar, and deep laminar flows in minichannels and microchannels," *Journal of the American Chemical Society*, vol. 59, no. 10, pp. 1984–1987, 2004.

[49] K. Gungor and R. Winterton, "Simplified general correlation for saturated flow boiling and comparisons of correlations with data," *Chemical Engineering Research & Design*, vol. 65, pp. 148–156, 1987.

[50] J. Chen, "Correlation for boiling heat transfer to saturated fluids in convective flow," *Industrial & Engineering Chemistry Process Design and Development*, vol. 5, no. 3, pp. 322–329, 1966.

[51] H. Wang and X. Fang, "Evaluation analysis of correlations of flow boiling heat transfer coefficients applied to ammonia," *Journal of Heat Transfer Engineering*, vol. 37, no. 1, pp. 32–34, 2016.

[52] S. Kim and I. Mudawar, "Universal approach to predicting saturated flow boiling heat transfer in mini/micro-channels - part i. dryout incipience quality," *International Journal of Heat and Mass Transfer*, vol. 64, pp. 1226–1238, 2013.

[53] S. Kim and I. Mudawar, "Universal approach to predicting saturated flow boiling heat transfer in mini/micro-channels - part ii. two-phase heat transfer coefficient," *International Journal of Heat and Mass Transfer*, vol. 64, pp. 1239–1256, 2013.

[54] E. Bediako, P. Dancova, and T. Vít, "Experimental study of horizontal flow boiling heat transfer coefficient and pressure drop of r134a from subcooled liquid region to superheated vapor region," *Energies*, vol. 15, p. 681, 01 2022.

[55] B. Averill and P. Eldredge, *General Chemistry: Principles, Patterns, and Applications.* Saylor Academy, 2011.

[56] W. Sha and V. Shah, "Bubble dynamics in a superheated liquid," 1977.

[57] T. Chen and S. Garimella, "Effects of dissolved air on subcooled flow boiling of a dielectric coolant in a microchannel heat sink," 06 2005.

[58] R. Bird, W. Stewart, and E. Lightfoot, *Transport Phenomena.* (Second Edition), New York: John Wiley & Sons, Inc., 2018.

[59] I. Dincer and M. Ezzat, "Energy Production." `https://www.sciencedirect.com/topics/engineering/non-condensable-gas#:~:text=Non%2Dcondensable%20gases%20(NCG),dissolved%20in%20the%20geothermal%20water.` Online, retrieved on September 28th 2021.

[60] L. Cecchinato, E. Fornasieri, M. Marcer, and C. Zilio, "The effects of non-condensable gases in household refrigerators," 2004.

[61] Wikipedia, "Henry's law." `https://en.wikipedia.org/wiki/Henry%27s_law.` Online, retrieved on September 7th 2021.

[62] V. Vinš and J. Hruby, "Solubility of nitrogen in one-component refrigerants: Prediction by pc-saft eos and a correlation of henry's law constants," *International Journal of Refrigeration*, vol. 34, 12 2011.

[63] R. Wiebe and V. Gaddy, "The solubility in liquid ammonia of hydrogen at 0° and of nitrogen at 0, 50, 75, 90 and 100° at pressures to 1000 atmospheres. critical phenomena of ammonia-nitrogen mixtures," *Journal of the American Chemical Society*, vol. 59, no. 10, pp. 1984–1987, 1937.

[64] K. Rouwenhorst and A. Valera-Medina, "Haber-Bosch Process." `https://www.sciencedirect.com/topics/engineering/haber-bosch-process`. Online, retrieved on September 7th 2021.

[65] B. 3D, "PEEK - Aeroapce industry." `https://www.bond3d.com/market/peek-aerospace-products/`. Online, retrieved on March 4th 2022.

[66] VICI, "Valco injectors and selectors - technical support." `https://www.vici.com/support/app/app11j.php`. Online, retrieved on September 7th 2021.

[67] W. van den Bergh, H. Moran, J. Dirker, C. Markides, and J. Meyer, "Effect of low heat and mass fluxes on the boiling heat transfer coefficient of r-245fa," *International Journal of Heat and Mass Transfer*, vol. 180, p. 121743, 12 2021.

[68] R. Battino, T. Rettich, and T. Tominaga, "The solubility of nitrogen and air in liquids," *Journal of Physical and Chemical Reference Data*, vol. 13, no. 2, 1984.

[69] VICI, "Valve accessories - sample loops." `https://www.vici.com/v_access/sample_loops.php`. Online, retrieved on September 7th 2021.

[70] E. ToolBox, "Roughness & Surface Coefficients." `https://www.engineeringtoolbox.com/surface-roughness-ventilation-ducts-d_209.html`. Online, retrieved on April 18th 2022.

[71] L. Moody, "Friction factors for pipe flow," *Transactions of the ASME*, vol. 66, no. 8, pp. 671–684, 1944.

[72] Wikipedia, "Standard conditions for temperature and pressure." `https://en.wikipedia.org/wiki/Standard_conditions_for_temperature_and_pressure`. Online, retrieved on September 7th 2021.

[73] VICI, "Valco injectors and selectors - leak testing." `https://www.vici.com/vval/vval_leak.php`. Online, retrieved on September 7th 2021.

A

Heat transfer calculation

A.1 Liquid heat transfer

To calculate the heat transfer coefficient for single-phase flow, the Nusselt number is needed. For convenience, Equations 2.7 and 2.8 are repeated below.

$$\mathrm{Nu} = 4.36 \qquad \mathrm{Re} < 2300 \tag{A.1}$$

$$\mathrm{Nu} = \frac{(f/8)\,(\mathrm{Re} - 1000)\,\mathrm{Pr}}{1 + 12.7(f/8)^{1/2}\left(\mathrm{Pr}^{2/3} - 1\right)} \qquad \mathrm{Re} > 3000, 0.5 \leq \mathrm{Pr} \leq 2000 \tag{A.2}$$

Where Pr is the Prandtl number, defined as the ratio of momentum diffusivity to thermal diffusivity.

$$\mathrm{Pr} = \frac{c_p \mu}{k} \tag{A.3}$$

For fully developed turbulent flow in smooth circular tubes, the Blasius correlation is widely used as friction factor f. However, this is only valid for smooth tubes. To consider the surface roughness, the more accurate Haaland equation can be used which is an explicit approximation of the Colebrook equation [44].

$$f = \left(-1.8 \log\left(\left(\frac{\varepsilon}{3.7d}\right)^{1.11} + \frac{6.9}{\mathrm{Re}}\right)\right)^{-2} \qquad \mathrm{Re} > 3000, 0.5 \leq \mathrm{Pr} \leq 2000 \tag{A.4}$$

In the Haaland equation, ε is the surface roughness of the tube. The value usually found in the literature for the surface roughness in this case is 1.0 to 2.0 µm [70]. The used surface roughness during this research is discussed in detail in Chapter 3 about the used experimental setup.

According to Equations A.1 and A.2, no Nusselt number is specified between a Reynolds number of 2300 and 3000. This range is called the transition region and the flow can be either laminar or turbulent or something in between. It is convenient to use a smoothing function between the laminar and turbulent friction coefficients in order to prevent instabilities in numerical simulations or iteration procedures. The smoothing function interpolates the friction factor for both regimes [14]:

$$\zeta = \frac{1}{1 + e^{(\mathrm{Re}-2300)/200}} \tag{A.5}$$

$$f = (1-\zeta) f_{\mathrm{laminar}} + \zeta f_{\mathrm{turbulent}} \qquad 2300 < \mathrm{Re} \leq 3000 \tag{A.6}$$

Where the 200 in the above equation is a characteristic width. The laminar and turbulent friction factor with smoothing function can be plotted in a moody diagram [71], which is in non-dimensional form. The friction factor for fully developed flow as a function of the Reynolds number and the surface roughness ε is shown in Figure A.1. Note that the friction factor of a laminar flow is not influenced by the surface roughness. The red line in the figure indicates the friction factor calculated with the smoothing function for 0.002.

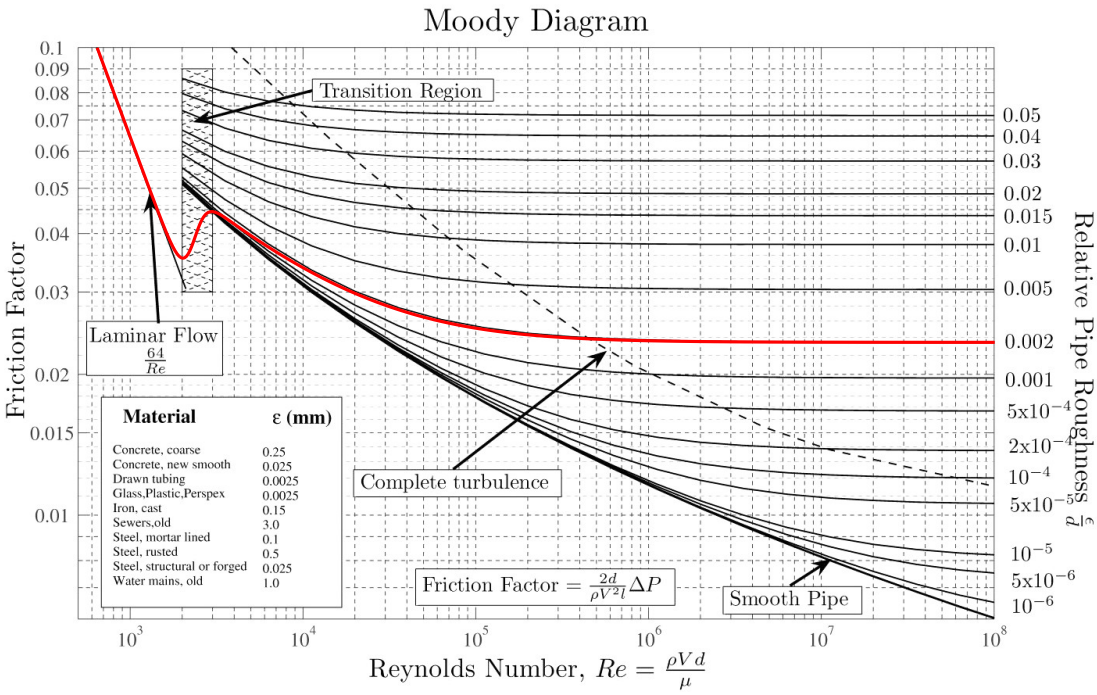

Figure A.1: The Moody diagram represents the friction factor as a function of the Reynolds number for different values of the surface roughness for fully developed flow in circular tubes [71].

A.2 Boiling heat transfer

As discussed in Section 2.3.1, there are many empirical correlations for two-phase flow, but no universal ones. To compare the best applicable correlation of Kandlikar for two-phase MPL thermal management systems, the Gungor & Winterton and Kim & Mudawar correlations are used. The various correlations with associated equations are explained below.

A.2.1 Kandlikar empirical correlation

The main equation in this research for the two-phase heat transfer coefficient of Kandlikar is already given in Equation 2.9. For convenience, it is repeated below.

$$h_{tp} = \max \begin{cases} h_{tp,nbd} = \left[0.6683\mathrm{Co}^{-0.2}(1-x)^{0.8} + 1058.0\mathrm{Bo}^{0.7}(1-x)^{0.8}\right] h_l \\ h_{tp,cbd} = \left[1.136\mathrm{Co}^{-0.9}(1-x)^{0.8} + 667.2\mathrm{Bo}^{0.7}(1-x)^{0.8}\right] h_l \end{cases} \tag{A.7}$$

Where the Convection number is:

$$\mathrm{Co} = \left(\frac{1-x}{x}\right)^{0.8} \left(\frac{\rho_v}{\rho_l}\right)^{0.5} \tag{A.8}$$

The Boiling number is shown below.

$$\mathrm{Bo} = \frac{q}{Gh_{lv}} \tag{A.9}$$

A.2.2 Gungor & Winterton empirical correlation

Next, the used Gungor & Winterton empirical correlation is shown in Equation A.10 [49]:

$$h_{tp} = \left[1 + 3000\mathrm{Bo}^{0.86} + \left(\frac{1.12x}{1-x}\right)^{0.75} \left(\frac{\rho_l}{\rho_v}\right)^{0.41}\right] h_l \tag{A.10}$$

A.2.3 Kim & Mudawar empirical correlation

Finally, the Kim & Mudawar empirical correlation is shown below [53].

$$h_{tp} = \left(h_{tp,nbd}^2 + h_{tp,cbd}^2\right)^{0.5} \tag{A.11}$$

Where the contribution of nucleate and convective boiling are:

$$h_{tp,nbd} = \left[2345\left(\mathrm{Bo}\frac{P_H}{P_F}\right)^{0.70} p_R^{0.38}(1-x)^{-0.51}\right] h_l \tag{A.12}$$

$$h_{tp,cbd} = \left[5.2\left(\mathrm{Bo}\frac{P_H}{P_F}\right)^{0.08} \mathrm{We}^{-0.54} + 3.5\left(\frac{1}{X_{tt}}\right)^{0.94} \left(\frac{\rho_v}{\rho_l}\right)^{0.25}\right] h_l \tag{A.13}$$

Where P_H is the heated perimeter of the channel and P_F the wetted perimeter. In this study, $P_H/P_F = 1$ in all cases. p_R is the reduced pressure and corresponds to the system pressure divided by the critical pressure. X_{tt} is the dimensionless dimensionless Lockhart-Martinelli parameter and is shown in Equation A.14.

$$X_{tt} = \left(\frac{1-x}{x}\right)^{0.9} \left(\frac{\mu_l}{\mu_v}\right)^{0.1} \left(\frac{\rho_v}{\rho_l}\right)^{0.5} \tag{A.14}$$

Equation A.15 is used to calculate the dry-out incipience quality x_{di} [52].

$$x_{di} = 1.4\mathrm{We}^{0.03} p_R^{0.08} - 15.0\left(\mathrm{Bo}\frac{P_H}{P_F}\right)^{0.15} \mathrm{Ca}^{0.35} \left(\frac{\rho_v}{\rho_l}\right)^{0.06} \tag{A.15}$$

Where We is the Weber number and Ca the Capillary number, both shown below.

$$\mathrm{We} = \frac{dG^2}{\rho_l \sigma} = \frac{\rho_l u^2 d}{\sigma} \tag{A.16}$$

$$\mathrm{Ca} = \frac{\mu G^2}{\rho_l \sigma} = \frac{\mathrm{We}}{\mathrm{Re}} \tag{A.17}$$

B

Experimental solubility data

The data from the available papers were converted in MATLAB to create contour plots. This gives a clear overview of the solubility at different temperatures and pressures. The solubility here is still expressed in cc/g as it is in the original paper [63]. During this study, the more practical unit g/kg is used and these plots were given in Section 2.6. The dissolved gas is treated at standard temperature and pressure (STP). Since the paper is from 1937, STP was defined as a temperature of 273.15 K (0 °C) and an absolute pressure of exactly 1 atm (101325 Pa = 1.01325 bar(a)) until 1982 [72]. Since 1982, STP has been defined at the same temperature but with an absolute pressure of 1 bar.

B.1 Experimental data for the solubility of nitrogen gas in liquid ammonia

The figure below is comparable with Figure 2.23, only the solubility unit is different.

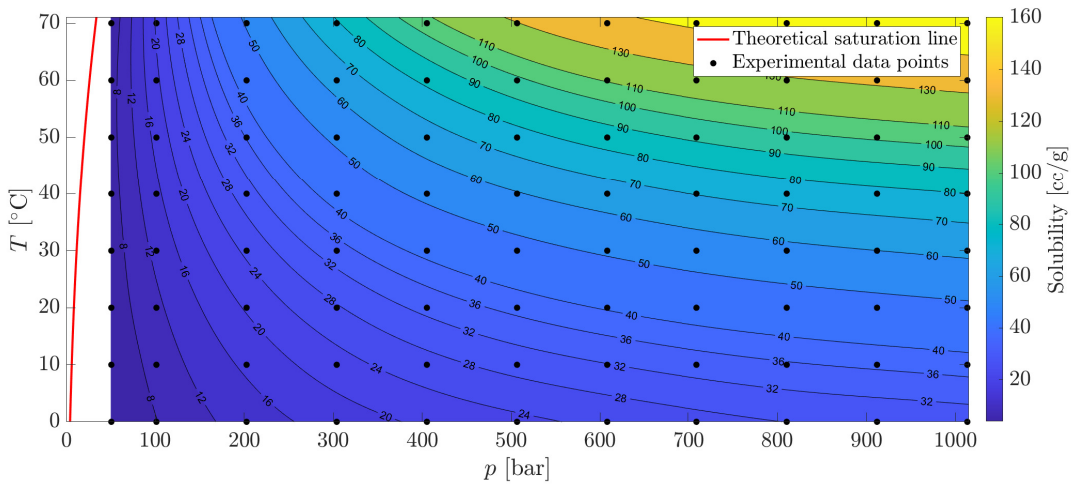

Figure B.1: Original interpolated experimental data for the solubility in cc/g of nitrogen gas in liquid ammonia.

The figure below is comparable with Figure 2.24.

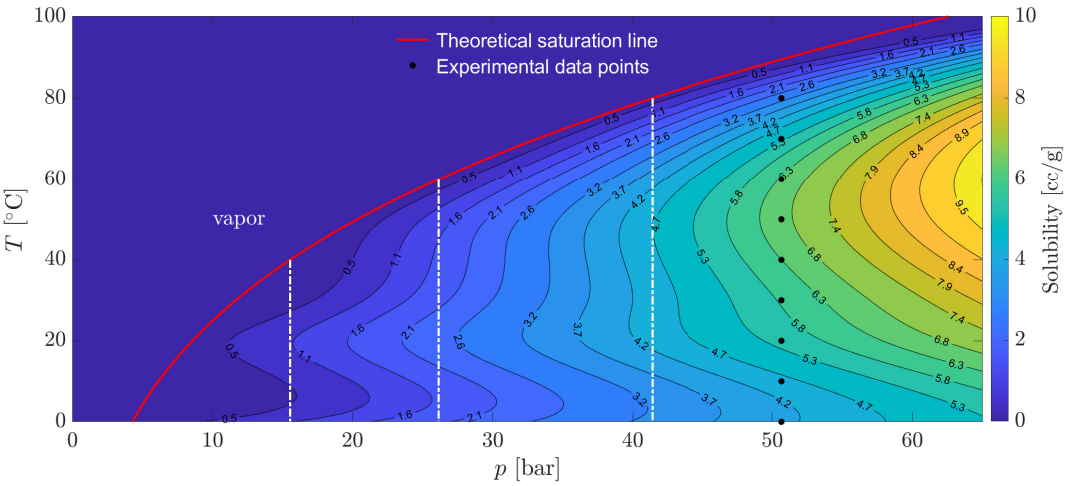

Figure B.2: Extrapolated experimental data for the solubility in cc/g of nitrogen gas in liquid ammonia.

B.2 Experimental data for the solubility of hydrogen gas in liquid ammonia

Other NCGs have also been studied. For example, there is experimental data for the solubility of hydrogen in liquid ammonia from the same paper [63]. The figures are shown below, but after considering whether to use nitrogen as NCG, the data below is not treated in detail. It is preferable to work with nitrogen instead of hydrogen because of the low molecular mass.

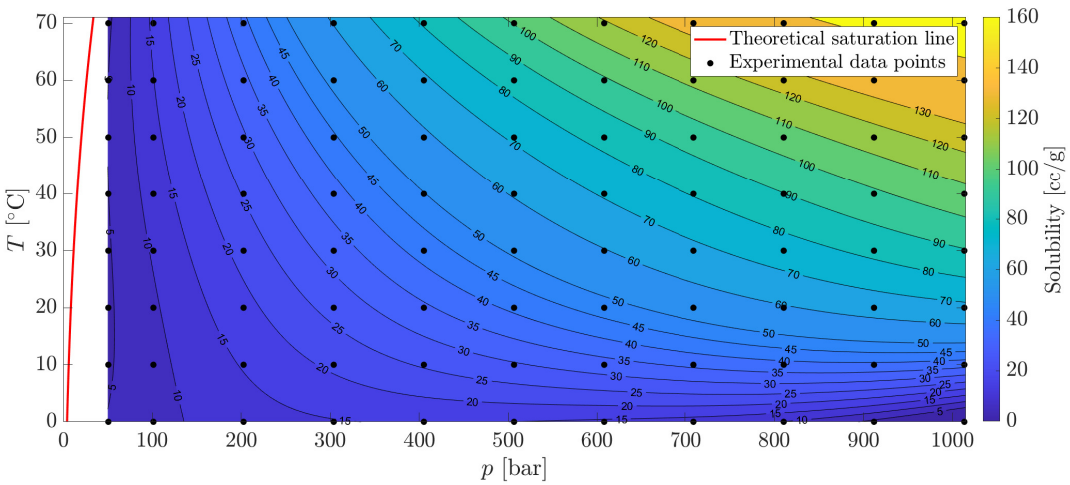

Figure B.3: Interpolated experimental data for the solubility of hydrogen in liquid ammonia.

The data for hydrogen has also been extrapolated to the range of interest for two-phase MPL thermal management systems.

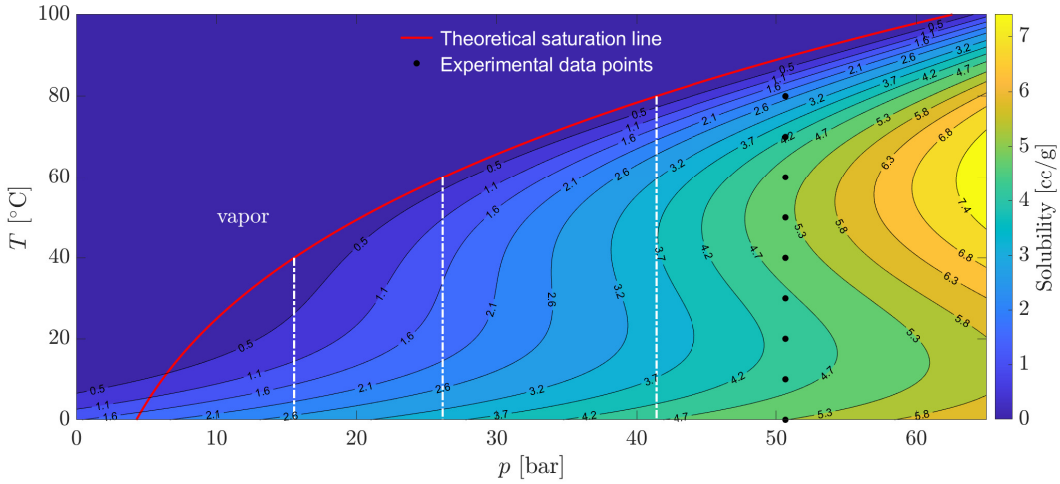

Figure B.4: Extrapolated experimental data for the solubility of hydrogen in liquid ammonia.

C

Derivation of the inside wall temperature in the experimental setup

For the calculation of the heat transfer coefficient, the temperature must be known at the fluid-wall interface. However, only the outer wall temperature T_2 from Figure 3.5 can be measured, and not the temperature at the interface T_1. Fortunately, the temperature at the interface can be derived from the outside wall temperature of the tube with the heat diffusion equation.

The steady-state, one-dimensional heat diffusion equation in cylinder coordinates is [39]:

$$\frac{1}{r}\frac{\mathrm{d}}{\mathrm{d}r}\left(r\frac{\mathrm{d}T}{\mathrm{d}r}\right) + \frac{\dot{q}}{k} = 0 \tag{C.1}$$

Where k is the thermal conductivity of the tube and $\dot{q}$ is the uniform heat production in $\mathrm{W/m^3}$ due to the electric current. The uniform heat production is rewritten by substituting Equation 3.3.

$$\dot{q} = \frac{P}{\pi\left(r_2^2 - r_1^2\right)L_{\mathrm{tube}}} = \frac{2qr_1}{r_2^2 - r_1^2} \tag{C.2}$$

Integrating Equation C.1 once gives:

$$r\frac{\mathrm{d}T}{\mathrm{d}r} = -\frac{\dot{q}}{2k}r^2 + C_1 \tag{C.3}$$

Integrating Equation C.1 twice yields:

$$T(r) = -\frac{\dot{q}}{4k}r^2 + C_1\ln(r) + C_2 \tag{C.4}$$

Which is the general solution for the temperature distribution. The values for C_1 and C_2 can be found by substituting the appropriate boundary conditions in Equation C.3 and C.4:

$$\left.\frac{dT}{dr}\right|_{r_2} = 0 \longrightarrow C_1 = \frac{\dot{q}}{2k} r_2^2 T\left(r_2\right) = T_{\text{sensor}} \longrightarrow C_2 = T_{\text{sensor}} + \frac{\dot{q}}{4k} r_2^2 - C_1 \ln\left(r_2\right) \quad \text{(C.5)}$$

The temperature at the inner wall of the tube ($r = r_1$) becomes:

$$T_{\text{wall}} = T_{\text{sensor}} + \frac{\dot{q}}{4k}\left(r_2^2 - r_1^2\right) - \frac{\dot{q}}{2k} r_2^2 \ln\left(\frac{r_2}{r_1}\right) \quad \text{(C.6)}$$

D

Functional test of the SPIV

A SPIV is normally used in the gas chromatography industry. To apply it in a two-phase MPL thermal management system, a functional test was first done to test the specifications. The SPIV would be able to withstand a maximal pressure of 100 bar and the general leak rate is less than 10^{-7} cc-atm/sec [73]. The functional test visually observes whether the SPIV is working properly and whether no gas is escaping around the SPIV. This is done using the setup in Figure D.1. In the background there is a cylinder bottle filled with nitrogen. With the connected reducer, the nitrogen gas can leave the cylinder at a certain pressure. At the bottom left of the image, the nitrogen gas arrives at a valve. When opening this tap, the SPIV is filled when it is in the closed position. The SPIV is positioned in a beaker filled with Galden HT80. If gas were to escape this should be visible visually. When the SPIV is opened, the filled sample volume with nitrogen gas goes to the second beaker. Here it was clearly visible that the gas bubble ended up in the beaker. The above test was first performed for low pressure and then increased in steps towards 90 bar. From this, it can be concluded that the SPIV is working properly and is ready for implementation in the experimental setup.

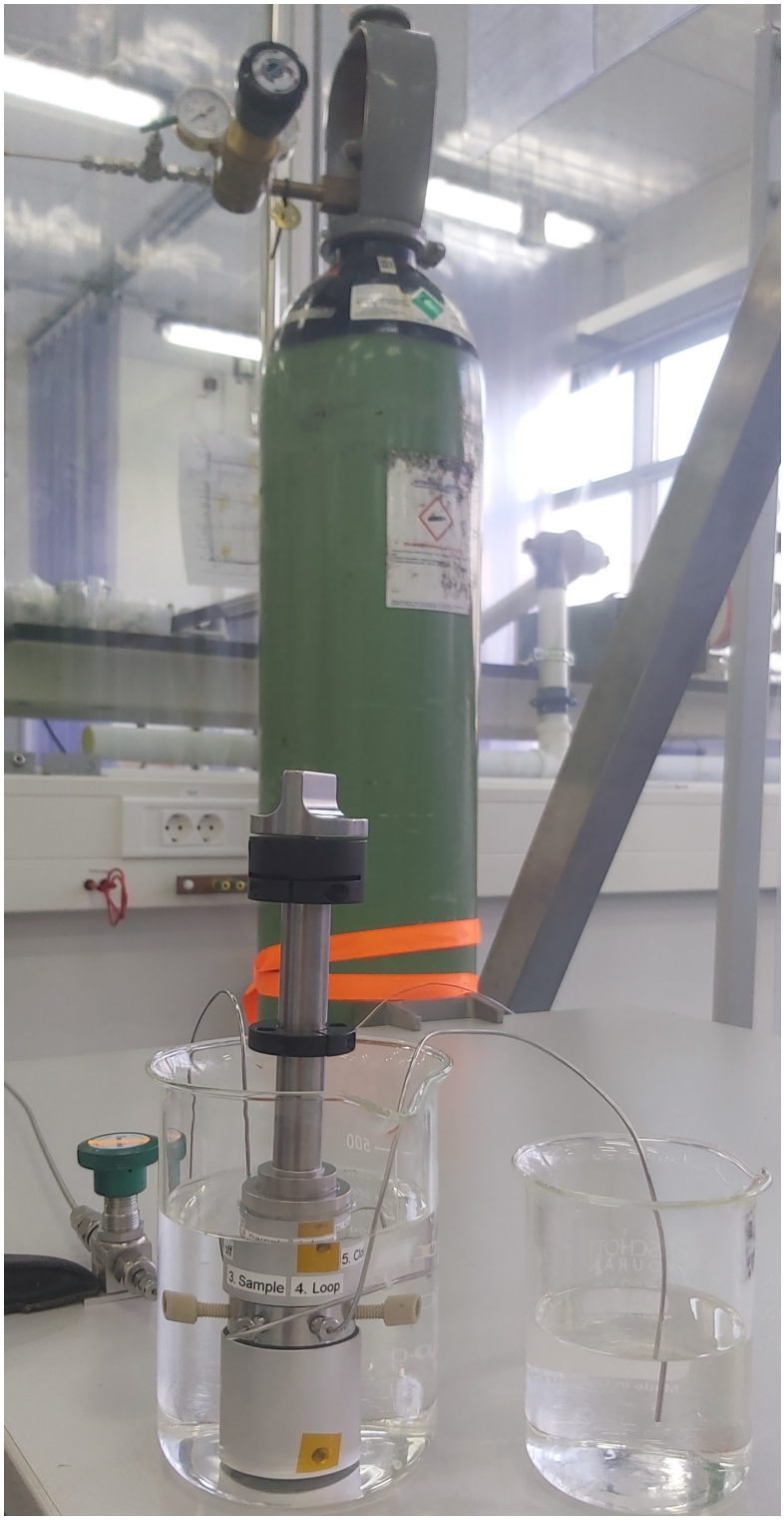

Figure D.1: Functioning test of the SPIV.

E

Empirical heat transfer coefficient plots

The Kandlikar correlations for various heat fluxes and the whole range for the vapor mass fraction is shown in the figure below. The influence of the heat flux becomes less as the vapor mass fraction increases.

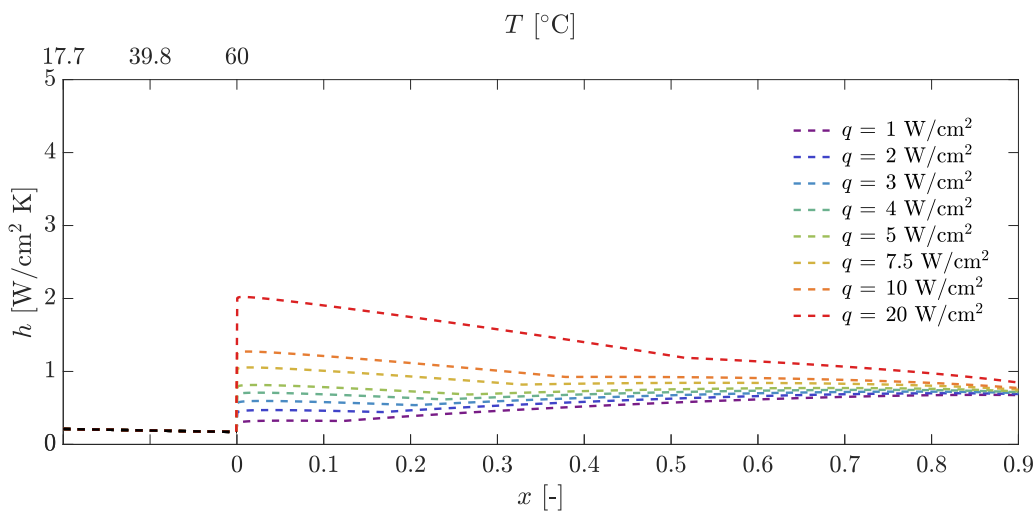

Figure E.1: Heat transfer coefficient plot for the Kandlikar correlation with ammonia as refrigerant for the whole range of the vapor mass fraction. A saturation temperature of 60 °C, a 1 mm internal diameter, a mass flow of 0.1 g/s, and various heat fluxes are used.

The same plot as Figure 4.1 is shown below, except that the Gungor & Winterton and Kim & Mudawar correlation are used here.

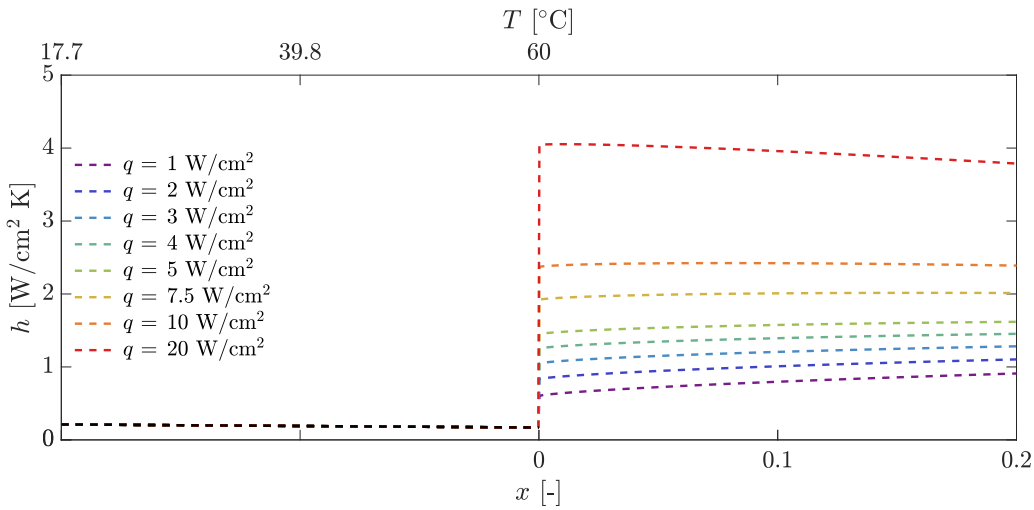

Figure E.2: Heat transfer coefficient plot for the Gungor & Winterton correlation with ammonia as refrigerant. A saturation temperature of 60 °C, a 1 mm internal diameter, a mass flow of 0.1 g/s, and various heat fluxes are used.

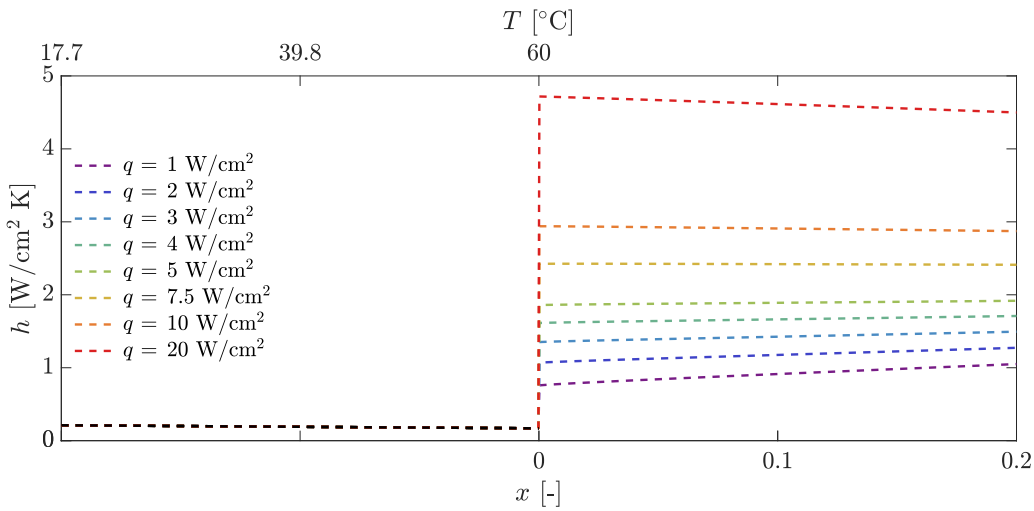

Figure E.3: Heat transfer coefficient plot for the Kim & Mudawar correlation with ammonia as refrigerant. A saturation temperature of 60 °C, a 1 mm internal diameter, a mass flow of 0.1 g/s, and various heat fluxes are used.

In comparison with the Kandlikar correlation, Gungor & Winterton estimates the heat transfer coefficient higher, and Kim & Mudawar estimate the highest.

The figure below shows the heat transfer coefficient for different mass flows. A single-phase heat transfer coefficient with a mass flow of 0.1 g/s is analytically determined because it is laminar. A mass flow of 0.2 g/s is in the transition region and 0.3 g/s is turbulent flow. Turbulent flow has a higher heat transfer coefficient because of the thinner stagnant fluid film layer on the heat transfer surface. For two-phase flow, the mass flow is related to the mass flux which is in the Boiling number. This boiling number can be found as a multiplication factor in the Kandlikar correlation shown in Equation 2.9. Therefore, the two-phase heat transfer coefficient is higher for higher mass flows.

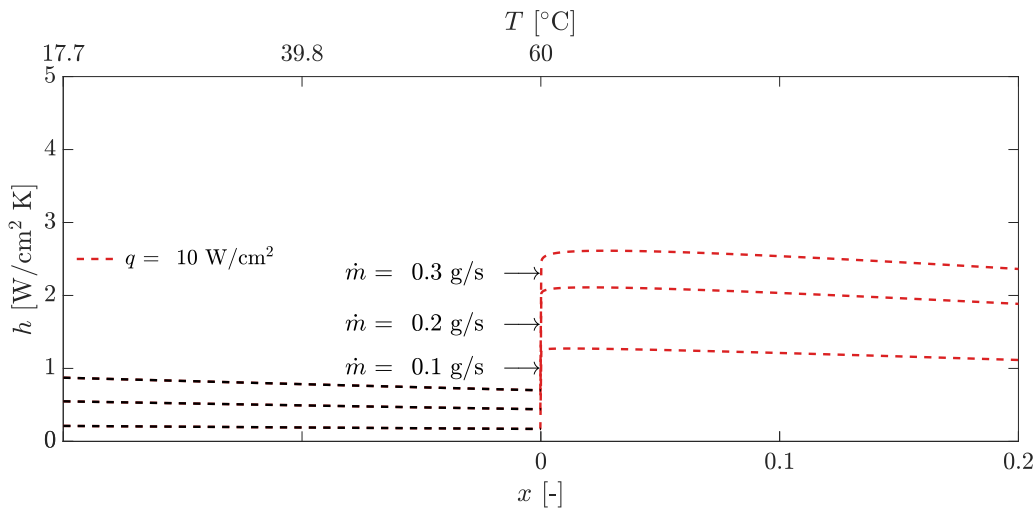

Figure E.4: Heat transfer coefficient plot for the Kandlikar correlation with ammonia as refrigerant. A saturation temperature of 60 °C, a 1 mm internal diameter, a heat flux of 10 W/cm^2, and various mass flows are used.

F

Results for the superheated liquid reference experiments

In addition to Figure 5.5, the temperatures over time for the different saturation temperatures and the other applied heat fluxes of 2, 3, 4, and 5 W/cm^2 are shown in the figures below.

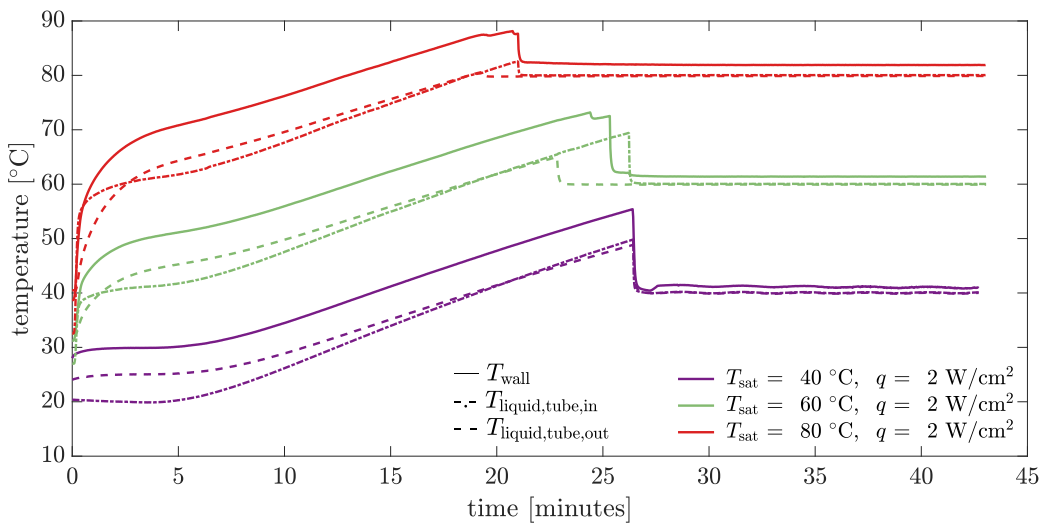

Figure F.1: Temperature over time for the different saturation temperatures at a constant heat flux of 2 W/cm^2.

At a saturation temperature of 40 °C, the superheated liquid temperature is 9.5 °C. In the following figures, the superheating does not jump back immediately at the trigger point and it takes time for T_{wall} to become constant.

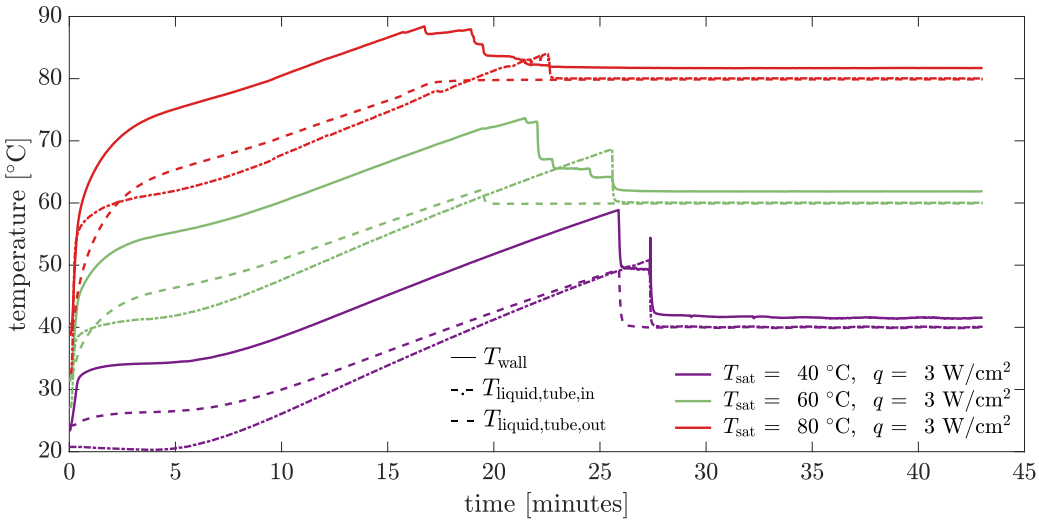

Figure F.2: Temperature over time for the different saturation temperatures at a constant heat flux of 3 W/cm^2.

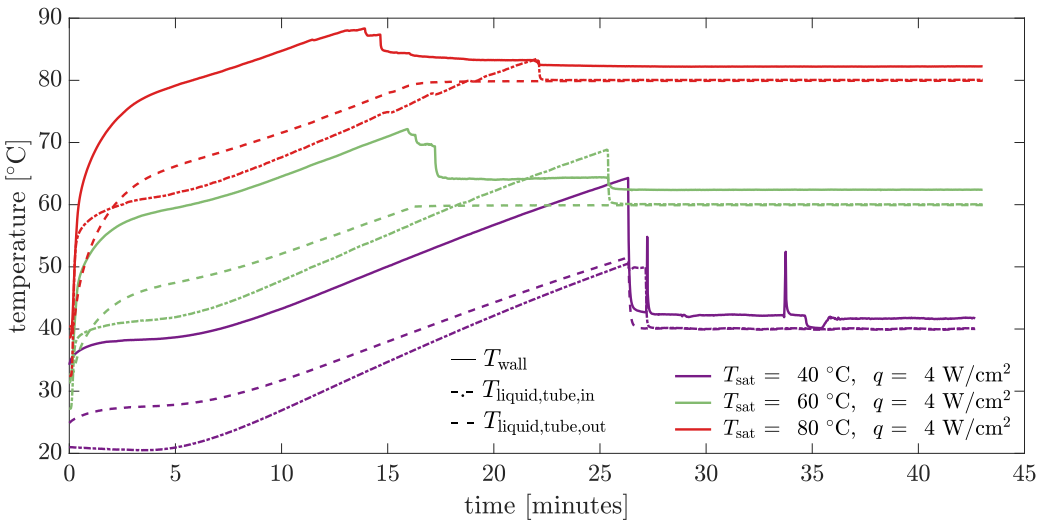

Figure F.3: Temperature over time for the different saturation temperatures at a constant heat flux of 4 W/cm^2.

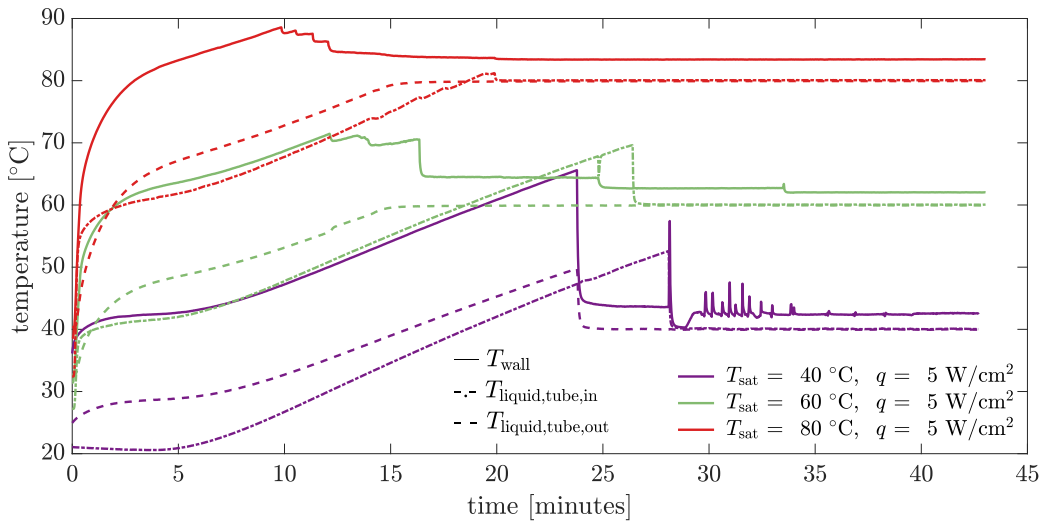

Figure F.4: Temperature over time for the different saturation temperatures at a constant heat flux of 5 W/cm^2.

The figures below show the temperature over time for the saturation temperature of 60, and 80 °C and the various heat fluxes.

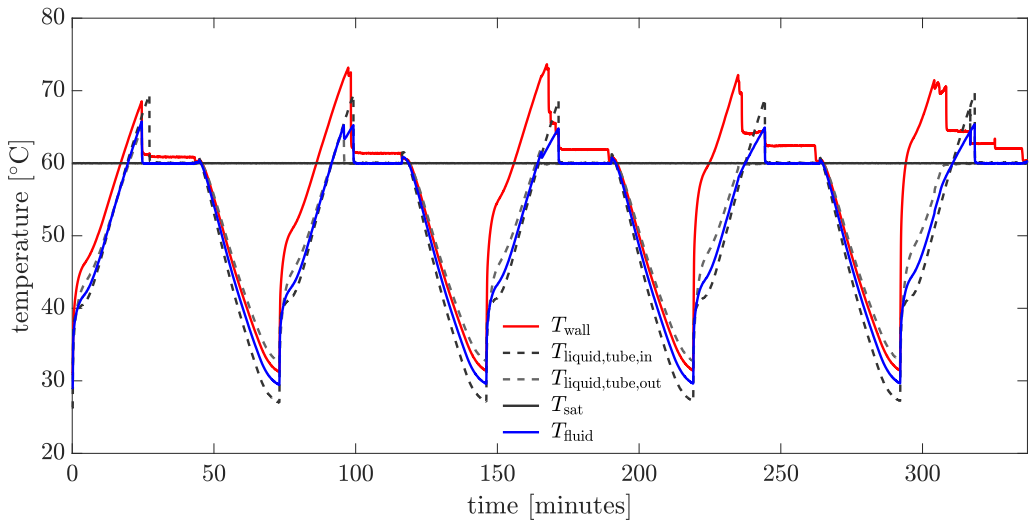

Figure F.5: Temperature over time for the applied heat fluxes of 1, 2, 3, 4, and 5 W/cm^2 with a saturation temperature of 60 °C.

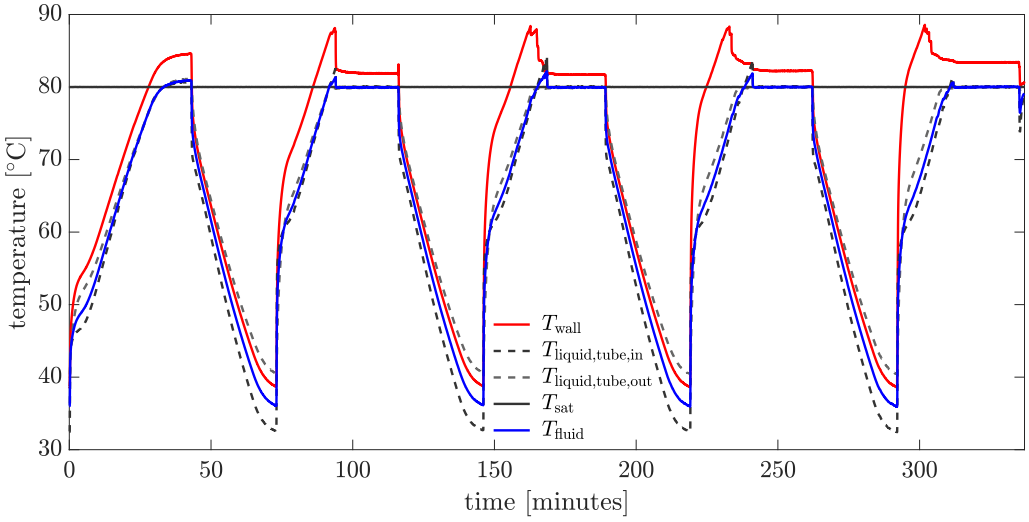

Figure F.6: Temperature over time for the applied heat fluxes of 1, 2, 3, 4, and 5 W/cm^2 with a saturation temperature of 80 °C.

G

Results of the mass flow influence

The subquestion of the influence of the heat flux and saturation temperature on the superheated liquid temperature is answered earlier in this report. Another parameter is the mass flow, which would be kept constant due to the size and complexity of the project. However, the last experiments have been done with other saturation temperatures and mass flows to see whether this could be the cause and as an introduction for a possible follow-up study.

Figure E.4 already indicates that a higher mass flow results in a higher heat transfer coefficient. Some experiments have been done to look into the influence of the mass flow on the superheated liquid temperature. An example experiment for a mass flow of 0.3 g/s is shown in Figure G.1.

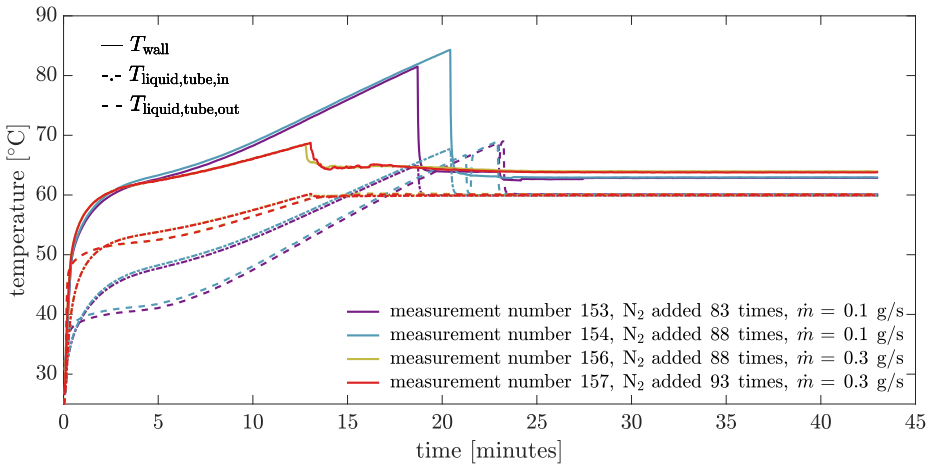

Figure G.1: Temperature over time for the applied heat flux of 5 W/cm^2 with a saturation temperature of 60 °C for different amounts of added nitrogen and mass flows.

A mass flow of 0.3 g/s means that the flow is turbulent. The figure shows that a higher mass flow lowers the superheated liquid temperature.